

¹

Analysis Note

Measurement of charged particle production in diffractive proton-proton collisions at $\sqrt{s} = 200$ GeV with tagging of the forward scattered proton

Leszek Adamczyk¹, Łukasz Fulek¹, Mariusz Przybycień¹, and Rafał Sikora¹

¹*AGH University of Science and Technology, FPACS, Kraków, Poland*

²

17th November 2020

In this note we present the analysis of the Single Diffractive Dissociation process with the STAR Roman Pot (RP) detectors at RHIC. The measurement is focused on the charged particle multiplicity, its dependence on the transverse momentum and pseudorapidity in three regions of ξ : $0.02 < \xi < 0.05$, $0.05 < \xi < 0.1$ and $0.1 < \xi < 0.2$. The identified particle to antiparticle (pion, kaon, proton and their antiparticle) multiplicity ratios as a function of transverse momentum in above three ξ regions are also measured. The data come from proton-proton collisions collected in 2015. The forward proton was tagged in the STAR Roman Pot system while the charged particle tracks were reconstructed in the STAR Time Projection Chamber (TPC). We describe all stages of the analysis involving comparison of the data with MC simulations and systematic uncertainty studies. More technical parts of the analysis are described in a supplementary analysis note [1].

³ **List of contributions**

Leszek Adamczyk	Analysis coordination/supervision, production of picoDST, production of embedded MC samples
Lukasz Fulek*	Main analyzer, write-up author
Mariusz Przybycień	Analysis supervision
Rafal Sikora	Analysis support

⁷ * - contact editor

⁹ **Change log**

17th Novem-	ver. 1.0	Initial revision
ber		
2020		

Contents

14	List of contributions	2
16	Change log	2
17	1 Introduction	1
18	2 Monte Carlo Samples	2
19	3 Data Sample and Event Selection	4
20	3.1 Track Selection	5
21	3.2 Fiducial Region of the Measurement	8
22	4 Background Contribution	11
23	4.1 Background from Non-Primary Tracks	13
24	4.2 Control Plots	20
25	5 Selection Efficiencies	24
26	5.1 Vertex Reconstruction	24
27	5.2 Correction to BBC-Small	29
28	6 Migrations into and out of the Fiducial Region	33
29	6.1 Migrations of Tracks into and out of the Fiducial Region	33
30	6.2 Migrations in ξ	34
31	7 Event Corrections and Unfolding Procedure	37
32	7.1 Correction to dN/dn_{sel}	37
33	7.2 Correction to Transverse Momentum and Pseudorapidity Distributions	40
34	7.3 Closure Tests	41
35	7.4 EAST-WEST asymmetry	41
36	7.5 Particle Identification	42
37	7.6 Antiparticle-to-Particle Ratios	48
38	8 Systematic Uncertainties	49
39	9 Results	54
40	10 Summary and Conclusions	61
41	Appendices	64
42	A Proton and Antiproton DCA Distributions	65
43	B Distributions of $n\sigma_{dE/dx}^i$ in SD	78

⁴⁴ **Acronyms**

⁴⁵	CD	Central Diffraction
⁴⁶	DD	Double Diffraction
⁴⁷	MBR	Minimum Bias Rockefeller
⁴⁸	MC	Monte Carlo
⁴⁹	ND	Non-Diffractive
⁵⁰	QCD	Quantum Chromodynamics
⁵¹	RP	Roman Pot
⁵²	SaS	Schuler and Sjöstrand
⁵³	SD	Single Diffraction
⁵⁴	TPC	Time Projection Chamber

1. Introduction

Inclusive measurements of charged-particle distributions in proton–proton (pp) collisions probe the strong interaction in the low-momentum transfer, non-perturbative regime of Quantum Chromodynamics (QCD). In this kinematic region interactions are usually described by phenomenological models implemented in Monte Carlo (MC) event generators. Measurements can be used to constrain the free parameters of these models. An accurate description of low-energy strong interaction processes is essential for understanding and precise simulation of different types of pp processes and the effects of multiple pp collisions in the same bunch crossing at high instantaneous luminosity at hadron colliders. Measurements with tagging of the forward-scattered proton are of special interest. They give direct access to specific but still significant part of pp processes called diffraction. In addition precise modelling of forward particle production is essential for better understanding of the longitudinal development of air showers observed in experiments studying cosmic radiation.

We present a measurement of charged particle production in events with single forward proton tagging (dominated by Single Diffraction (SD): $p + p \rightarrow p + X$). The following observables are studied:

$$\frac{1}{N_{\text{ev}}} \frac{dN_{\text{ev}}}{dn_{\text{ch}}}, \quad \frac{1}{N_{\text{ev}}} \frac{1}{2\pi p_{\text{T}}} \frac{d^2 N}{d\bar{\eta} dp_{\text{T}}}, \quad \frac{1}{N_{\text{ev}}} \frac{dN}{d\bar{\eta}} \quad (1.1)$$

where n_{ch} is the number of primary charged particles within kinematic range given by $p_{\text{T}} > 200$ MeV and $|\eta| < 0.7$, N_{ev} is the total number of events with $2 \leq n_{\text{ch}} \leq 8$, N is the total number of charged particles within the above kinematic acceptance and $\bar{\eta}$ is the pseudorapidity of the charged particle with longitudinal momentum taken with respect to direction of the forward scattered proton. To suppress non-SD events the trigger system required no signal in BBC-small in the direction of forward scattered proton and signal in BBC-small in opposite direction. The measurements are performed in a fiducial phase space of the forward scattered protons of $0.04 < -t < 0.16$ GeV $^2/c^2$ and $0.02 < \xi < 0.2$, where ξ is the fractional energy loss of the scattered proton and t is the squared four momentum transfer. In case of SD process $\xi = M_X^2/s$, where M_X is the mass of the state X into which one of the incoming proton dissociates and s is the center of mass energy squared of the pp system. The Mandelstam variable t is defined by $t = (p_1 - p_3)^2$, where p_1 is the four-momentum of the incoming proton, p_3 is the four-momentum of the outgoing proton. The above mentioned observables are presented in three ξ regions: $0.02 < \xi < 0.05$, $0.05 < \xi < 0.1$ and $0.1 < \xi < 0.2$. In addition their average values are presented as a function of ξ .

We have also studied an identified particle to antiparticle (pion, kaon, proton and their anti-particle) multiplicity ratios as a function of p_{T} also in the above mentioned three regions of ξ . The system X into which proton diffractively dissociates has net charge and baryon number +1. It is believed that initial charge and barion number should appear in the very forward direction leading to the equal amount of particles and antiparticles in the central region created by fragmentation and hadronization processes. However other scenarios are also possible where extra baryon is uniformly distributed over rapidity [2] or even appear close to the gap edge [3]. It is natural to expect that possible charge and baryon number transfer to central region will be better visible at small ξ where amount of particle-antiparticle creation is smaller due to the generally smaller particle multiplicity or due to the fact that gap edge is inside our fiducial region of $|\eta| < 0.7$.

96 2. Monte Carlo Samples

97 MC samples used to correct data for detector effects were obtained by the embedding MC technique
 98 [4], in which simulated particles are mixed with the real Zerobias events at the raw data
 99 level. Zerobias data events used in the embedding were sampled over the entire data-taking period
 100 in order to properly describe the data set used in the analysis. Two samples of embedding MC
 101 were produced:

- 102 1. Single particle MC, in which particles are generated from flat distributions in η and p_T , in
 103 order to have similar statistics in all bins.
- 104 2. The Schuler and Sjöstrand (SaS) model implemented in PYTHIA 8 with 4C tune.

105 Generated particles were passed through the full simulation of the STAR TPC and RP system
 106 detectors using GEANT3 and GEANT4, respectively, and then embedded into real data sample.
 107 These embedding events were next processed through the full event reconstruction chain.

108 It is preferred to get the detector corrections from a MC, which is dedicated to simulate
 109 the studied physics process. However, for this purpose, the statistics in the MC should be several
 110 times greater than in the analysed data sample. Since this is not possible with low efficiency of
 111 TPC and TOF, the basic method of corrections used in the analysis for p_T and $\bar{\eta}$ distributions
 112 is a method of factorization of global efficiency into the product of single-particle efficiencies. In
 113 this way, statistically precise multidimensional corrections on TPC and TOF were obtained from
 114 the single particle MC. The energy loss correction was also determined from the same MC sample.
 115 The charged-particle multiplicity distributions were unfolded from the measured multiplicities of
 116 TPC tracks based on the response matrix, which takes into account all detector effects. In this
 117 procedure single particle MC samples were not used.

118 All other detector corrections were obtained from PYTHIA 8 4C (SaS). In order to keep
 119 statistical precision coming from the corrections high, samples filtered on true-level values of ξ
 120 and t (not necessarily with reconstructed proton track in RP) are used.

121 Several additional MC samples were generated, in which simulated particles were propagated
 122 through full simulation and reconstruction chain but were not embedded into Zerobias events.
 123 Systematic uncertainty related to hadronization of the diffractive system was determined by using
 124 alternative hadronization models as implemented in HERWIG and EPOS. Results are compared
 125 to model predictions from PYTHIA 8 4C (SaS), HERWIG, EPOS and alternative PYTHIA 8
 126 model Minimum Bias Rockefeller (MBR) with A2 tune. EPOS predicts very large contribution
 127 of forward protons, which originate from Non-Diffractive (ND) events and are well separated in
 128 rapidity from other final state particles. This is the result of low mass excitation of the proton
 129 remnant (< 1 GeV) leading to hadronization of the beam remnant back to the proton. Therefore
 130 EPOS predictions were separated in two classes: diffractive (EPOS SD) modelled by Pomeron
 131 exchange and ND modelled by low mass excitation of the proton remnant (EPOS SD'). Such
 132 remnant treatment is very unique in EPOS compared to other string models, especially, to that
 133 used in PYTHIA 8, where ND forward protons are rare and arise from string fragmentation and
 134 hadronization. In all PYTHIA 8 models, diffractive cross-sections are scaled by the factors, which
 135 were introduced in order to describe the full phase space [5, 6]. In the SaS model, the scaling
 136 factors for SD and DD, F_{SD} and F_{DD} , are defined as a function of diffractive masses:

$$F_{SD} = \left(1 - \frac{M^2}{s}\right) \left(1 + \frac{c_{res} M_{res}^2}{M_{res}^2 + M^2}\right) \quad (2.1)$$

$$F_{DD} = \left(1 - \frac{M_a^2 + M_b^2}{s}\right) \left(\frac{sm_p^2}{sm_p^2 + M_a^2 M_b^2}\right) \times \left(1 + \frac{c_{res} M_{res}^2}{M_{res}^2 + M_a^2}\right) \left(1 + \frac{c_{res} M_{res}^2}{M_{res}^2 + M_b^2}\right) \quad (2.2)$$

137 where M and M_a, M_b are the invariant masses of the systems X and X_a, X_b for SD and DD,
138 respectively, $c_{\text{res}} = 2$ and $M_{\text{res}} = 2 \text{ GeV}/c^2$ were obtained from a fit to $pp/\bar{p}p$ data [5]. On
139 the other hand, in the MBR model the scaling factor is given as a function of the rapidity gap [6]:
140

$$S = \frac{1}{2} \left[1 + \text{erf} \left(\frac{\Delta y - \Delta y_S}{\sigma_S} \right) \right] \quad (2.3)$$

141 where Δy is the rapidity gap, $\Delta y_S = 2$ and $\sigma_S = 0.5$. As a result, diffractive cross sections are
142 artificially suppressed at relatively large values of $\xi (>0.05)$. This artificial suppression significantly
143 changes predicted distribution of ξ and fractions of different processes in our fiducial phase space.
144 Therefore data is also compared with expectations obtained without suppression of the diffractive
145 cross sections (MBR-tuned).

146 Figure 2.1 (left) shows the distribution of ξ generated with EPOS (SD and SD+SD') and
147 PYTHIA 8 SD (SaS, MBR and MBR-tuned). PYTHIA 8 (MBR) predicts a strong dependence of
148 the cross section on ξ , which is much weaker in PYTHIA 8 (SaS and MBR-tuned) and the weakest
149 in EPOS. This difference between PYTHIA 8 SaS and MBR models is expected since they are
150 based on different Pomeron trajectories ($\epsilon_{\text{SaS}} = 0, \epsilon_{\text{MBR}} = 0.104$). Only 30% of events in EPOS
151 are SD, while the rest are SD'. Since all MC samples were generated with forward proton filter
152 (a cut on the proton position in front of the RPs), the shapes of $|t|$ distributions for these samples
153 are biased. In order to compare them with each other, only their ratio to PYTHIA 8 (MBR)
154 predictions is presented as a function of $|t|$. EPOS SD is only relevant for very small $|t|$ (below
155 $0.04 \text{ GeV}^2/c^2$) and is suppressed in the STAR acceptance region, $0.04 < |t| < 0.16$, where EPOS
156 SD' contribution dominates. The t -slope is very different for EPOS SD and EPOS SD', while it
157 is similar for EPOS SD+SD' and PYTHIA 8 (SaS and MBR-tuned), EPOS SD and PYTHIA 8
158 (MBR). This is related to the smaller average value of ξ for EPOS SD and PYTHIA 8 (MBR)
compared to EPOS SD+SD' and PYTHIA 8 (SaS and MBR-tuned).

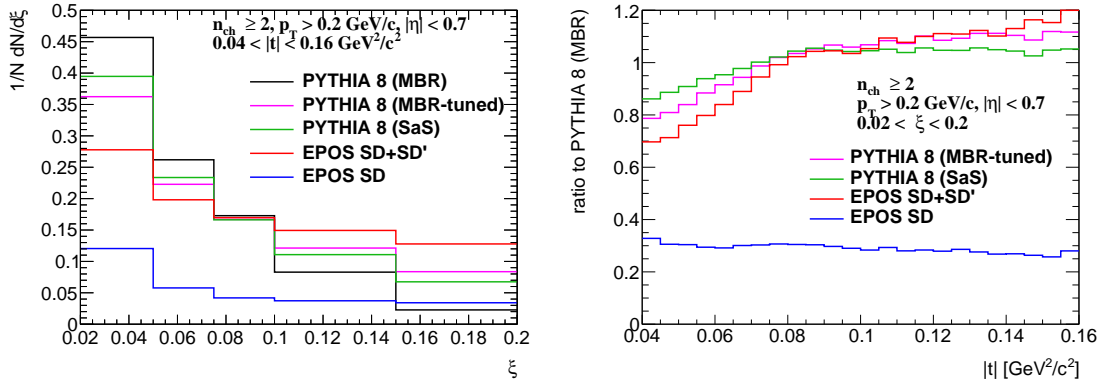


Figure 2.1: (left) ξ distribution for various MC generators and (right) ratios of different MCs to PYTHIA 8 (MBR) predictions as a function of $|t|$ at $\sqrt{s} = 200 \text{ GeV}$.

159

3. Data Sample and Event Selection

The data sample used in this analysis was collected in proton-proton collisions at centre-of-mass energy of $\sqrt{s} = 200$ GeV during RHIC Run 15.

All of the studies in this analysis use data from only the SDT trigger condition, which was the main trigger designed for SD studies in Run 15. The logic of the trigger was formed by the following conditions combined with the logical AND:

1. RP_EOR || RP_WOR - signal in at least one RP on any side of the STAR central detector,
2. veto on any signal in small BBC tiles or ZDC on the triggered RP side of the STAR central detector,
3. at least two TOF hits.

The above requirements were imposed in accordance with the diffractive event topology. Veto on any signal in small BBC tiles and ZDC allowed to accept only events with rapidity gap and reject diffractive events with simultaneous pile-up event. The requirement of at least two TOF hits was applied to ensure activity in the mid-rapidity.

Integrated luminosity delivered by the RHIC to the STAR experiment in pp collisions during Run 15 amounts to 185.1 pb^{-1} [9], whereas about 34.4M SDT events were gathered by the STAR detector, shown in Fig. 3.1, which corresponds to 16 nb^{-1} of integrated luminosity.

Event Selection

Events were selected from those passing the SDT trigger condition. In order to remove events of poor quality and to suppress background the following conditions were required:

1. trigger signals in exactly two stations of one arm of RP system (this requirement divides the sample into four sub-samples, which were later analysed independently, e.g. for background studies),
2. any trigger signal in small BBC tiles on the opposite side of the STAR central detector to the triggered RP station,

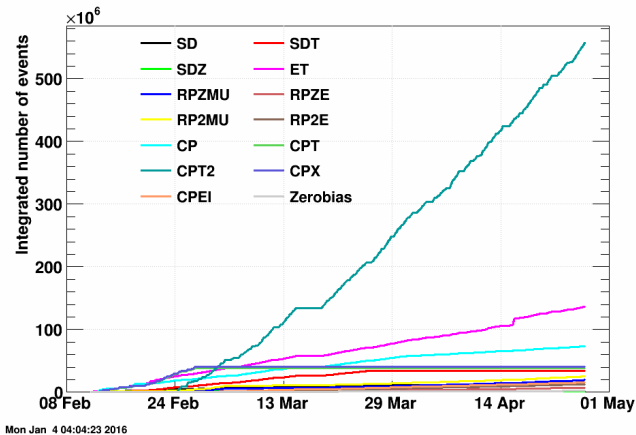


Figure 3.1: Cumulative number of events collected for each trigger in the RP data stream during Run 15 [7, 8].

- 186 3. exactly one proton track in the above RP stations with $0.02 < \xi < 0.2$ and $0.04 < -t <$
 187 $0.16 \text{ GeV}^2/c^2$.
- 188 4. exactly one vertex reconstructed from TPC tracks matched with hits in TOF (later in the text
 189 such vertex is referred as a TOF vertex),
- 190 5. TOF vertex within $|V_z| < 80 \text{ cm}$ - events with vertices away from the nominal IP have low
 191 acceptance for the central and forward tracks,
- 192 6. at least two but no more than eight primary TPC tracks, $2 \leq n_{\text{sel}} \leq 8$, matched with hits
 193 in TOF and satisfying the selection criteria described in Sec. 3.1,
- 194 7. if there are exactly two primary tracks satisfying the above criteria and exactly two global
 195 tracks used in vertex reconstruction (Sec. 5.1), the longitudinal distance between these global
 196 tracks should be smaller than 2 cm, $|\Delta z_0| < 2 \text{ cm}$.

197 Figure 3.2 shows the multiplicity of TOF vertices n_{vrt} (left) and the z -position of reconstructed
 198 vertices in single TOF vertex events (right). Data are compared to embedded PYTHIA 8 SD
 199 sample. These distributions are not significantly process-dependent, therefore, contributions from
 200 other processes are not included in these plots. Most events with $n_{\text{vrt}} > 1$ originate from in-time
 201 pile-up and are excluded from the analysis.

202 ZDC Veto

203 The SDT trigger conditions imposed a veto on any signal in the same-side ZDC. However, all MC
 204 samples do not contain ZDC simulation. To check the impact of this veto on the measurement,
 205 the total energy of neutral particles, such as n , γ , π^0 , produced within ZDC acceptance ($|\eta| > 6$)
 206 was measured using true-level PYTHIA 8 (SaS). In most of the events, the energy measured on
 207 the proton side of the IP is smaller than trigger thresholds (as shown in Fig. 3.3). Therefore,
 208 the ZDC veto has a negligible effect on the analysis and ZDC simulation is not needed.

209 3.1 Track Selection

210 The following quality cuts had to be passed by the selected primary tracks:

- 211 1. the tracks must be matched with hits reconstructed in TOF,
 212 2. the number of the TPC hits used in the helix fit $N_{\text{hits}}^{\text{fit}}$ must be greater than 24,

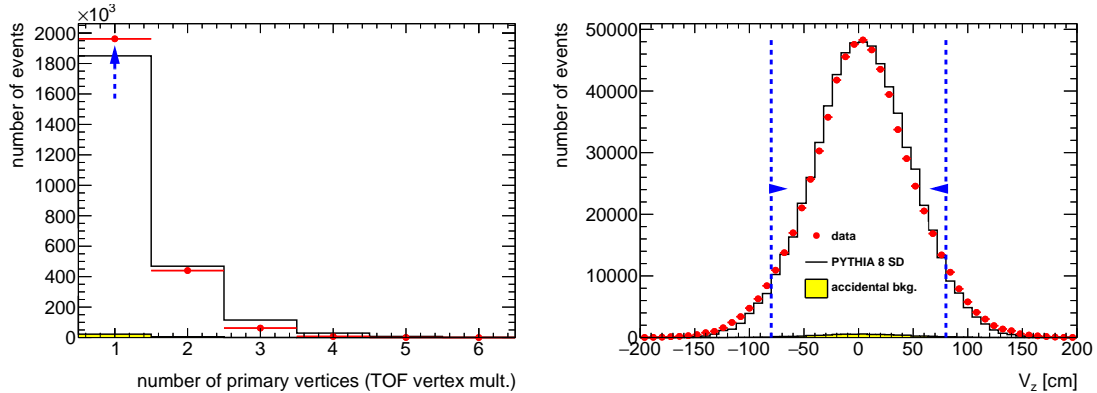


Figure 3.2: (left) Vertex multiplicity and (right) the z -position of reconstructed vertices in single TOF vertex events before applying the cut on the quantity shown. Blue lines indicate regions accepted in the analysis.

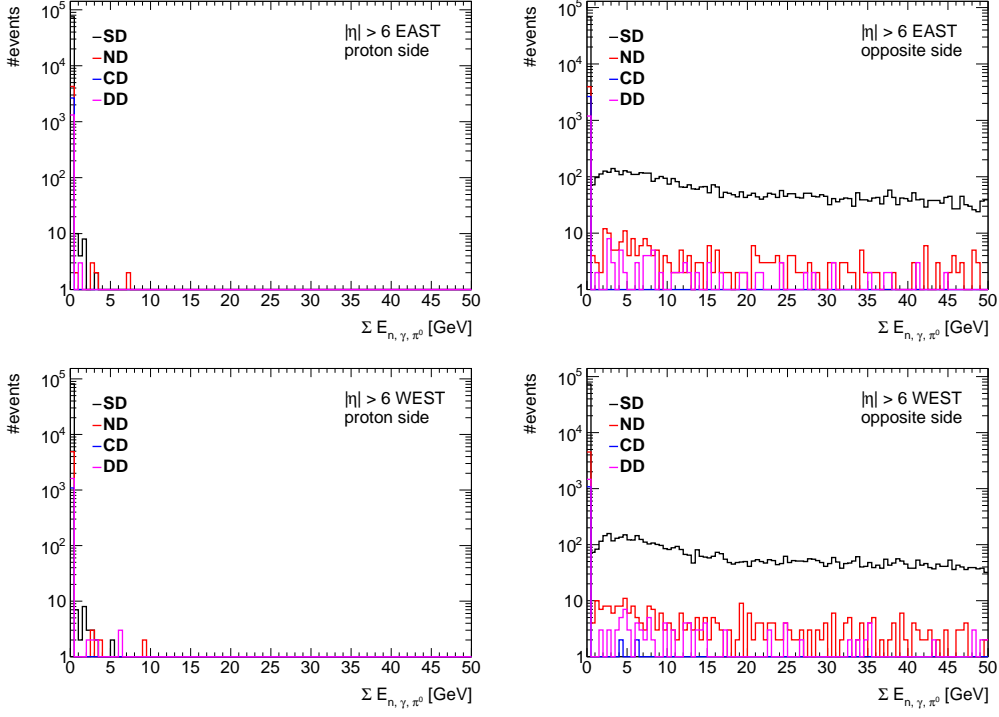


Figure 3.3: Total energy of neutral particles (n, γ, π^0) produced within ZDC acceptance ($|\eta| > 6$) for events in which forward-scattered proton is on (top) west and (bottom) east side of the IP. Distributions are presented separately for neutral particles produced on (left) the proton and (right) opposite side of the IP. PYTHIA 8 predictions for different processes are shown as colour histograms.

- 213 3. the number of the TPC hits used to determine the dE/dx information $N_{\text{hits}}^{\text{dE/dx}}$ must be
214 greater than 14,
- 215 4. the transverse impact parameter with respect to the beamline d_0 must be less than 1.5 cm,
- 216 5. the radial component of the distance of the closest approach between the global helix and
217 the vertex DCA_{xy} must be less than 1.5 cm,
- 218 6. the absolute magnitude of longitudinal component of the distance of the closest approach
219 between the global helix and the vertex $|\text{DCA}_z|$ must be less than 1 cm,
- 220 7. the track's transverse momentum p_T must be greater than 0.2 GeV/c,
- 221 8. the track's absolute value of pseudorapidity $|\eta|$ must be smaller than 0.7.

222 The $N_{\text{hits}}^{\text{fit}}$ and $N_{\text{hits}}^{\text{fit}}/N_{\text{hits}}^{\text{possible}}$ cuts are used to reject low quality TPC tracks and avoid track
223 splitting effects. The d_0 and global DCA_{xy} , $|\text{DCA}_z|$ cuts are used to select tracks that originate
224 from the primary interaction vertex. The cut on $N_{\text{hits}}^{\text{dE/dx}}$ is used to ensure that selected tracks
225 have sufficient energy loss information for particle identification purposes. In this analysis tracks
226 without identification are required to have $p_T > 0.2$ GeV/c and $|\eta| < 0.7$ due to high track
227 reconstruction and TOF matching efficiencies in this region. For the identified particle-antiparticle
228 ratio analysis, where charged pions, charged kaons and (anti)protons are measured, the p_T cut
229 was increased for kaons and (anti)protons to 0.3 and 0.4 GeV/c, respectively. The distributions
230 of the DCA_{xy} , $|\text{DCA}_z|$, d_0 , $N_{\text{hits}}^{\text{fit}}$ and $N_{\text{hits}}^{\text{dE/dx}}$ quantities together with applied cuts are shown in

Fig. 3.4, while the p_T , η and the azimuthal angle, ϕ , of the reconstructed tracks are shown in Fig. 3.5. Data are compared to embedded PYTHIA 8 SD sample.

The azimuthal angle of the reconstructed tracks for runs ≤ 16073050 is not described by PYTHIA 8. The inner sector #19 in the TPC was dead for this running period and some effects related to it were presumably not taken into account in the TPC detector simulation. Therefore, additional data-driven corrections to track efficiencies are used [1]. The larger accidental background is observed for runs > 16073050 , probably due to the higher bunch intensities in this running period [10].

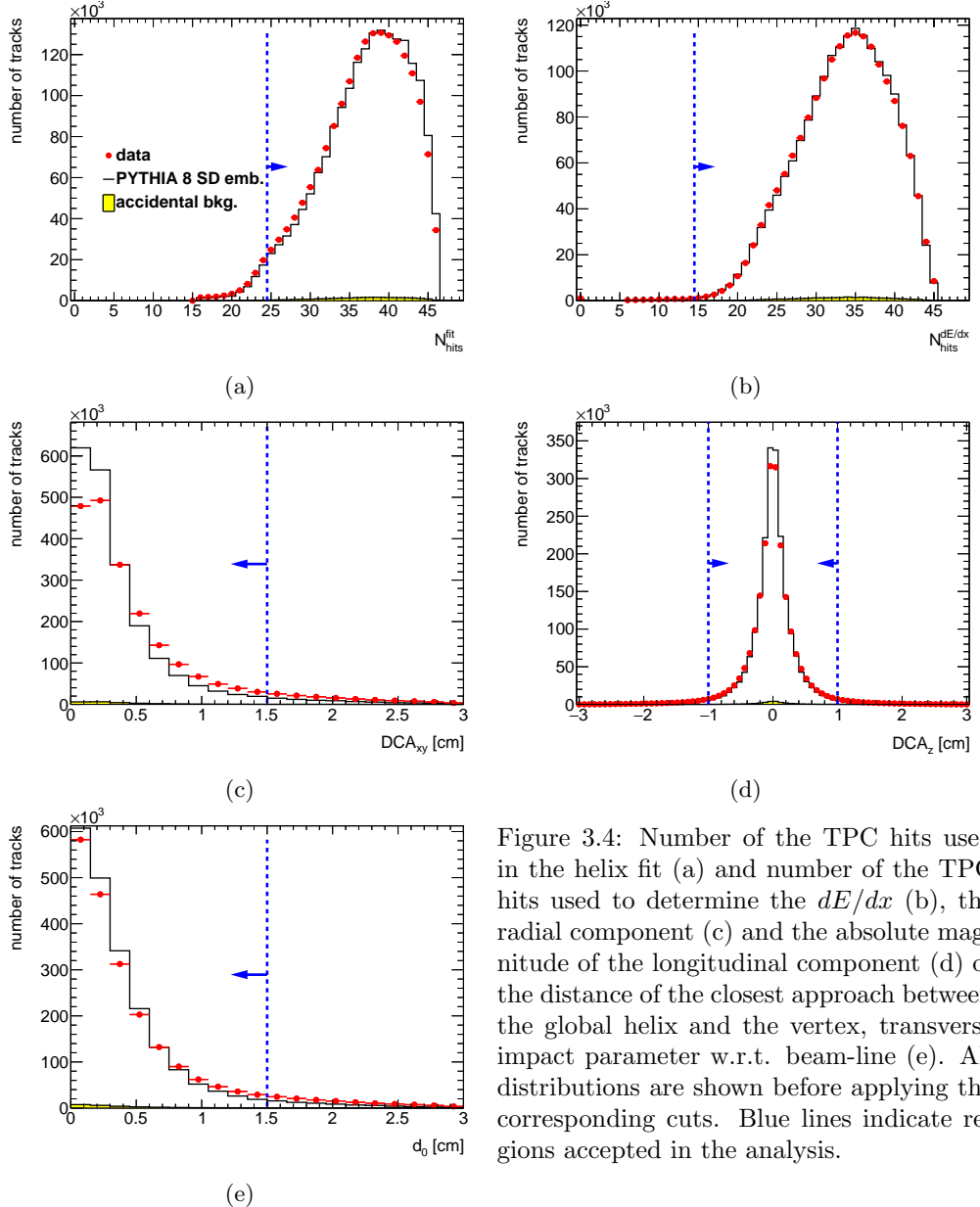


Figure 3.4: Number of the TPC hits used in the helix fit (a) and number of the TPC hits used to determine the dE/dx (b), the radial component (c) and the absolute magnitude of the longitudinal component (d) of the distance of the closest approach between the global helix and the vertex, transverse impact parameter w.r.t. beam-line (e). All distributions are shown before applying the corresponding cuts. Blue lines indicate regions accepted in the analysis.

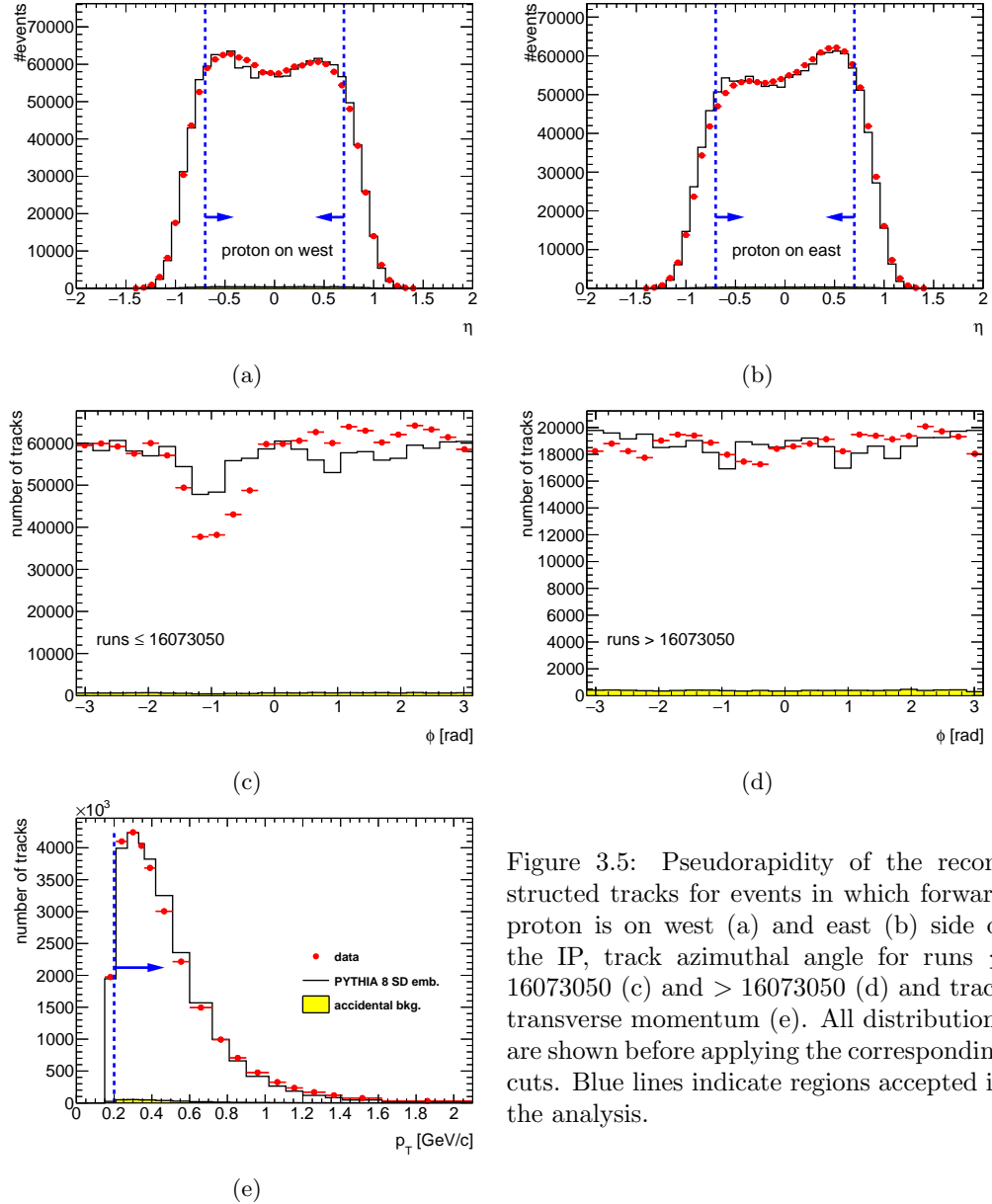


Figure 3.5: Pseudorapidity of the reconstructed tracks for events in which forward proton is on west (a) and east (b) side of the IP, track azimuthal angle for runs ≤ 16073050 (c) and > 16073050 (d) and track transverse momentum (e). All distributions are shown before applying the corresponding cuts. Blue lines indicate regions accepted in the analysis.

3.2 Fiducial Region of the Measurement

A fiducial phase space of measurement is defined by the following criteria. Primary charged particles are defined as charged particles with a mean lifetime $\tau > 300$ ps, either directly produced in pp interaction or from subsequent decays of directly produced particles with $\tau < 30$ ps. Primary charged particles had to be contained within the kinematic range of $p_T > 0.2$ GeV/c and $|\eta| < 0.7$. The results are corrected to the region of the total number of primary charged particles (without identification), $2 \leq n_{ch} \leq 8$. In identified charged antiparticle to particle ratio measurement, the lower transverse momentum limit was set for the analysed particles as follows: 0.2 GeV/c (pions), 0.3 GeV/c (kaons), 0.4 GeV/c (protons and antiprotons).

The measurements were performed in a fiducial phase space of the forward-scattered protons of $0.04 < -t < 0.16$ GeV $^2/c^2$ and $0.02 < \xi < 0.2$. Figure 3.6 shows that the fraction of events containing at least two primary charged particles, $\epsilon_{n_{ch}\geq 2}(\log_{10} \xi)$, is reduced by half for $\xi < 0.02$ compared to the region of larger ξ . In addition, the accidental background contribution at $\xi < 0.02$ is significant and approximately equal to 10% (Sec. 4). For these reasons the lower ξ cut was introduced. The upper ξ cut was required since the region of larger ξ is dominated by Double

254 Diffraction (DD) and ND (Sec. 4.2). The joint RP acceptance and track reconstruction efficiency
 255 was defined as the probability that true-level proton was reconstructed as a track passing the
 256 selection criteria. This efficiency was calculated as a function of $-t$ for three ranges of ξ separately
 257 and is shown in Fig. 3.7. Events were accepted only if the reconstructed values of $-t$ for protons
 258 fall within $> 5\%$ acceptance regions, which were required to be the same for each ξ region and
 259 similar to those defined in the elastic analysis [11]. Therefore, cuts on $0.04 < -t < 0.16 \text{ GeV}^2/c^2$
 260 were introduced. All measured observables are presented in three ξ regions: $0.02 < \xi < 0.05$,
 261 $0.05 < \xi < 0.1$ and $0.1 < \xi < 0.2$.

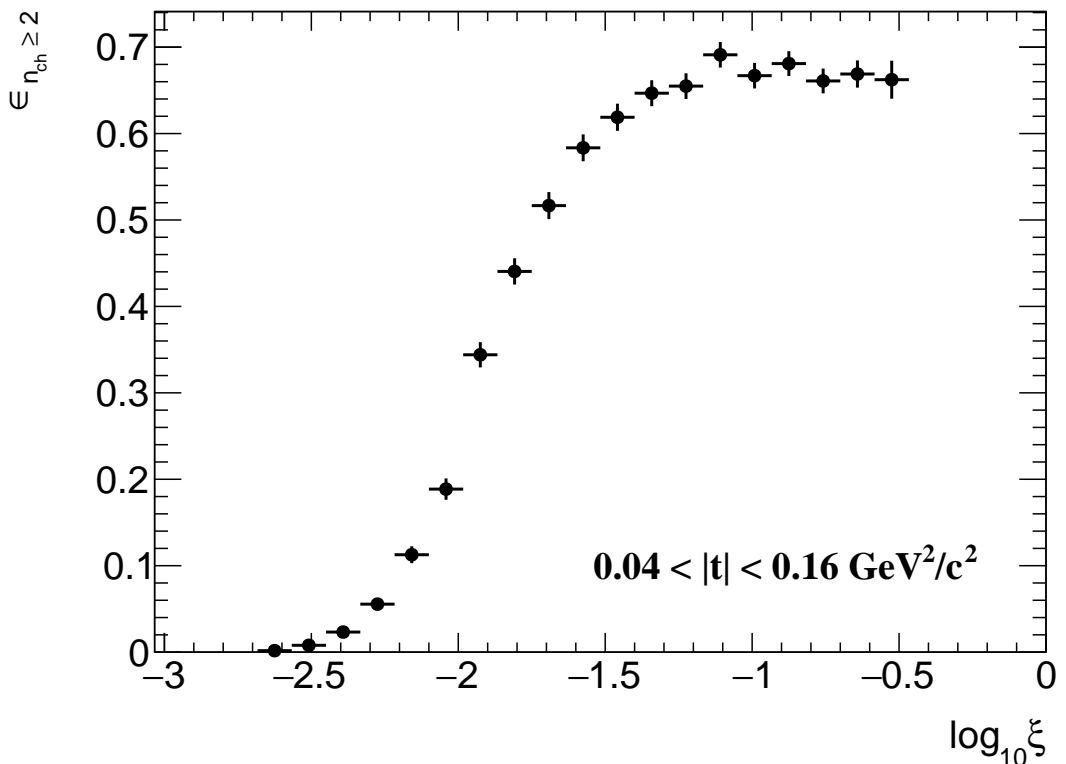


Figure 3.6: $\epsilon_{n_{ch} \geq 2}$ as a function of $\log_{10} \xi$ calculated from PYTHIA 8 (MBR).

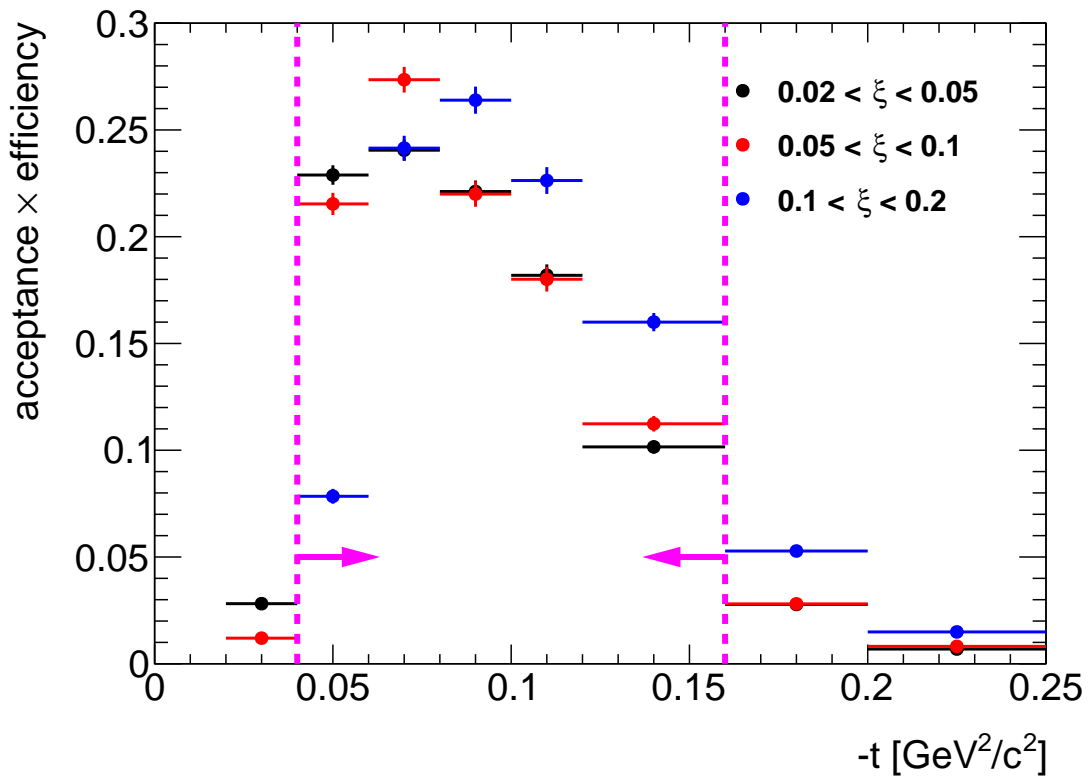


Figure 3.7: RP acceptance and track reconstruction efficiency as a function $-t$ in three ranges of ξ , calculated using PYTHIA 8 4C (SaS). Magenta lines indicate region accepted in the analysis.

4. Background Contribution

263 The background contributions to the charged-particle distributions can be divided into event-level
264 and track-level backgrounds, and are described in detail below:

- 265 • Accidental background refers to events which do not originate from a single collision of two
266 protons.
- 267 • Track backgrounds from non-primary tracks consist of secondary tracks and fake tracks; the
268 first come mostly from decays, the short-lived particles with mean life $30 < \tau < 300$ ps,
269 or secondary interactions with the detector dead material, while the second comes from the
270 track reconstruction algorithms and out-of-time pile-up with no corresponding true particles.

271 Accidental Background

272 The accidental backgrounds (same bunch pile-up background) are quantified using data-driven
273 method and defined as a process where in single bunch crossing there is coincidence of two inter-
274 actions, where any single-side proton signal is collected in coincidence with an independent signal
275 in the TPC+TOF+BBC detector. This type of background may come from the overlap of a signal
276 in RP (proton from beam-halo, low mass SD process without activity in TOF, elastic or low mass
277 Central Diffraction (CD) processes with undetected proton on the other side) with a signal in
278 TPC+TOF+BBC (mainly ND events without forward-scattered proton).

279 The accidental background contribution was calculated from Zerobias data (colliding bunches),
280 where two signatures of such background were investigated: the reconstructed proton in RP and
281 the reconstructed vertex from TPC tracks matched with TOF. The analysis was done for each RP
282 arm separately and thus the Zerobias data was firstly required to pass the following criteria:

- 283 1. no trigger in any RP or trigger in exactly one arm (two RPs) with exactly one reconstructed
284 proton track in that arm,
- 285 2. veto on any signal in small BBC tiles or ZDC on the same side of the IP as the RP arm
286 under consideration,
- 287 3. no or exactly one reconstructed vertex with at least two TOF-matched tracks passing the
288 quality criteria. The latter includes also signal in BBC small tiles on the opposite side of
289 the IP to the RP arm under study.

290 The sample of selected Zerobias data with total number of events N was divided into four classes:
291

$$N = N_{PS} + N_{RS} + N_{PT} + N_{RT} \quad (4.1)$$

292 where: N_{PS} is the number of events with reconstructed proton in exactly one RP and reconstruc-
293 ted TOF vertex, N_{RS} is the number of events with no trigger in any RP and reconstructed TOF
294 vertex, N_{PT} is the number of events with reconstructed proton in exactly one RP and no recon-
295 structed TOF vertex, N_{RT} is the number of events with no trigger in any RP and no reconstructed
296 TOF vertex. Since the signature of the signal is a reconstructed proton in exactly one RP and
297 a reconstructed TOF vertex, the number of such events can be expressed as:

$$N_{PS} = N(p_3 + p_1 p_2) \quad (4.2)$$

298 where: p_1 is the probability that there is a reconstructed proton in RP and there is no reconstruc-
299 ted TOF vertex, p_2 is the probability that there is no reconstructed proton in RP and there is
300 a reconstructed TOF vertex, p_3 is the probability that there is a reconstructed proton in RP and
301 there is a reconstructed TOF vertex (not accidental).

302 The other classes of events given in Eq. (4.1) can be expressed in terms of the above probabilities
 303 as:

$$\begin{aligned} N_{RS} &= N(1 - p_1)p_2(1 - p_3) \\ N_{PT} &= N(1 - p_2)p_1(1 - p_3) \\ N_{RT} &= N(1 - p_1)(1 - p_2)(1 - p_3) \end{aligned} \quad (4.3)$$

304 Finally, the accidental background contribution $A_{\text{bkg}}^{\text{accidental}}$ is given by:

$$A_{\text{bkg}}^{\text{accidental}} = \frac{p_1 p_2}{p_3 + p_1 p_2} = \frac{N_{RS} N_{PT} N}{N_R N_T N_{PS}} \quad (4.4)$$

305 where: $N_R = N_{RS} + N_{RT}$ and $N_T = N_{PT} + N_{RT}$.

306 The shapes of the accidental background related to TPC distributions come from the above
 307 Zerobias data events which pass all the analysis selection except having no trigger in any RP.
 308 The templates corresponding to RP distributions are from protons in the above data sets but
 309 with no reconstructed TOF vertex. The normalization is given by Eq. (4.4). Figure 4.1 shows
 310 distributions of the reconstructed ξ with the accidental background contribution for events with
 311 proton reconstructed in EU, ED, WU and WD arms. Accidental background in the range of
 312 $0.02 < \xi < 0.2$ is below 1% and increases to 10% at $\xi < 0.02$. Unphysical negative values of
 313 reconstructed ξ are due to the detector resolution.

314 The selection of Zerobias events, which is not unique, may provide some bias to the normalization
 315 of the accidental background. As a systematic check, two criteria for Zerobias selection were
 316 changed to:

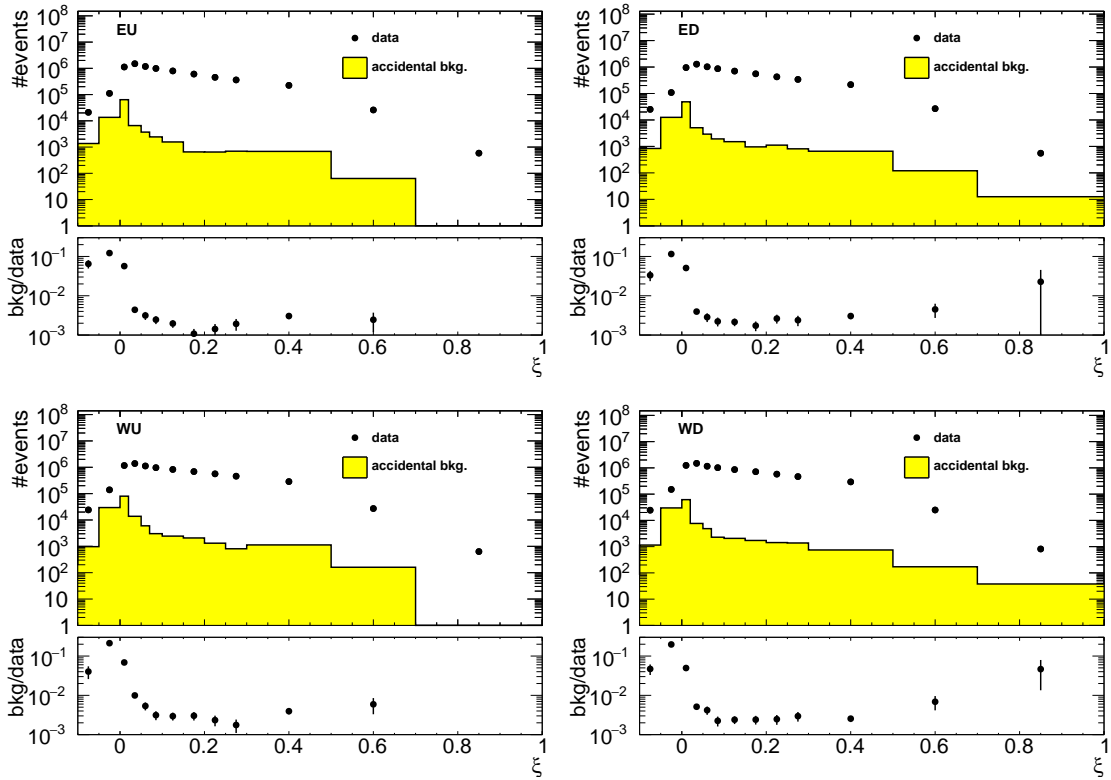


Figure 4.1: Uncorrected distributions of the reconstructed ξ for events with proton reconstructed in (top left) EU, (top right) ED, (bottom left) WU and (bottom right) WD arms. Data is shown as black markers, whereas the accidental background contribution is shown as yellow histogram. The ratio of accidental background and data is shown in the bottom panels.

- 317 1. no trigger in any RP or trigger in exactly one arm (two RPs) with *no more* than one
 318 reconstructed proton track in that arm, i.e. events with trigger signals in exactly one arm
 319 and without reconstructed proton track in that arm were also used,

 320 2. no or exactly one reconstructed TOF vertex (*without any additional requirements*), i.e.
 321 events with a reconstructed TOF vertex that does not have at least two primary tracks
 322 satisfying the selection criteria (Sec. 3.1), or with a reconstructed TOF vertex that is out of
 323 the range of $|V_z| < 80$ cm, were also accepted. The requirement of signal in BBC small tiles
 324 remains unchanged.

325 As a result of this change, the accidental background normalization increases of about 50% with
 326 respect to the nominal value. A symmetric systematic uncertainty of 50% of the normalization of
 327 accidental background is applied to the measurement.

328 4.1 Background from Non-Primary Tracks

329 Reconstructed tracks matched to a non-primary particle, so-called background tracks, originate
 330 mainly from the following sources:

- 331 • decays of short-lived primary particles with strange quark content (mostly K^0, Λ^0),
 332 • photons from π^0 and η decays which are converting to e^+e^- ,
 333 • hadronic interactions of particles with the beam-pipe or detector dead material.

334 Figure 4.2 (left) shows the background from non-primary tracks, $f_{\text{bkg}}(p_T, \eta)$, as a function
 335 of tracks' p_T and η , predicted by PYTHIA 8 SD model. There were no differences observed in
 336 the background contribution in different ξ ranges, hence, all three ξ ranges were merged for this
 337 study. The highest background fraction, which varies between 5 – 10%, was found to be at low
 338 p_T .

339 Figure 4.2 (right) shows the background track contribution to reconstructed tracks as a function
 340 of p_T and η calculated from EPOS SD+SD'. The differences between PYTHIA 8 and EPOS,
 341 which are up to 50% for $p_T > 0.5$ GeV/c (as shown in Fig. 4.3), were symmetrized and taken as
 342 a systematic uncertainty.

343 There is also a small (< 0.5%) contribution from fake tracks, $f_{\text{fake}}(p_T, \eta)$, i.e. tracks not associated
 344 with true-level particles, coming from out-of-time pile-up or formed by a random combination
 345 of TPC hits. The change by $\pm 100\%$ in this contribution was taken as a systematic uncertainty.

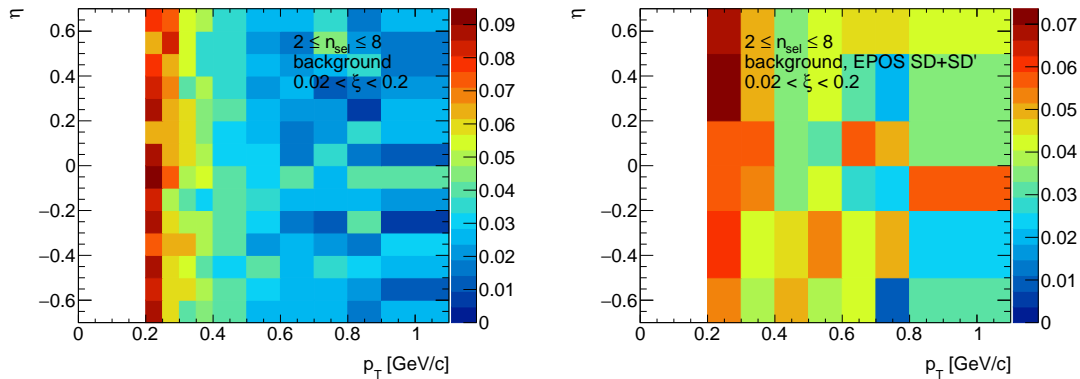


Figure 4.2: Distribution of fraction of selected tracks associated with non-primary particles in the range $0.02 < \xi < 0.2$ as predicted by (left) PYTHIA 8 4C (SaS) embedding and (right) EPOS SD+SD'.

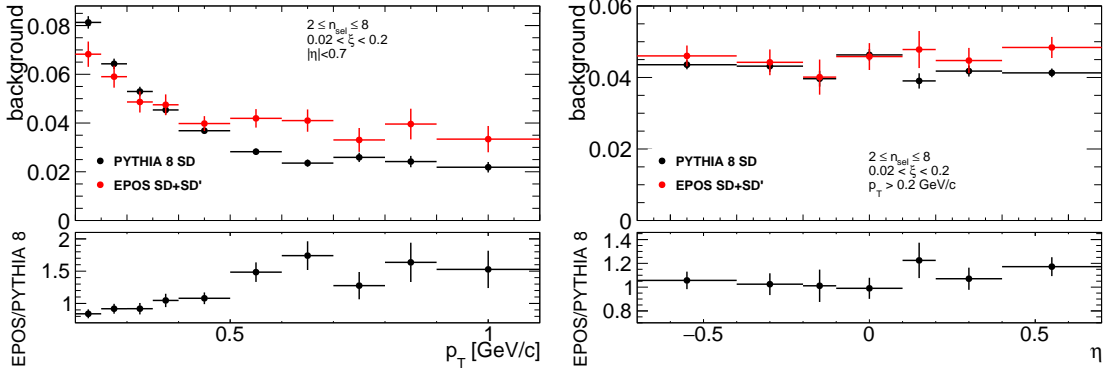


Figure 4.3: PYTHIA 8 SD and EPOS SD+SD' predictions of fraction of selected tracks associated with non-primary particles as a function of (left) p_T and (right) η . The ratio of EPOS and PYTHIA 8 predictions is shown in the bottom panels.

346 Proton Background

347 Secondary particles can be created due to the interaction of particles with detector dead-material.
 348 The proton sample contains background from such protons knocked out from the detector materials [12].
 349 Most of these protons have large DCA to the primary vertex and are not associated with it.
 350 However, the protons with small DCA are included in the primary track sample. Antiprotons
 351 do not have knockout background, hence the DCA tail is almost absent in their DCA distributions.

352 The fraction of knock-out background protons depends on a number of factors, including
 353 the amount of detector material, analysis cuts and the ξ of diffractive proton. While it is natural
 354 to calculate the fractions of primary and background protons in the MC sample, the MC models
 355 do not necessarily predict the fraction of knock-out background protons without any bias. Hence,
 356 data-driven methods should be used to calculate this type of background.

357 In order to correct for the knock-out background protons, sample enriched in proton back-
 358 ground was used for background normalization, where DCA_{xy} , DCA_z and d_0 cuts were aban-
 359 doned. Additionally, at least one, instead of exactly one, reconstructed vertex was allowed in this
 360 sample. Figures 4.4 and 4.5 show the DCA distributions of protons and antiprotons, respectively,
 361 for nominal (bottom) and background enriched (top) samples. The distributions for other p_T
 362 and ξ regions are shown in Appendix A. The protons and antiprotons are selected by a dE/dx
 363 cut of $-1 < n\sigma_{p,\bar{p}} < 3$ where $n\sigma_{p,\bar{p}}$ is given by Eq. (7.10). In some p_T regions, the dE/dx of
 364 (anti)protons and pions starts to overlap, hence, the asymmetric $n\sigma_{p,\bar{p}}$ cut was introduced in or-
 365 der to select as clean (anti)proton sample as possible. The fraction of knock-out protons within
 366 the selected sample is determined via MC template fits. The templates of reconstructed tracks
 367 with dE/dx corresponding to the proton and antiproton are obtained from PYTHIA 8 embedding
 368 MC separately for:

- 369 • primary (anti)protons,
- 370 • knock-out background protons (labeled as dead-material),
- 371 • fake tracks,
- 372 • secondary particles with dE/dx of (anti)proton (labeled as wrong PID - sec.),
- 373 • tracks associated with primary (anti)protons, but with the reconstructed vertex not matched
 374 to true-level primary vertex (labeled as wrong vtx),
- 375 • reconstructed track is partially matched to true-level particle (labeled as wrong match, track
 376 to true-level particle matching is described in [1]), i.e. track and true-level particle have
 377 appropriate number of common hit points but the distance between true-level particle and

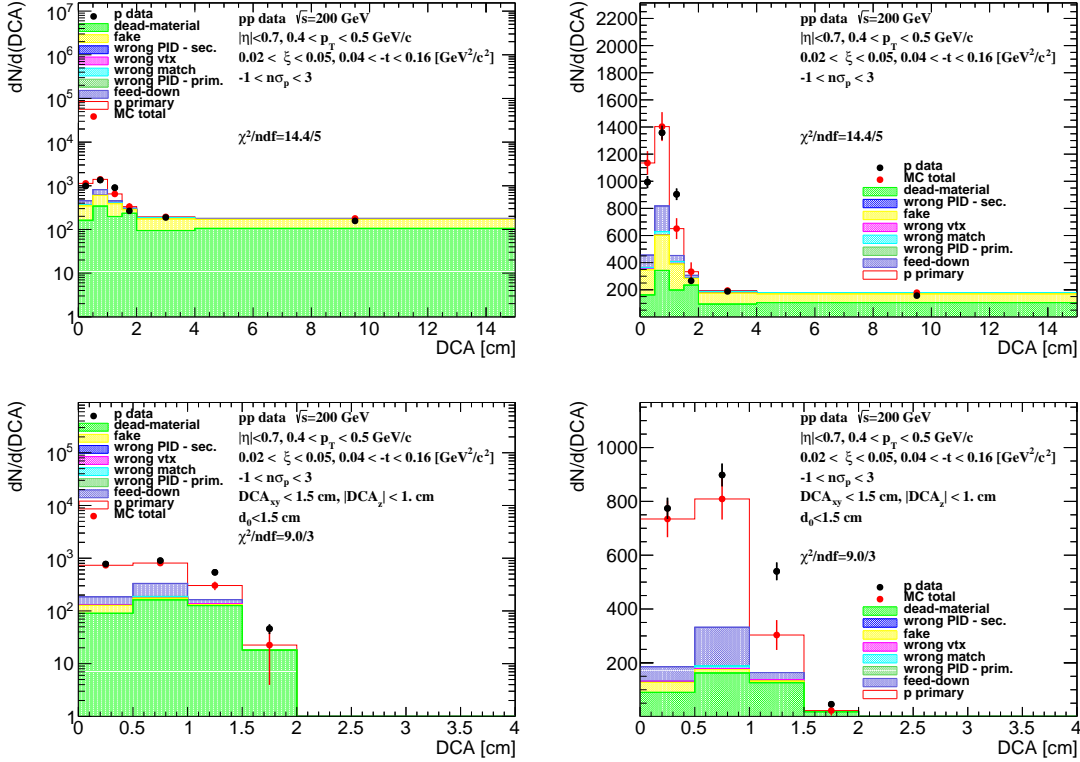


Figure 4.4: The DCA distributions of protons for $0.4 < p_T < 0.5 \text{ GeV}/c$ shown for single range of $0.02 < \xi < 0.05$ (shown in log and linear scale in left and right column, respectively). The MC contributions are shown after scaling the dead-material template to the tail of large DCA values, $2 < \text{DCA} < 15 \text{ cm}$. (top) Background enriched samples were used in the normalization procedure, whereas (bottom) the proton background was estimated from the nominal sample.

378 track is too large, $\delta^2(\eta, \phi) > (0.15)^2$, thus, track is not considered as primary particle
 379 according to discussion in [1],

- 380 • primary particles with dE/dx of (anti)proton (labeled as wrong PID - prim.),
 381 • (anti)proton as a product of short-lived decays, mainly Λ^0 (labeled as feed-down).

382 First, the background enriched sample was analyzed (Fig. 4.4, top), where the template of
 383 knock-out background protons was normalized to the number of events in the fake-subtracted tail
 384 of the DCA distribution, $2 < \text{DCA} < 15 \text{ cm}$. Next the knock-out proton and fake background
 385 was subtracted from the DCA distribution and the sum of other templates was normalized to
 386 the number of events in the signal region, $\text{DCA} < 1.5 \text{ cm}$.

387 The fraction of the knock-out proton background in the signal region, $\text{DCA} < 1.5$, was es-
 388 timated from the nominal sample (Fig. 4.4, bottom), where DCA_{xy} , DCA_z and d_0 track cuts
 389 were applied and exactly one reconstructed vertex was required. The normalization of each MC
 390 contribution was kept the same as that estimated for the background enriched sample. Figure 4.6
 391 shows the knock-out proton background as a function of p_T in three ranges of ξ . The following
 392 functional form was found to describe the background protons:

$$f_{\text{bkg}}^p(p_T) = p_0 \exp(p_1 p_T) \quad (4.5)$$

393 where p_0 and p_1 are free parameters obtained from a fit.

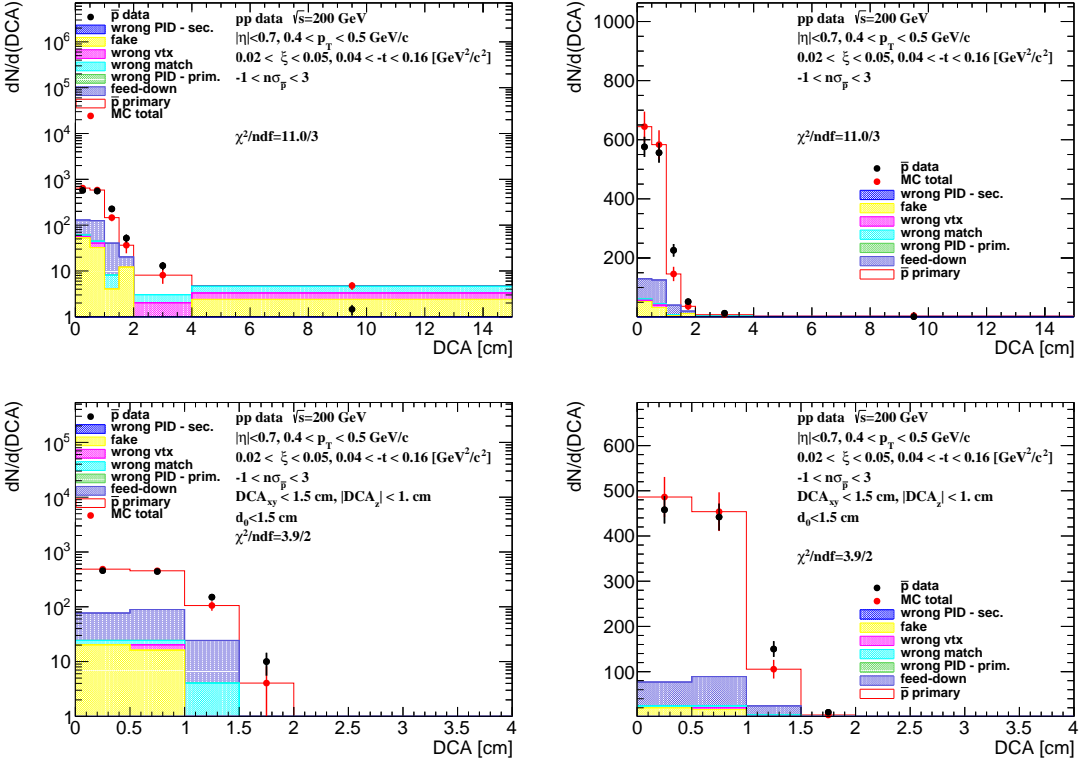


Figure 4.5: The DCA distributions of antiprotons for $0.4 < p_T < 0.5 \text{ GeV}/c$ shown for one range of $0.02 < \xi < 0.05$ (log and linear scale in left and right column, respectively). The MC contributions are shown as colour histograms. (top) Background enriched and (bottom) nominal samples were used.

394 The obtained fraction of knock-out background protons is approximately 20% at $p_T = 0.45$
 395 GeV/c and less than 10% at $p_T = 1.0 \text{ GeV}/c$. In PYTHIA 8 SD predictions (also shown in Fig. 4.6),
 396 such fraction is much smaller and equals to approximately 7% at $p_T = 0.45 \text{ GeV}/c$ and about 5%
 397 at $p_T = 1.0 \text{ GeV}/c$. This may suggest that there are differences in the amount of dead material in
 398 front of TPC between data and simulation, which is consistent with the studies presented in [1].

399 Figure 4.5 shows the corresponding DCA distributions with MC templates for antiprotons,
 400 where the background from knock-out particles is not present. Therefore, there was no need for
 401 any fit to be performed in this comparison. The MC templates fairly well describe the DCA
 402 distribution for both, protons, after tuning the fraction of knock-out background to data, and
 403 antiprotons.

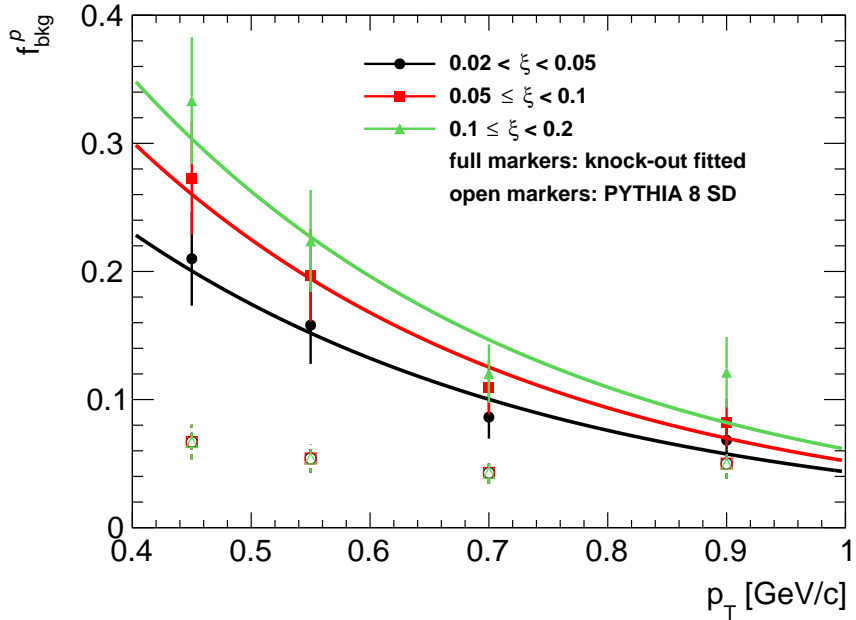


Figure 4.6: The fraction of knock-out proton background as a function of p_T in three ranges of ξ with fitted parametrizations. Full markers represent fitted knock-out background and open markers represent PYTHIA 8 SD predictions.

404 Systematic Uncertainty Related to Proton Background

405 The knock-out proton background estimation introduces systematic uncertainties. First, the nor-
 406 malization interval of the knock-out proton background template in the background enriched
 407 sample was changed to $4 < \text{DCA} < 15$ cm. This introduced a relative systematic uncertainty of
 408 up to 30% for $p_T \approx 0.9$ GeV/c.

409 The knock-out proton background contribution was parameterized as it is shown in Eq. (4.5).
 410 The systematic uncertainty related to the parameterization procedure was estimated by varying the
 411 parameters, p_0 and p_1 , by their statistical uncertainties ($\pm 1\sigma$). As a result, a relative systematic
 412 uncertainties of about 10% were obtained.

413 Differences in the shape of the DCA distribution between data and MC can affect the knock-
 414 out proton background estimation procedure. Figure 4.7 (top left) shows the data to MC ratio of
 415 the number of events in the background dominated region, $2 < \text{DCA} < 15$ cm. Since this region
 416 is used to estimate background normalization, and the shape of the DCA distribution in the data
 417 differs from that observed in the simulation, the predicted background in the $\text{DCA} < 1.5$ cm region
 418 can change. Thus, the following functional form was used to estimate the slope between data and
 419 MC:

$$\frac{\text{data}}{\text{MC}}(\text{DCA}) = A(\text{DCA} - 8.5) + B \quad (4.6)$$

420 where A (slope) and B are fit free parameters. Differences in slope between data and MC were used
 421 to estimate how many more background tracks would fit into the signal region and a systematic
 422 uncertainty, which varies up to 5% for $0.02 < \xi < 0.05$, was introduced.

423 All above components of the systematic uncertainty related to the knock-out proton back-
 424 ground, shown in Fig. 4.7, are added in quadrature. Those related to the fit range and the shape
 425 of the proton background are symmetrized. Figure 4.8 shows the fraction of knock-out proton
 426 background in three ranges of ξ and the total systematic uncertainty related to it.

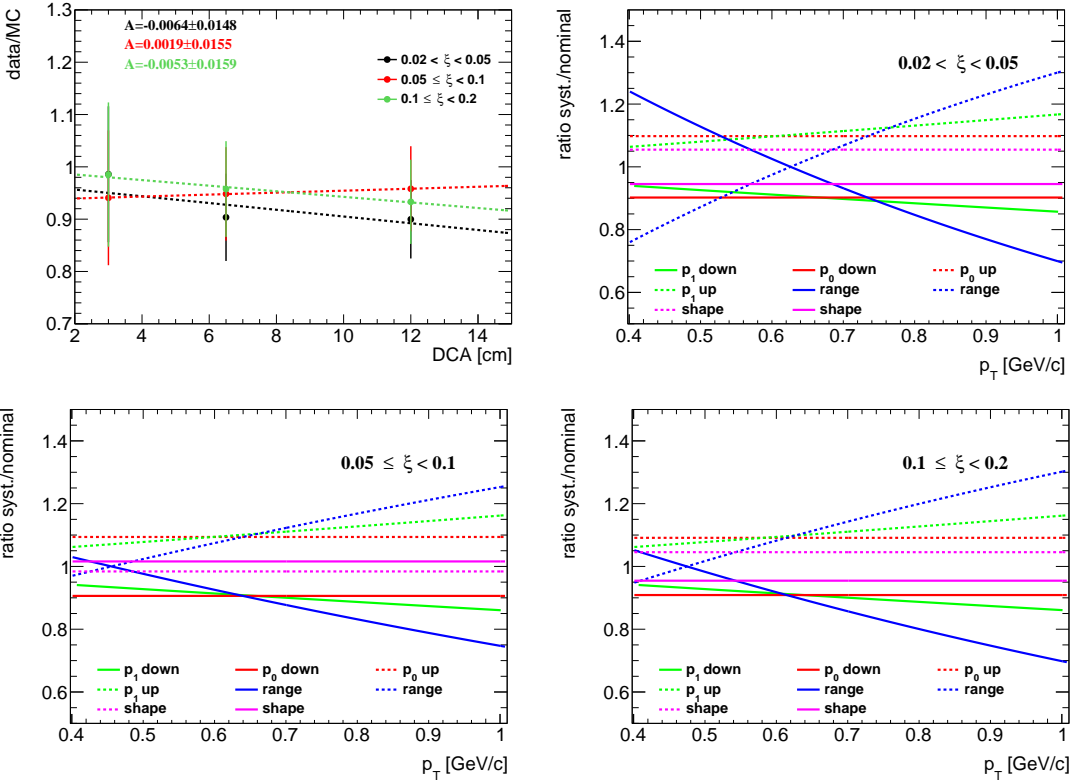


Figure 4.7: (top left) Data to MC ratio of the number of events in the background dominated region in three ranges of ξ with fitted functional form given by Eq. (4.6). (top right and bottom) Components of the systematic uncertainty related to the knock-out background protons contribution in three ξ ranges.

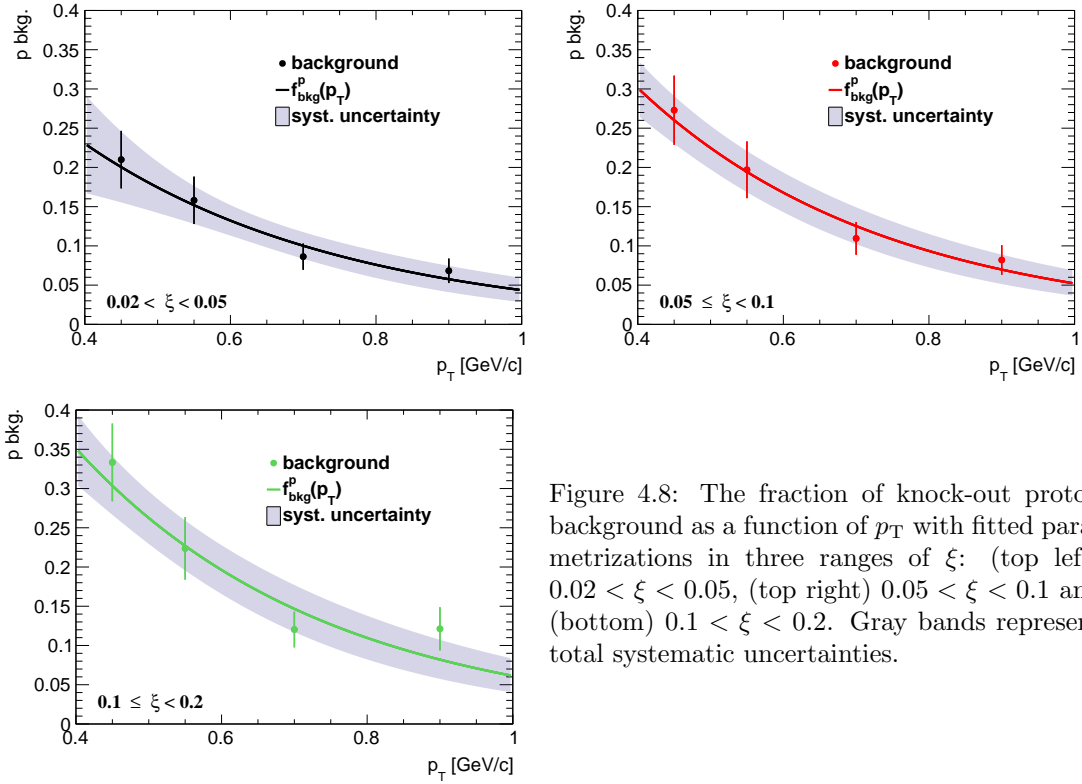


Figure 4.8: The fraction of knock-out proton background as a function of p_T with fitted parametrizations in three ranges of ξ : (top left) $0.02 < \xi < 0.05$, (top right) $0.05 \leq \xi < 0.1$ and (bottom) $0.1 \leq \xi < 0.2$. Gray bands represent total systematic uncertainties.

427 **Pion Background**

428 The pion spectra are corrected for weak decays (mainly of K_S^0 and Λ^0), muon contribution and
 429 background from the detector dead-material interactions. The pion decay muons can be identified
 430 as pions due to the similar masses. These background contributions are obtained from PYTHIA 8
 431 SD. Figure 4.9 shows the background contribution to the pion spectra as a function of p_T in
 432 three ranges of ξ , separately for π^- and π^+ . Since there were negligible differences observed
 433 between these three ranges of ξ , the background contribution was averaged over ξ . The following
 434 parametrization was found to describe it:

$$f_{\text{bkg}}^\pi(p_T) = a_0 \exp(a_1 p_T) + a_2 p_T^2 + a_3 p_T \quad (4.7)$$

435 where a_i , $i = 0, \dots, 3$ are free parameters of the fitted function.

436 The pion background contribution varies between 5% at low- p_T ($p_T = 0.25$ GeV/c) and about
 437 1% at $p_T = 1.0$ GeV/c for both negatively and positively charged pions. In addition, the back-
 438 ground was calculated from EPOS SD+SD' for the full range of ξ . The differences between
 439 PYTHIA 8 and EPOS are up to 1% for π^- .

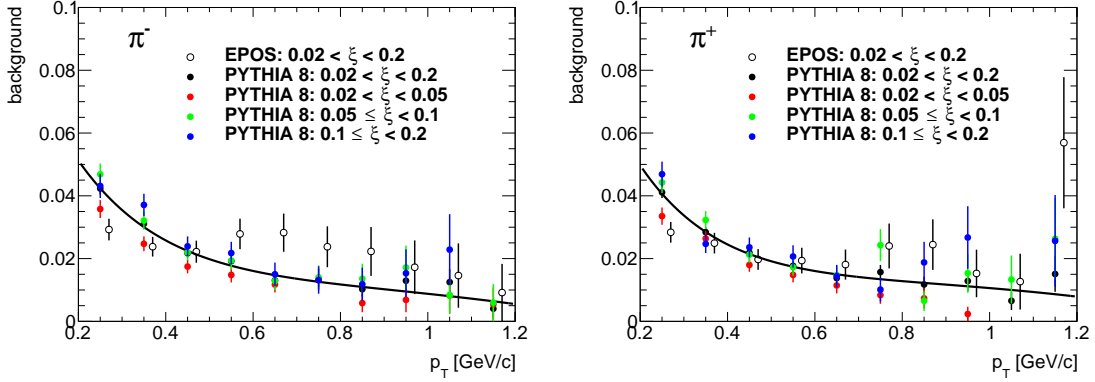


Figure 4.9: Pion background fraction as a function of p_T shown separately for (left) negatively and (right) positively charged pions in three ranges of ξ : (red) $0.02 < \xi < 0.05$, (green) $0.05 < \xi < 0.1$, (blue) $0.1 < \xi < 0.2$. (full black points) The pion background averaged over three ranges of ξ with fitted parametrization is also shown. Open black points represent EPOS predictions for the full ξ range.

4.2 Control Plots

Events, in which forward-scattered proton and reconstructed TOF vertex are the result of the same pp interaction, may originate from ND, DD, SD, and CD processes. It is preferred to estimate the background contribution from data, using dedicated control regions. Since such regions were not found, the relative contributions from the above processes were estimated from MC models and are therefore model dependent. Tracks reconstructed in RPs may also be:

- forward-scattered protons produced in the SD, CD or DD diffractive systems or from ND events,
- secondary particles from showering initiated by interaction of forward-scattered protons with beam-line elements. This contribution is negligible.

Figure 4.10 shows the uncorrected ξ and t distributions in data compared to various MC models: PYTHIA 8 A2 (MBR), PYTHIA 8 A2 (MBR-tuned), PYTHIA 8 4C (SaS) and EPOS. The MC distributions are split into SD, ND, DD and CD components. For EPOS, SD' is separated from the ND events. Additionally, the accidental background is also shown. PYTHIA 8 A2 (MBR) predictions, shown in Fig. 4.10 (a-b), do not agree with the data, especially there is small number of events in the region of large values of ξ . This effect may be due to the scaling factors, which are introduced in PYTHIA 8 to artificially suppress diffractive cross sections in the high mass region, or due to too large Pomeron intercept ($\epsilon = 0.104$). Therefore, additional two samples of PYTHIA 8 were generated: without this artificial suppression (MBR-tuned) and with $\epsilon = 0$ (SaS). Their predictions, shown in Fig. 4.10 (c-f), agree much better with the data than PYTHIA 8 A2 (MBR) and result also in a suppression of non-SD events. Amongst PYTHIA 8 models, PYTHIA 8 A2 (MBR-tuned) shows the best agreement with the data. EPOS predictions, shown in Fig. 4.10 (g-h), describes data better than PYTHIA 8 but shows a dominant contribution of SD' events. The CD contribution in EPOS is several times greater than in PYTHIA 8 (MBR), but it was never tuned to describe any data, as opposed to PYTHIA 8 (MBR) in which the CD cross sections are constrained by CDF measurements [13]. The CD component in the SaS model is based on simple scaling assumption, therefore, it is not usually used by the experimental communities. All MCs predict significant DD and ND background at large ξ , thereby the analysis was limited to $\xi < 0.2$.

Figures 4.11 to 4.13 show the uncorrected distributions of variables used in the later analysis: n_{sel} , p_T and $\bar{\eta}$. The contributions from non-SD (except EPOS SD') interactions differ a bit between each other, i.e. EPOS predicts significantly larger CD contribution, whereas DD and ND are suppressed in PYTHIA 8 A2 (MBR-tuned) and PYTHIA 8 4C (SaS). PYTHIA 8 A2 (MBR) is used as the default model of non-SD contribution subtracted from the data with systematic uncertainty $\pm 50\%$, which covers all differences between the models except EPOS SD'. In this analysis EPOS SD' is considered as an alternative to PYTHIA 8 SD model of events with forward-scattered proton in the final state, where one of the proton remnants hadronizes back to a single proton (non-diffractive process), while in PYTHIA 8 the initial proton stays intact (diffractive process). As a consequence, results are compared with the sum of SD and SD' processes for EPOS model.

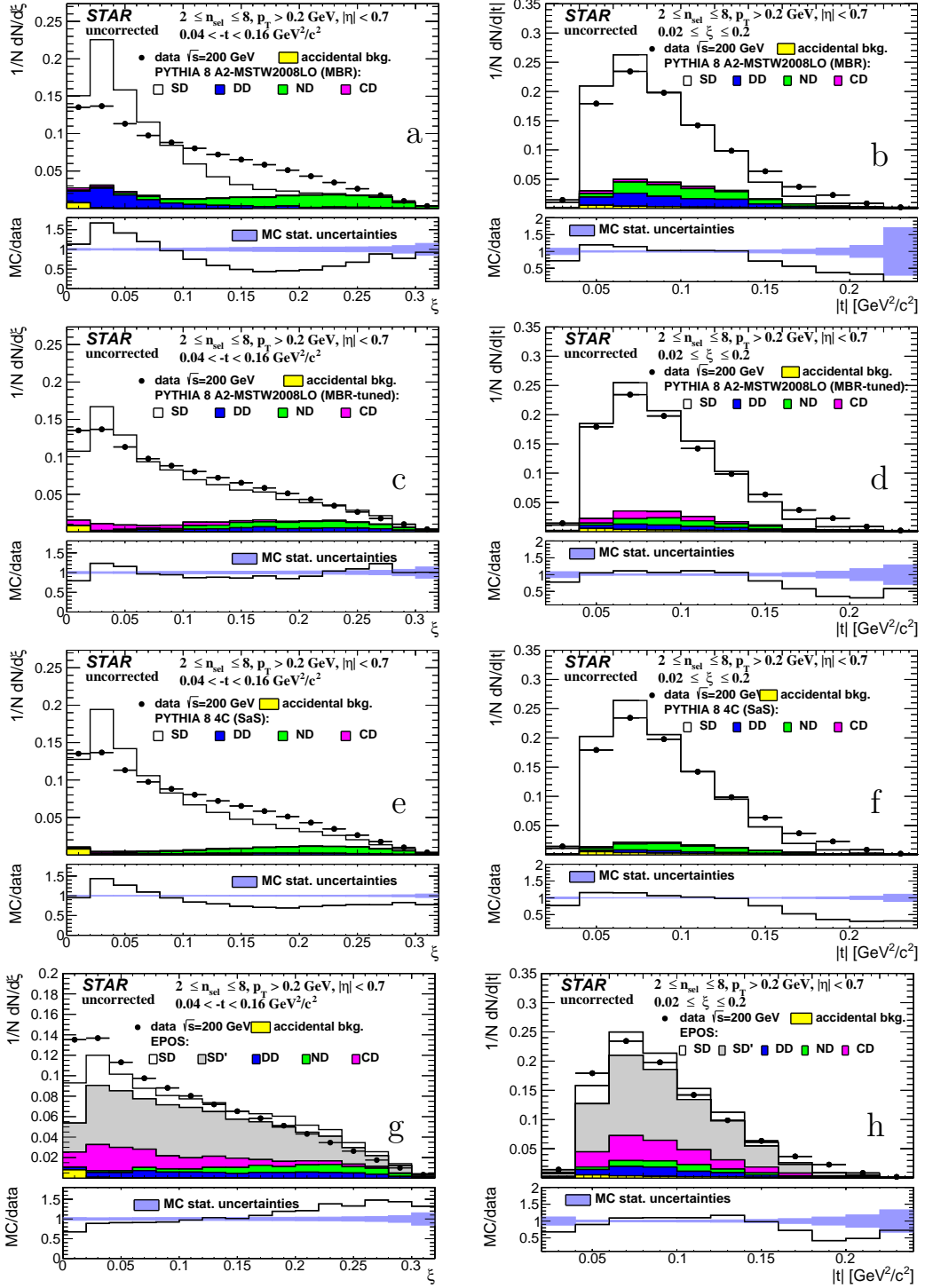


Figure 4.10: Uncorrected distributions of data compared to various MC models: (a-b) PYTHIA 8 A2 (MBR), (c-d) PYTHIA 8 A2 (MBR-tuned), (e-f) PYTHIA 8 4C (SaS) and (g-h) EPOS, as a function of (left column) ξ and (right column) $|t|$. The ratio of MC predictions and data is shown in the bottom panels.

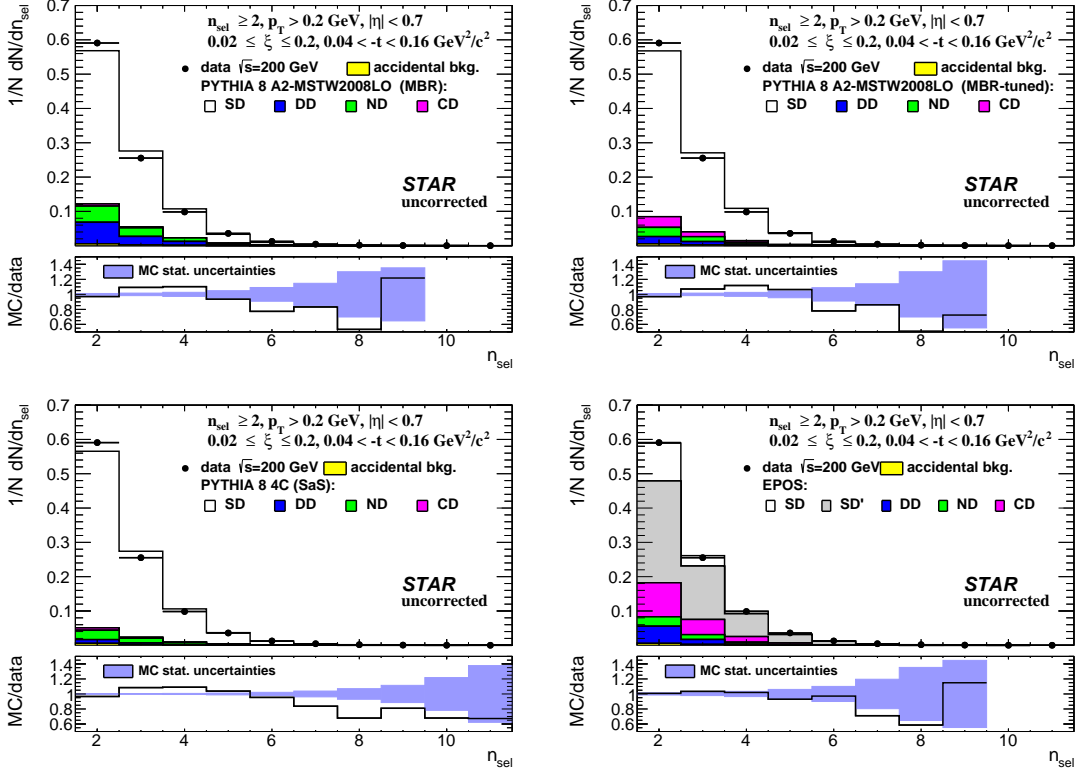


Figure 4.11: Uncorrected distributions of data compared to various MC models: (top left) PYTHIA 8 A2 (MBR), (top right) PYTHIA 8 A2 (MBR-tuned), (bottom left) PYTHIA 8 4C (SaS) and (bottom right) EPOS, as a function of n_{sel} . The ratio of MC predictions and data is shown in the bottom panels.

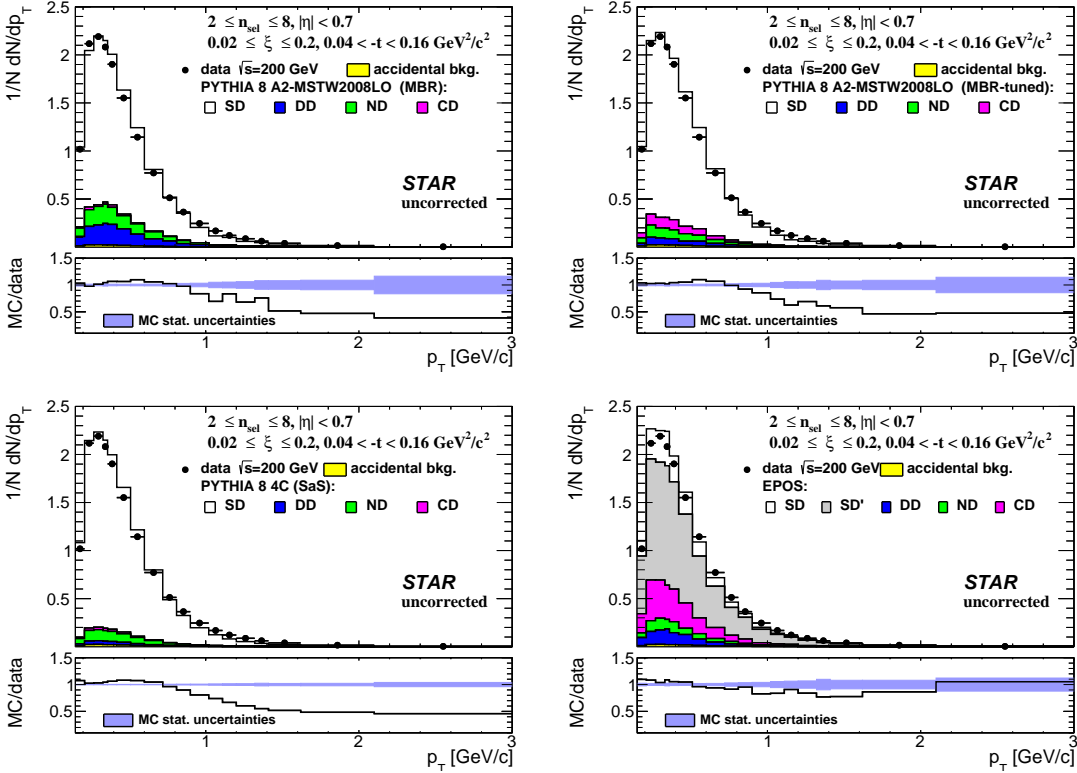


Figure 4.12: Uncorrected distributions of data compared to various MC models: (top left) PYTHIA 8 A2 (MBR), (top right) PYTHIA 8 A2 (MBR-tuned), (bottom left) PYTHIA 8 4C (SaS) and (bottom right) EPOS, as a function of p_T . The ratio of MC predictions and data is shown in the bottom panels.

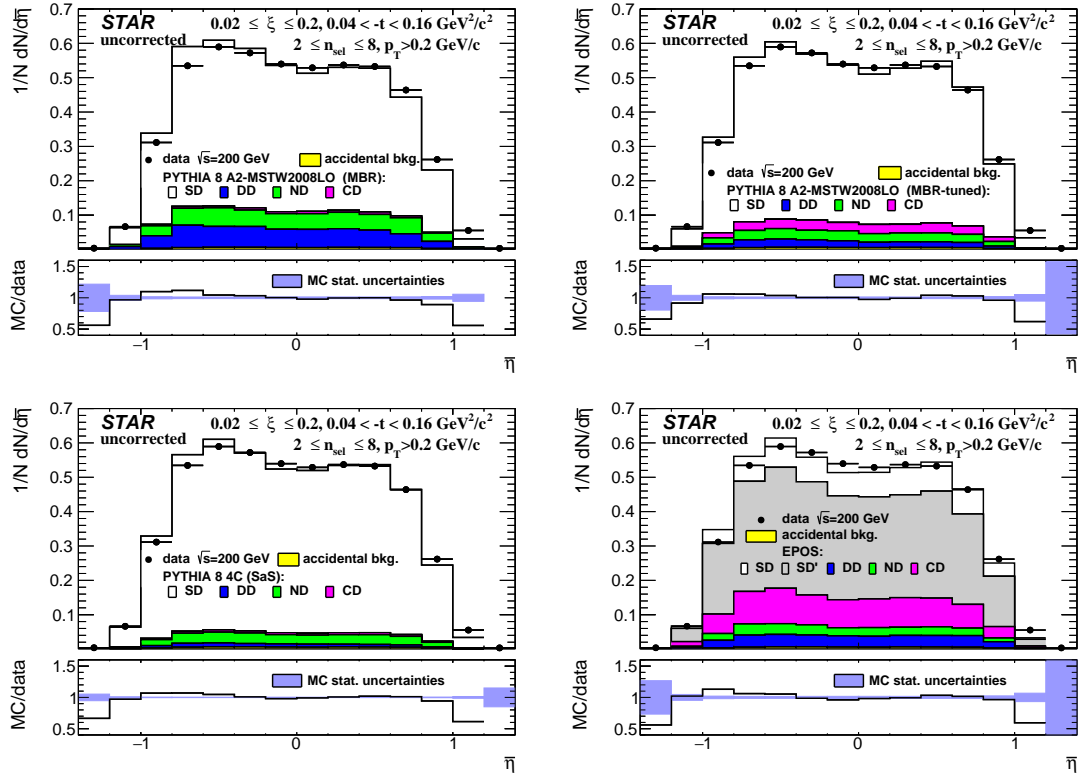


Figure 4.13: Uncorrected distributions of data compared to various MC models: (top left) PYTHIA 8 A2 (MBR), (top right) PYTHIA 8 A2 (MBR-tuned), (bottom left) PYTHIA 8 4C (SaS) and (bottom right) EPOS, as a function of $\bar{\eta}$. The ratio of MC predictions and data is shown in the bottom panels.

5. Selection Efficiencies

5.1 Vertex Reconstruction

When the charged-particle multiplicity is low, the vertex-finding algorithm sometimes fails to find the primary vertex. In addition, at high luminosity, vertex finder can fail due to the contribution of pile-up interactions, providing a wrong reconstructed vertex. In the study of vertex reconstruction efficiency we required at least two reconstructed global tracks $n_{\text{sel}}^{\text{global}} \geq 2$ passing all the quality cuts listed in Sec 3.1, except vertex-related cuts on DCA_{xy} and DCA_z , and associated to true-level primary particles. Additionally, MC events were accepted if the z -coordinate of the true-level primary vertex was between -80 and 80 cm and $n_{\text{ch}} \geq 2$. All corrections, described in this section, were calculated in three ranges of ξ separately using PYTHIA 8 SD embedding MC.

The global tracks (not necessarily associated to a true-level primary particles), which are used by the vertex-finder algorithm, had to pass the following quality cuts:

1. tracks must be matched with hits reconstructed in TOF,
2. the number of the TPC hits used in the helix fit $N_{\text{hits}}^{\text{fit}}$ must be greater than 20,
3. the ratio of the number of TPC hits used in the helix fit to the number of possible TPC hits $N_{\text{hits}}^{\text{fit}}/N_{\text{hits}}^{\text{poss}}$ must be greater than 0.52,
4. the transverse impact parameter with respect to the beamline d_0 must be less than 2 cm,
5. the track's transverse momentum p_T must be greater than 0.2 GeV/c.

The above track selection criteria are different than those used in the nominal analysis. Primary vertex reconstruction efficiency and fake vertex rate were calculated as a function of the number of global tracks used in vertexing $n_{\text{virt}}^{\text{global}}$ instead of $n_{\text{sel}}^{\text{global}}$ ($n_{\text{virt}}^{\text{global}} \geq n_{\text{sel}}^{\text{global}}$).

In the nominal analysis exactly one vertex with $n_{\text{sel}} \geq 2$ is required. However, in the study of vertex reconstruction, events with additional vertices were studied. Therefore, we define the best vertex as the reconstructed vertex with the highest number of TOF-matched tracks. This vertex does not have to be associated to true-level primary vertex (fake or secondary vertex). The algorithm, which matches reconstructed vertices to true-level vertices, checks for reconstructed tracks originating from them. If at least one reconstructed track is assigned to a true-level particle, then the reconstructed vertex is assigned to the true-level vertex from which the true-level particle originates. Since the fake vertices (not matched to the true-level primary vertex) are allowed in the analysis, the overall vertex-finding efficiency, $\epsilon_{\text{virt}}(n_{\text{virt}}^{\text{global}})$, is expressed as:

$$\epsilon_{\text{virt}}(n_{\text{virt}}^{\text{global}}) = \epsilon_{\text{virt}}^{\text{best}}(n_{\text{virt}}^{\text{global}}) + \delta_{\text{virt}}^{\text{fake}}(n_{\text{virt}}^{\text{global}}) \quad (5.1)$$

where:

$\epsilon_{\text{virt}}^{\text{best}}(n_{\text{virt}}^{\text{global}})$ is the primary vertex reconstruction efficiency, determined as the ratio of the number of good reconstructed events (best primary vertex with $n_{\text{sel}} \geq 2$ matched to the true-level primary vertex) to the number of input MC events,

$\delta_{\text{virt}}^{\text{fake}}(n_{\text{virt}}^{\text{global}})$ is the fake vertex rate, determined as the ratio of the number of good reconstructed events (best primary vertex with $n_{\text{sel}} \geq 2$ not matched to the true-level primary vertex) to the number of input MC events. Due to the contribution of pile-up, it is possible that the best vertex originates from fake tracks instead of true-level particles.

517 The vertex-finding efficiency as a function of $n_{\text{virt}}^{\text{global}}$, shown in Fig. 5.1 (left), is larger than 75% for
 518 all $n_{\text{virt}}^{\text{global}}$. However, for $n_{\text{virt}}^{\text{global}} > 8$, there are more fake than true-level primary vertices. When
 519 there are exactly two global tracks used in the vertex reconstruction, $n_{\text{virt}}^{\text{global}} = 2$, the vertex-
 520 finding efficiency depends on the longitudinal distance between these tracks $|\Delta z_0|$. Therefore,
 521 the vertex-finding efficiency for such events $\epsilon_{\text{virt}}(|\Delta z_0|)$ is given by:

$$\epsilon_{\text{virt}}(|\Delta z_0|) = \epsilon_{\text{virt}}^{\text{best}}(|\Delta z_0|) + \delta_{\text{virt}}^{\text{fake}}(|\Delta z_0|) \quad (5.2)$$

522 where: $\epsilon_{\text{virt}}^{\text{best}}(|\Delta z_0|)$ is the primary vertex reconstruction efficiency, $\delta_{\text{virt}}^{\text{fake}}(|\Delta z_0|)$ is the fake vertex
 523 rate.

524 Figure 5.1 (right) shows the vertex-finding efficiency for events with $n_{\text{virt}}^{\text{global}} = 2$. This efficiency
 525 is smaller than 20% for tracks with $|\Delta z_0| > 2$ cm, hence the analysis was limited to events with
 526 $|\Delta z_0| < 2$ cm, when $n_{\text{virt}}^{\text{global}} = 2$. The rate of fake vertices is negligibly low (open points overlap
 527 with full points).

528 Events are rejected if more vertices are reconstructed in addition to the best one. Rejected
 529 events can be classified as:

- 530 a) two or more additional vertices,
- 531 b) additional secondary vertex from interactions with the detector dead-material,
- 532 c) additional fake vertex,
- 533 d) additional primary vertex (vertex splitting or background vertex reconstructed as best ver-
 534 tex),
- 535 e) additional secondary vertex from the decay.

536 The fraction of such events, $f_{\text{virt}}^{\text{veto}}(n_{\text{virt}}^{\text{global}})$, is given by:

$$f_{\text{virt}}^{\text{veto}}(n_{\text{virt}}^{\text{global}}) = \frac{\text{number of events with more than one reconstructed TOF vertex}}{\text{number of events with at least one reconstructed TOF vertex}} \quad (5.3)$$

$$= f_a + f_b + f_c + f_d + f_e$$

537 where f_a to f_e are the fractions of events with additional vertices, with labels corresponding to
 538 the items in the listing above.

539 As before, the fraction was calculated as a function of $|\Delta z_0|$ for events with $n_{\text{virt}}^{\text{global}} = 2$.
 540 Figure 5.2 shows the fraction of multi-vertex events with respect to the $n_{\text{virt}}^{\text{global}}$. There is a large
 541 fraction of events (> 90%) with additional background vertices for $n_{\text{virt}}^{\text{global}} \geq 9$, what would result
 542 in large correction factor. Hence, the analysis was limited to events with $n_{\text{sel}}^{\text{global}} \leq 8$ ($n_{\text{sel}}^{\text{global}} \leq$

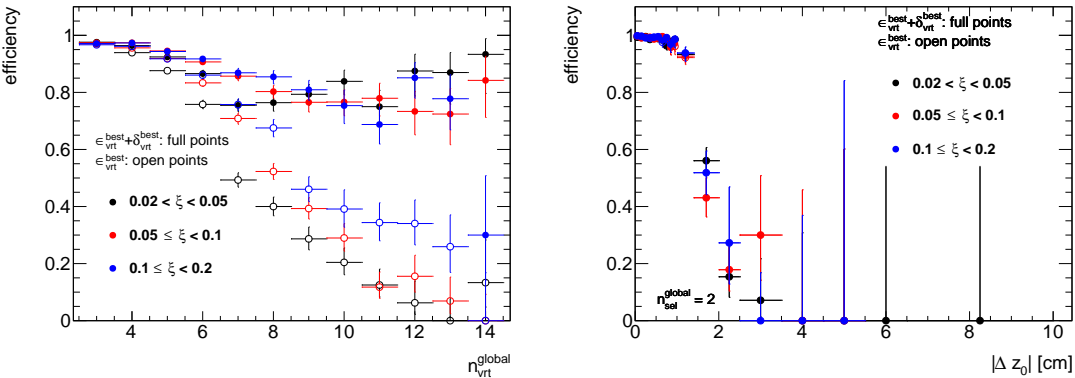


Figure 5.1: Vertex-finding efficiency in three ranges of ξ as a function of (left) $n_{\text{virt}}^{\text{global}}$ and (right)
 with respect to the $|\Delta z_0|$ between reconstructed tracks in events with $n_{\text{virt}}^{\text{global}} = 2$.

543 $n_{\text{vrt}}^{\text{global}}$). The total fraction of multi-vertex events, $f_a + f_b + f_c + f_d + f_e$, as a function of $n_{\text{vrt}}^{\text{global}}$
544 and $|\Delta z_0|$, shown in Fig. 5.3, demonstrates that $f_{\text{vrt}}^{\text{veto}}(|\Delta z_0|)$ is very small (< 2%) for events with
545 $n_{\text{vrt}}^{\text{global}} = 2$.

546 Although, the analysis was limited to $n_{\text{sel}}^{\text{global}} \leq 8$ ($n_{\text{sel}}^{\text{global}} \leq n_{\text{vrt}}^{\text{global}}$), a fraction of events with
547 additional background vertices was still relatively large. Since most of these additional vertices
548 are fake (and as accidental not correlated with true-level primary distributions), it was checked
549 whether the charged-particle multiplicity distributions are different for events with and without
550 reconstructed fake vertices. These distributions, as shown in Fig 5.4, are in good agreement, thus,
551 above studies of vertex reconstruction were repeated using MC events that do not contain recon-
552 structed fake vertices. It means that events with additional fake vertex were rejected (similarly to
553 the analysis of real data) and no correction is needed for such losses since it only affects overall
554 normalization (not the shapes of distributions under study). The vertex-finding efficiency, which
555 was calculated from such events, is shown in Fig. 5.5. It is greater than 95% for events with
556 $2 \leq n_{\text{vrt}}^{\text{global}} \leq 8$. In addition, the corresponding fraction of multi-vertex events, shown in Figs. 5.6

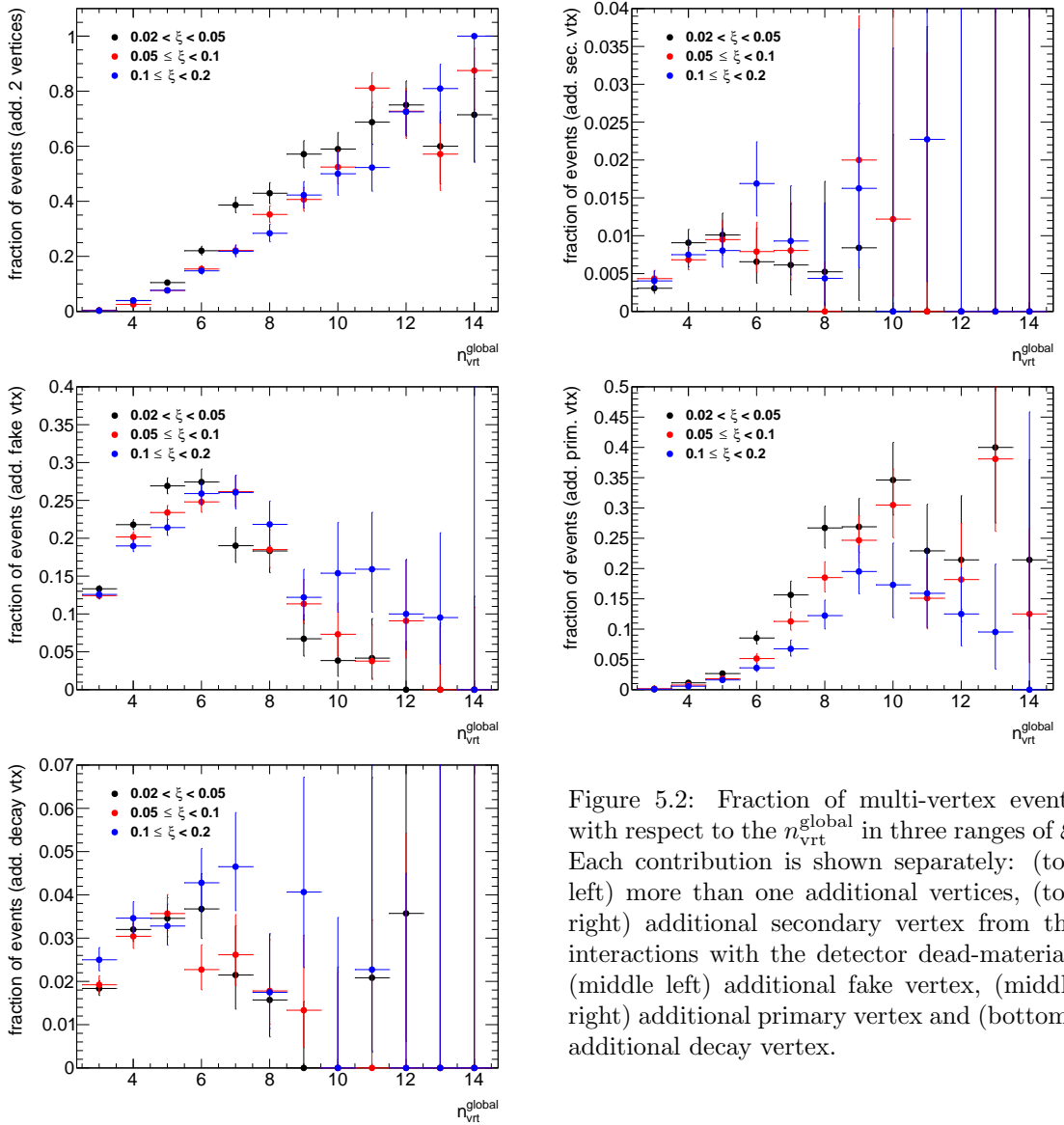


Figure 5.2: Fraction of multi-vertex events with respect to the $n_{\text{vrt}}^{\text{global}}$ in three ranges of ξ . Each contribution is shown separately: (top left) more than one additional vertices, (top right) additional secondary vertex from the interactions with the detector dead-material, (middle left) additional fake vertex, (middle right) additional primary vertex and (bottom) additional decay vertex.

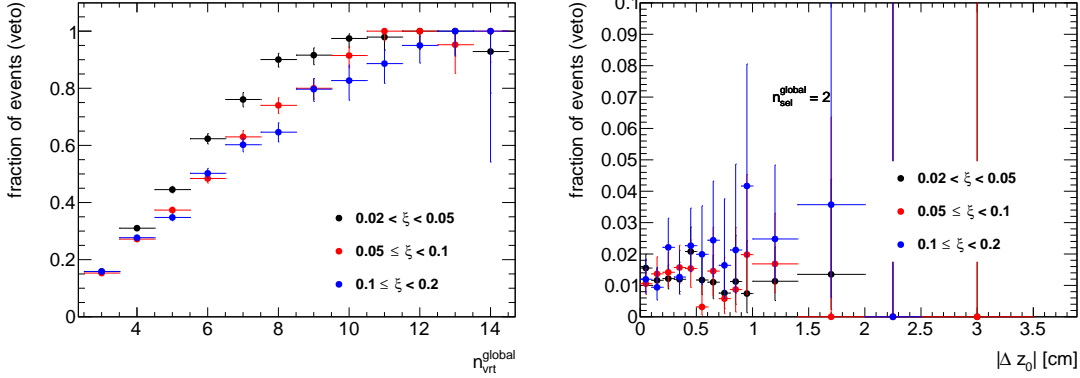


Figure 5.3: Total fraction of multi-vertex events as a function of (left) $n_{\text{vrt}}^{\text{global}}$ for events with $n_{\text{vrt}}^{\text{global}} > 2$ and (right) $|\Delta z_0|$ for events with $n_{\text{vrt}}^{\text{global}} = 2$ in three ranges of ξ .

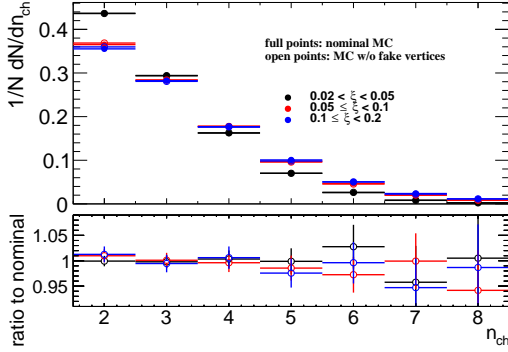


Figure 5.4: Normalized charged-particle multiplicity distributions in three ranges of ξ calculated from PYTHIA 8 SD embedding MC for (full points) all generated events and (open points) events without reconstructed fake vertices.

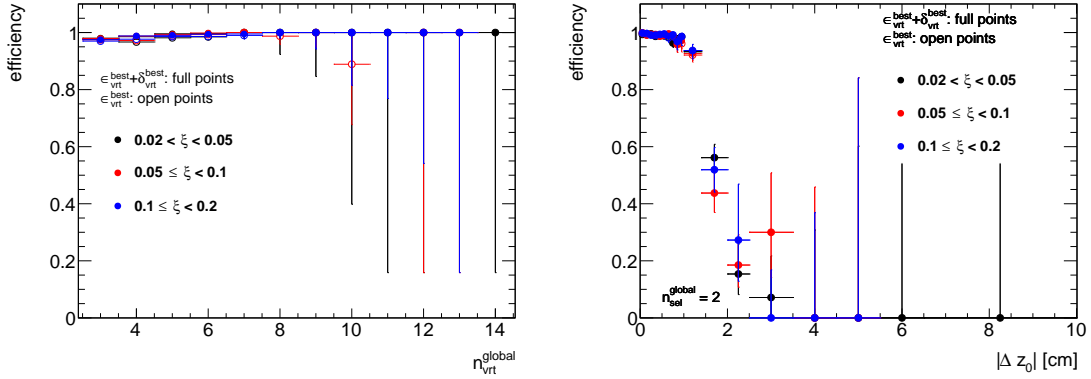


Figure 5.5: Vertex-finding efficiency in three ranges of ξ as a function of (left) $n_{\text{vrt}}^{\text{global}}$ and (right) with respect to the $|\Delta z_0|$ between reconstructed tracks in events with $n_{\text{vrt}}^{\text{global}} = 2$. Only events that do not contain additional fake vertices were used.

and 5.7, is smaller than 20%. Since fake vertices were rejected from this study, the f_c term from Eq. (5.3) is equal to 0. The correction factors calculated from MC events that do not contain reconstructed fake vertices were used in the analysis instead of the one obtained from the full MC sample.

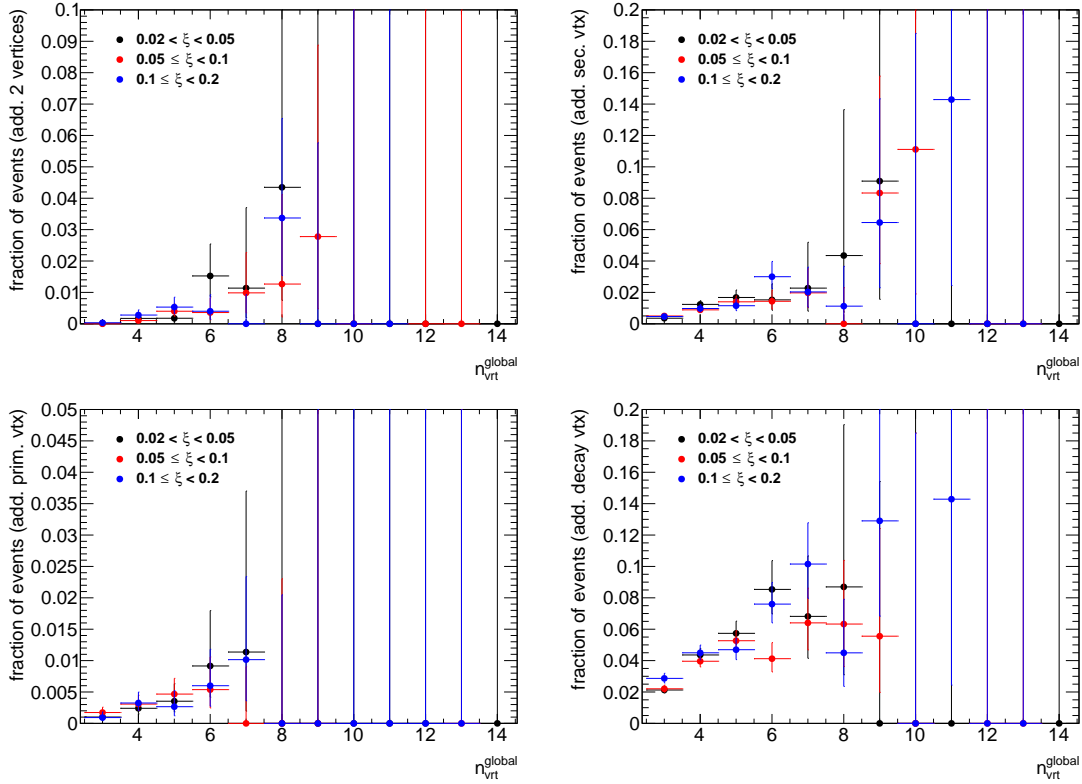


Figure 5.6: Fraction of multi-vertex events with respect to the $n_{\text{vrt}}^{\text{global}}$ in three ranges of ξ . Each contribution is shown separately: (top left) more than one additional vertices, (top right) additional secondary vertex from the interactions with the detector dead-material, (bottom left) additional primary vertex and (bottom right) additional decay vertex. Only events that do not contain additional fake vertices were used.

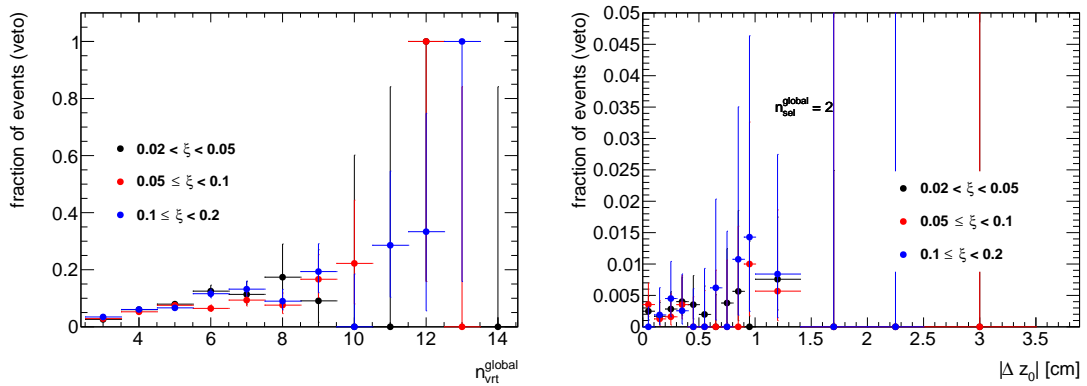


Figure 5.7: Total fraction of multi-vertex events as a function of (left) $n_{\text{vrt}}^{\text{global}}$ for events with $n_{\text{vrt}}^{\text{global}} > 2$ and (right) $|\Delta z_0|$ for events with $n_{\text{vrt}}^{\text{global}} = 2$ in three ranges of ξ . Only events that do not contain additional fake vertices were used.

5.2 Correction to BBC-Small

The SDT trigger conditions imposed a signal in RPs and a veto on any signal in the same-side small BBC tiles, whereas a signal in the opposite-side BBC-small was required by the offline event selection. These requirements were imposed in order to accept only events with rapidity gap and reduce DD, ND and accidental backgrounds. A joined BBC-small efficiency, ϵ_{BBC} , was obtained as a function of each measured quantity using PYTHIA 8 4C (SaS) SD embedded into Zerobias data, EPOS SD+SD' and HERWIG SD MC. The efficiency was calculated for events within fiducial region as follows:

$$\epsilon_{BBC} = \frac{\text{number of MC events satisfying the BBC-small selection criteria}}{\text{number of MC events}} \quad (5.4)$$

Figures 5.8 to 5.10 show the fraction of generated true-level MC events, within the fiducial region of the measurement, in which the selection criteria on BBC-small signal and veto are fulfilled. The efficiency weakly depends on the measured variables (n_{ch} , p_T and $\bar{\eta}$). In addition, veto, signal and joined BBC-small efficiencies are presented separately as a function of ξ in Fig. 5.11. The ϵ_{BBC} strongly depends on ξ and varies from about 90% for events with ξ within 0.02 – 0.05 to about 60% for events with $0.1 < \xi < 0.2$. However, measurements of corrected ξ distributions are out of the scope of this analysis.

Data is corrected for BBC-small efficiency using PYTHIA 8 4C (SaS). The uncertainty related to this correction is estimated by using HERWIG and EPOS SD+SD' samples, where the hadronization models are different from that used in PYTHIA 8. Figure 5.12 shows the PYTHIA 8 prediction on BBC efficiency divided by the HERWIG prediction in three ranges of ξ . The deviations between these two models are of the order of 4% at $0.02 < \xi < 0.05$, 2% at $0.05 < \xi < 0.1$ and about 10% at $0.1 < \xi < 0.2$. The differences between PYTHIA 8 and EPOS SD+SD' predictions are shown in Fig. 5.13. Most of them are of the order of 3%, except $n_{ch} \leq 3$ for which the difference varies up to 6%. The maximum difference between PYTHIA 8 and HERWIG/EPOS hadronization models is used as systematic uncertainty.

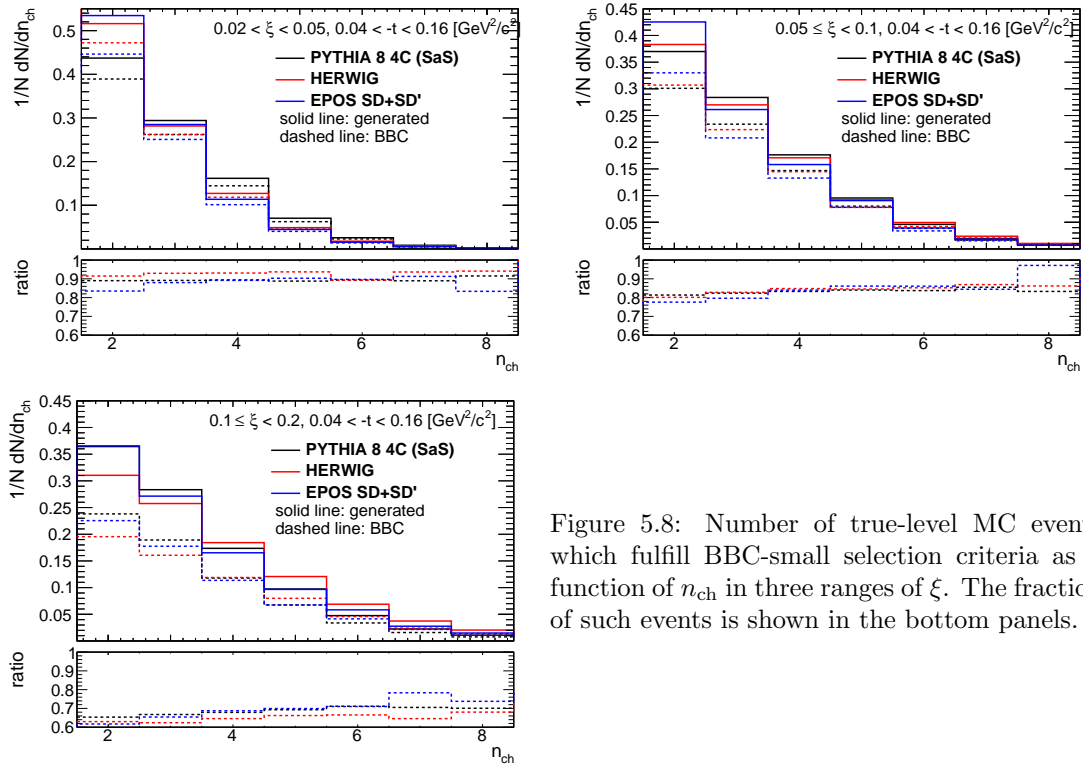


Figure 5.8: Number of true-level MC events which fulfill BBC-small selection criteria as a function of n_{ch} in three ranges of ξ . The fraction of such events is shown in the bottom panels.

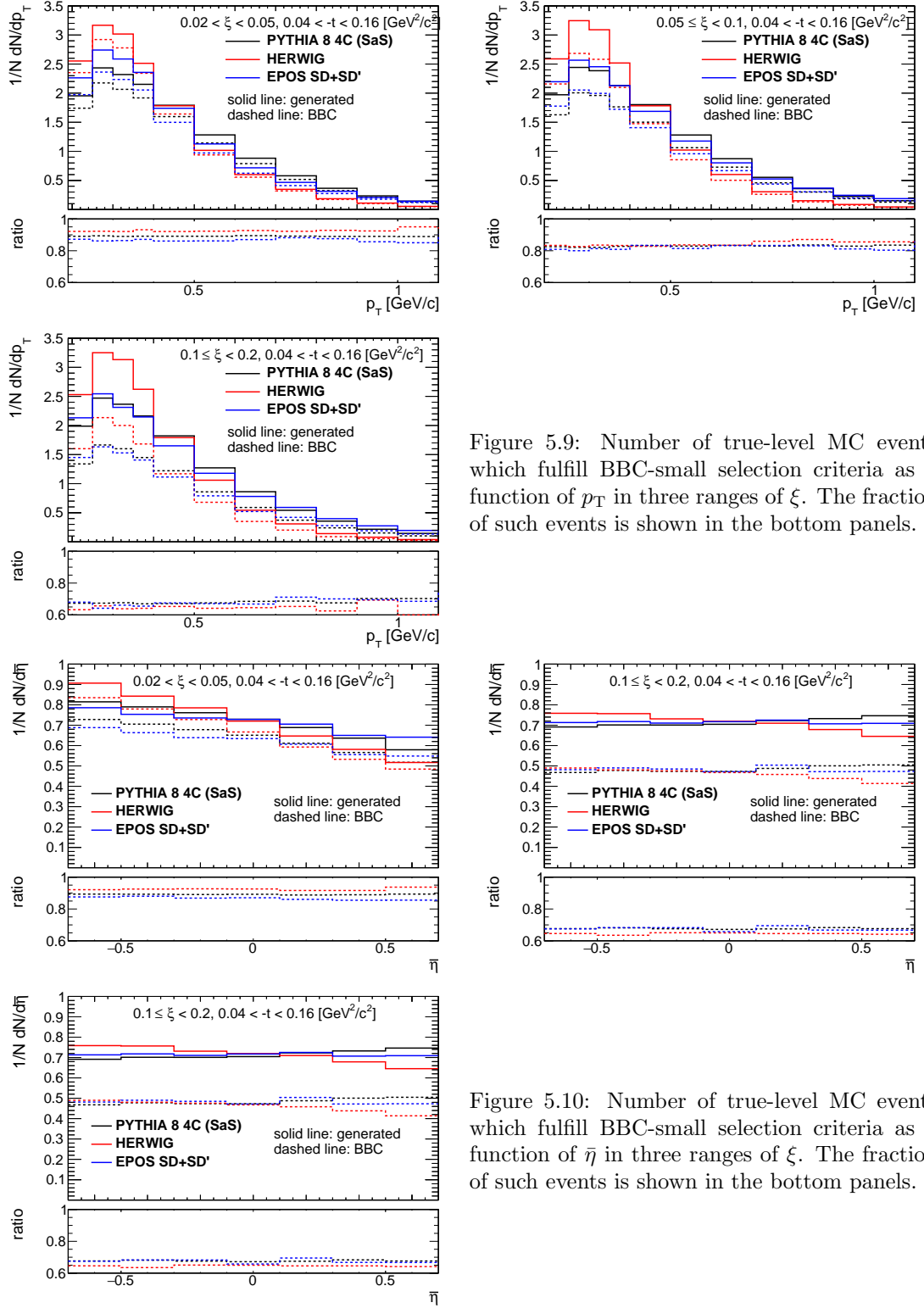


Figure 5.9: Number of true-level MC events which fulfill BBC-small selection criteria as a function of p_T in three ranges of ξ . The fraction of such events is shown in the bottom panels.

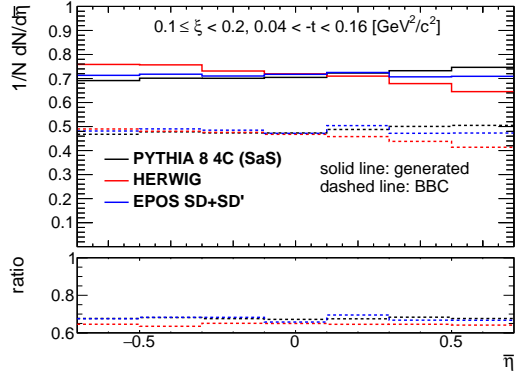


Figure 5.10: Number of true-level MC events which fulfill BBC-small selection criteria as a function of $\bar{\eta}$ in three ranges of ξ . The fraction of such events is shown in the bottom panels.

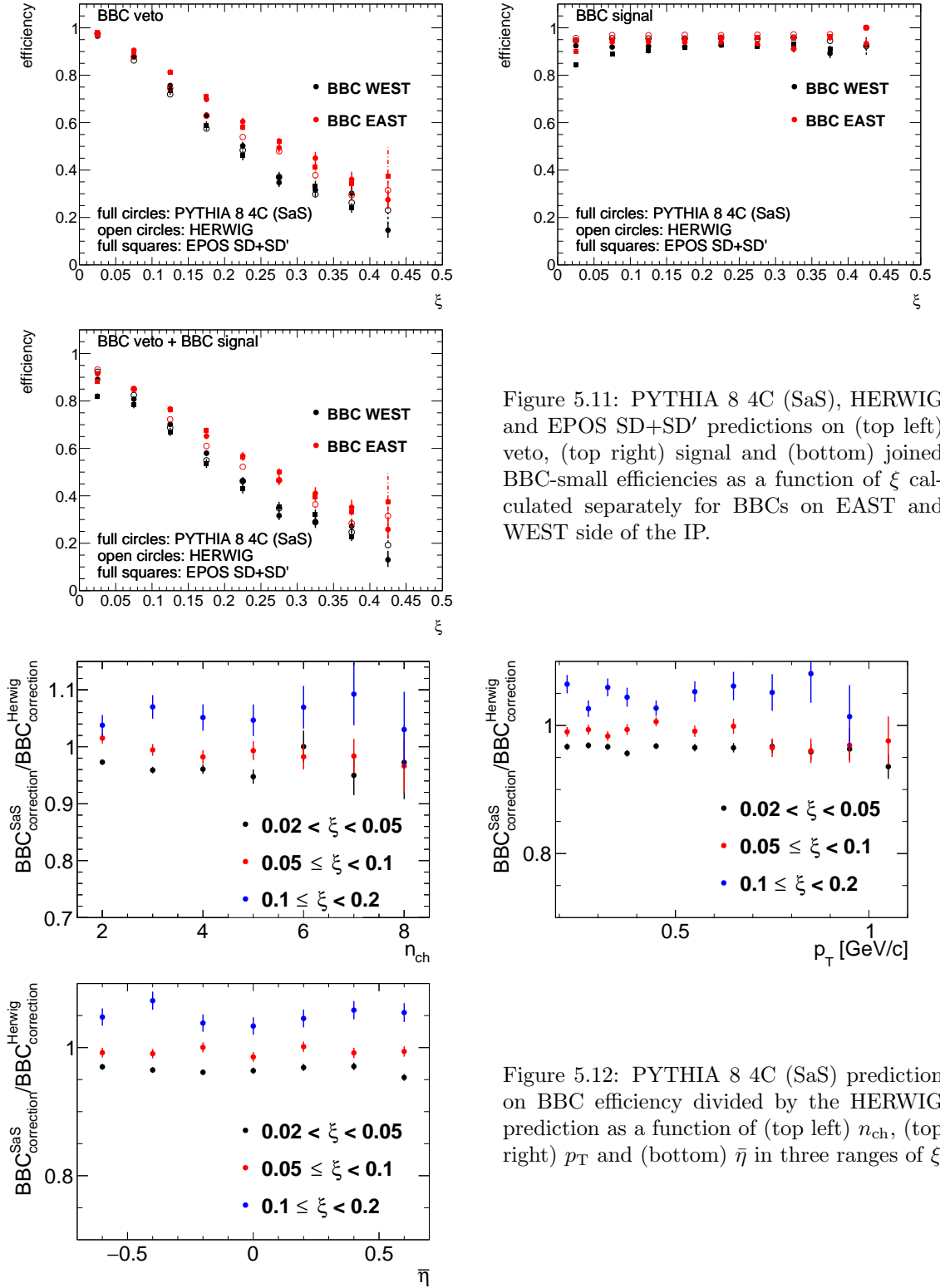


Figure 5.11: PYTHIA 8 4C (SaS), HERWIG and EPOS SD+SD' predictions on (top left) veto, (top right) signal and (bottom) joined BBC-small efficiencies as a function of ξ calculated separately for BBCs on EAST and WEST side of the IP.

Figure 5.12: PYTHIA 8 4C (SaS) prediction on BBC efficiency divided by the HERWIG prediction as a function of (top left) n_{ch} , (top right) p_T and (bottom) $\bar{\eta}$ in three ranges of ξ

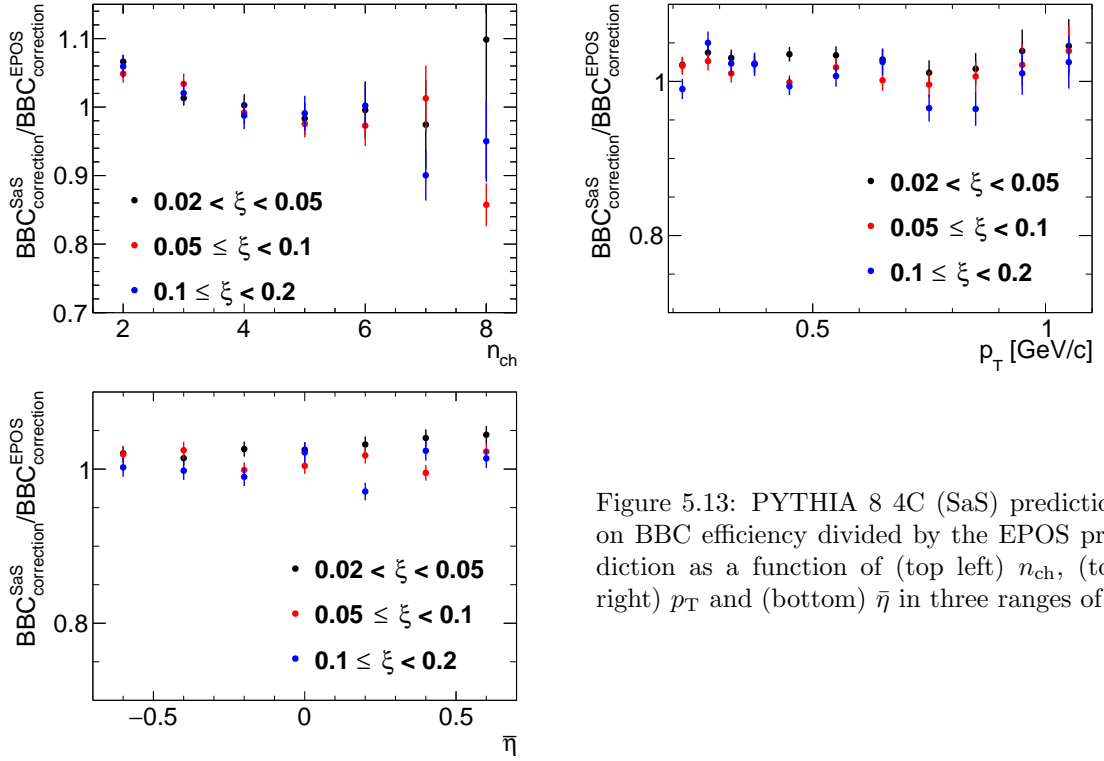


Figure 5.13: PYTHIA 8 4C (SaS) prediction on BBC efficiency divided by the EPOS prediction as a function of (top left) n_{ch} , (top right) p_{T} and (bottom) $\bar{\eta}$ in three ranges of ξ

6. Migrations into and out of the Fiducial Region

In this section the corrections due to the migrations of tracks and forward-scattered protons into and out of the fiducial region are described.

6.1 Migrations of Tracks into and out of the Fiducial Region

The procedure, described in this section, accounts for migrations of tracks into and out of the fiducial region, which originate from TPC resolution effects. The correction factor for such tracks, $f_{\text{okr}}(p_T, \eta)$ is defined as follows:

$$f_{\text{okr}}(p_T, \eta) = \frac{1 - f_{\text{okr}}^-(p_T, \eta)}{1 - f_{\text{okr}}^+(p_T, \eta)} \quad (6.1)$$

where $f_{\text{okr}}^-(p_T, \eta)$ is the fraction of reconstructed tracks for which the corresponding primary particle is outside of the kinematic range of the measurement and $f_{\text{okr}}^+(p_T, \eta)$ is the fraction of primary particles for which the corresponding reconstructed track is outside of the kinematic range of the measurement.

The resulting residual migrations, shown in Fig. 6.1, were estimated using PYTHIA 8 SD embedding MC. The main effect was observed at $|\eta| \sim 0.7$, where about 2 – 6% reconstructed tracks were associated to primary particle outside the fiducial region. However, above contributions to the correction factor, $f_{\text{okr}}(p_T, \eta)$, cancel each other and the resulting factor is about 2% at $|\eta| \sim 0.7$.

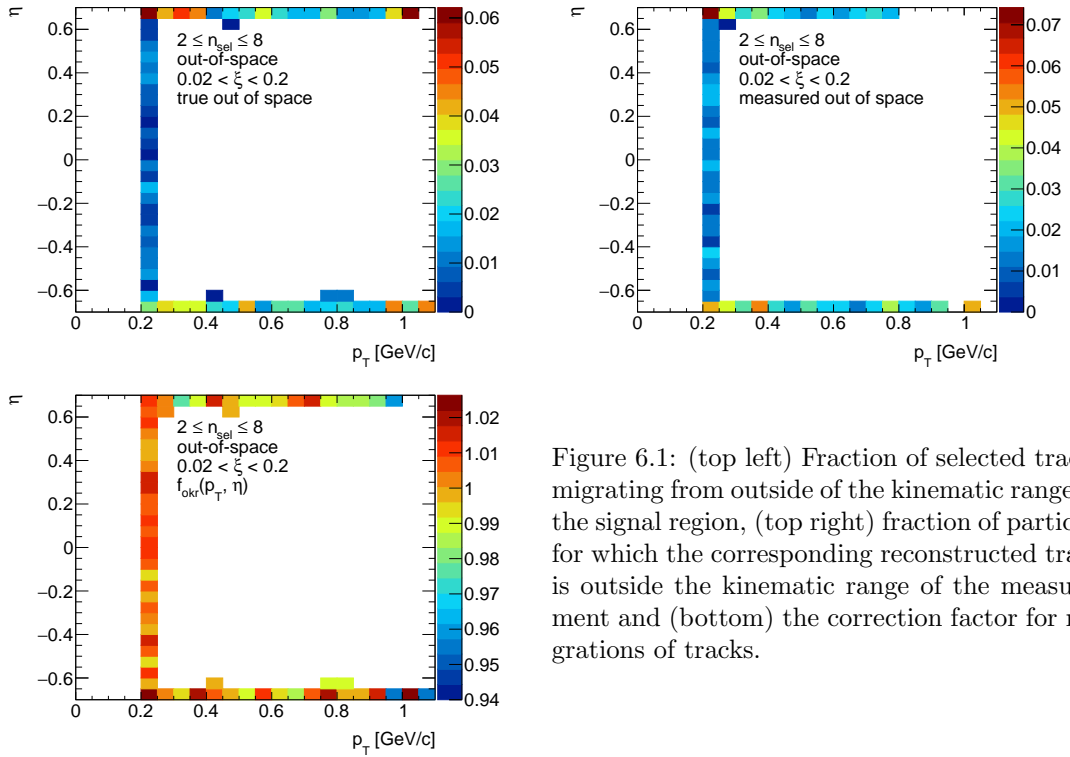


Figure 6.1: (top left) Fraction of selected tracks migrating from outside of the kinematic range to the signal region, (top right) fraction of particles for which the corresponding reconstructed track is outside of the kinematic range of the measurement and (bottom) the correction factor for migrations of tracks.

6.2 Migrations in ξ

The analysis was performed in three ranges of ξ . Thus, there are migrations into and out of these ξ regions. They mainly originate from the resolution of ξ reconstructed from RP tracks. Figure 6.2 shows the resolution of ξ as a function of the true-level ξ (denoted as ξ_{true}) with fitted zeroth order polynomial. The resolution of ξ is fairly constant and equals to about 0.3%.

The corrections due to migrations into and out of ξ regions was defined as:

$$f_\xi = \frac{1 - f_\xi^-}{1 - f_\xi^+} \quad (6.2)$$

where f_ξ^- is the fraction of events for which the corresponding true-level, ξ_{true} , is outside of the ξ region and f_ξ^+ is the fraction of events for which the corresponding reconstructed, ξ_{reco} , is outside of the ξ region.

The f_ξ was calculated for each measured variable separately. Figures 6.3 to 6.5 show the fraction of events f_ξ^- and f_ξ^+ as a function of n_{ch} , p_{T} and $\bar{\eta}$. The lower panel in each figure shows the corresponding correction factor f_ξ . The largest differences between migrations into and out of the ξ regions were observed at $0.02 < \xi < 0.05$, where they are of the order of 2 – 4%. In the other ξ regions, the difference between f_ξ^- and f_ξ^+ is smaller than 1%.

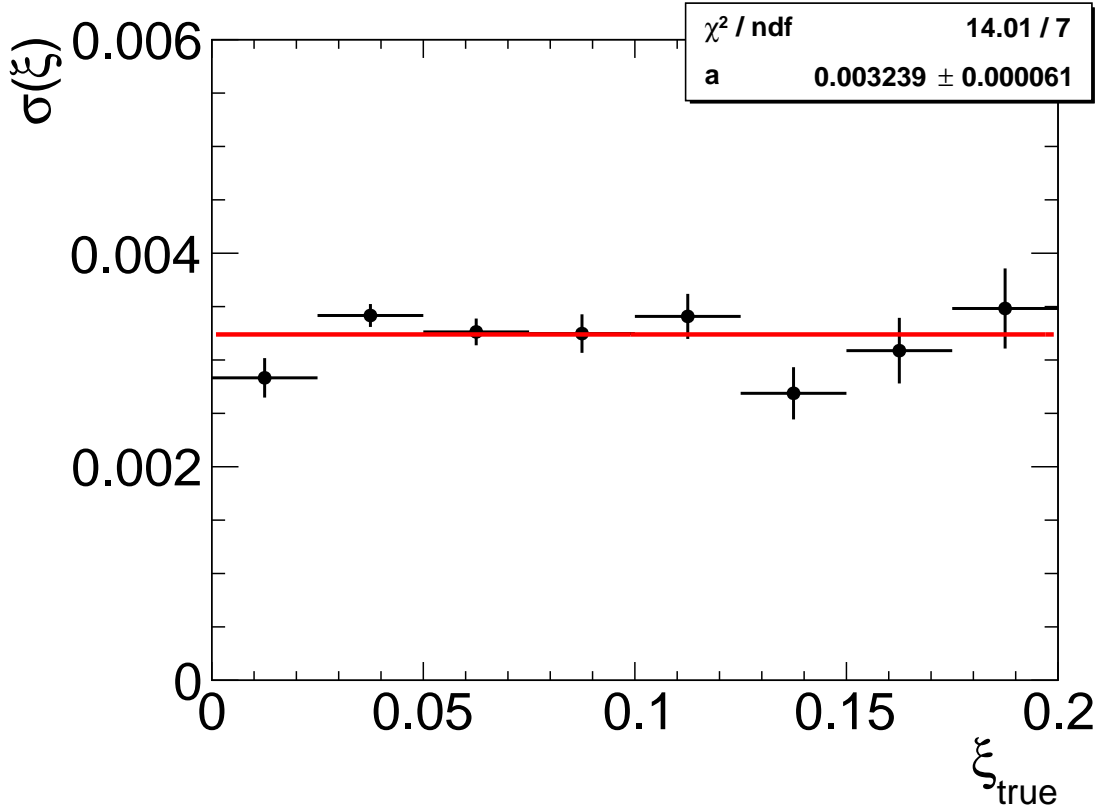


Figure 6.2: The resolution of ξ as a function of ξ_{true} . The zeroth order polynomial, shown as red line, was fitted.

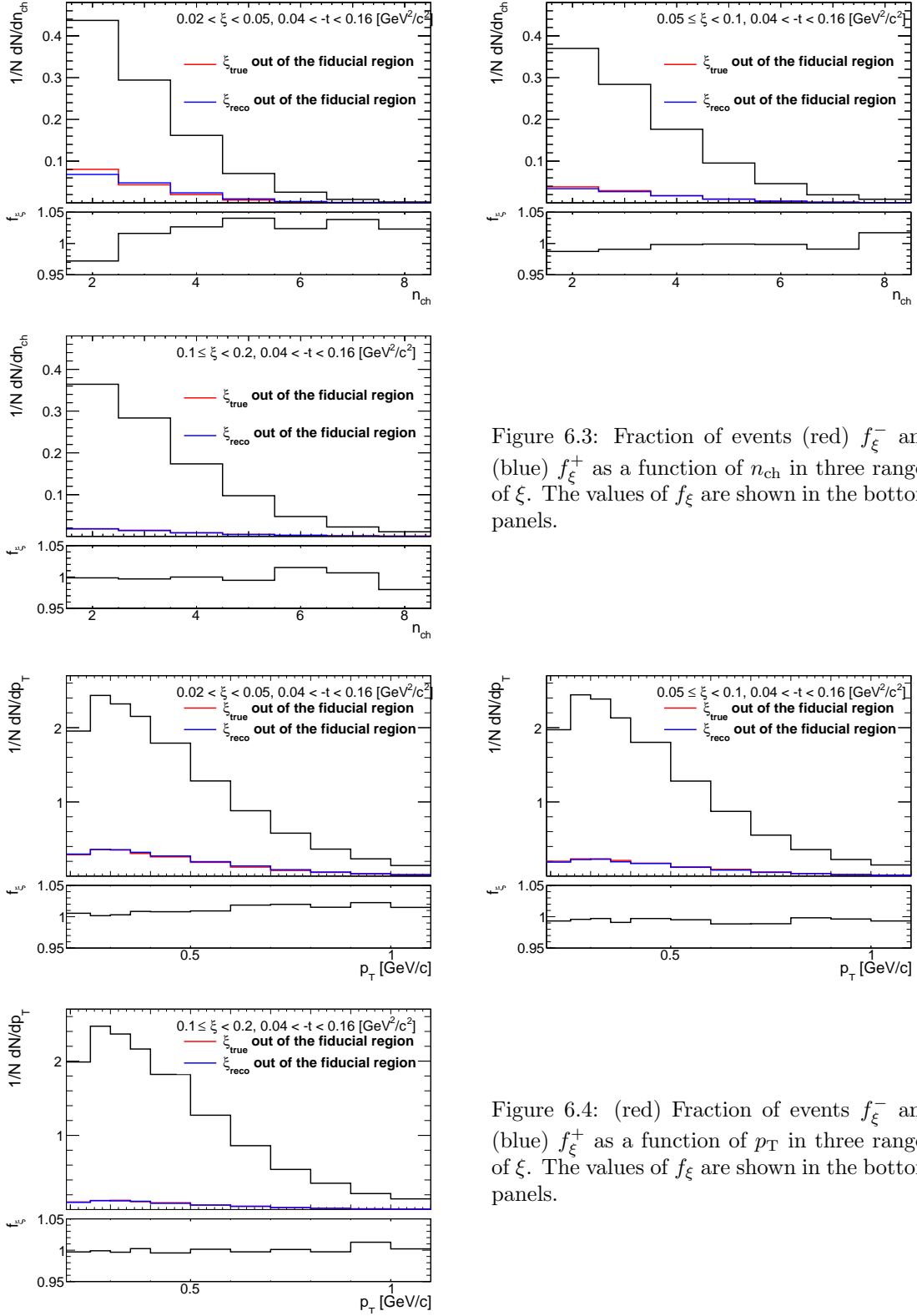


Figure 6.3: Fraction of events (red) f_ξ^- and (blue) f_ξ^+ as a function of n_{ch} in three ranges of ξ . The values of f_ξ are shown in the bottom panels.

Figure 6.4: (red) Fraction of events f_ξ^- and (blue) f_ξ^+ as a function of p_T in three ranges of ξ . The values of f_ξ are shown in the bottom panels.

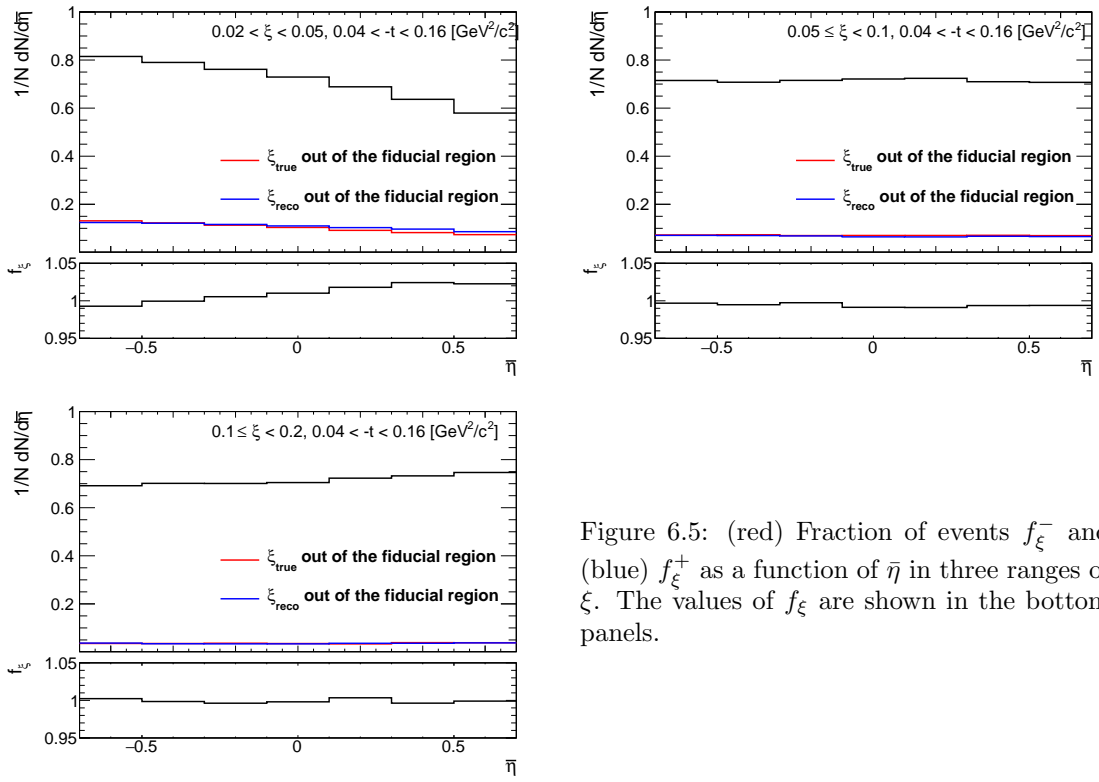


Figure 6.5: (red) Fraction of events f_ξ^- and (blue) f_ξ^+ as a function of $\bar{\eta}$ in three ranges of ξ . The values of f_ξ are shown in the bottom panels.

616 7. Event Corrections and 617 Unfolding Procedure

618 After subtraction of accidental, DD, CD and ND backgrounds (as described in Sec. 4 and 4.2),
619 the data was corrected for detector inefficiencies to obtain the distributions of charged particles
620 and particle to antiparticle (pion, kaon, proton and their antiparticle) multiplicity ratios. These
621 corrections include:

- 622 • event-by-event weights due to vertex reconstruction efficiency:

$$w_{\text{ev}}^{\text{vrt}}(n_{\text{vrt}}^{\text{global}}, |\Delta z_0|) = \frac{1}{\epsilon_{\text{vrt}}(n_{\text{vrt}}^{\text{global}}, |\Delta z_0|)} \cdot \frac{1}{1 - f_{\text{veto}}(n_{\text{vrt}}^{\text{global}}, |\Delta z_0|)} \quad (7.1)$$

623 where the $|\Delta z_0|$ dependence is only applicable for events with $n_{\text{vrt}}^{\text{global}} = 2$ as described in
624 Sec. 5.1.

- 625 • track-by-track weights due to track reconstruction efficiency, track backgrounds, migrations
626 of tracks into and out of the fiducial region:

$$w_{\text{trk}}(p_T, \eta, V_z) = \frac{1 - f_{\text{bkg}}(p_T, \eta) - f_{\text{fake}}(p_T, \eta)}{\epsilon_{\text{TPC}}(p_T, \eta, V_z) \epsilon_{\text{TOF}}(p_T, \eta, V_z)} f_{\text{okr}}(p_T, \eta) \quad (7.2)$$

627 where: $\epsilon_{\text{TPC}}(p_T, \eta, V_z)$ is TPC track reconstruction efficiency [1], $\epsilon_{\text{TOF}}(p_T, \eta, V_z)$ is TOF
628 matching efficiency [1], $f_{\text{okr}}(p_T, \eta)$ is a factor accounting for migrations of tracks into and
629 out of the fiducial region, $f_{\text{bkg}}(p_T, \eta)$ is a fraction of background tracks, and $f_{\text{fake}}(p_T, \eta)$
630 is a fraction of fake tracks. These corrections were not applied for n_{ch} measurements since
631 they were taken into account in the unfolding procedure.

- 632 • event-by-event (for n_{ch} distribution) or track-by-track (for $p_T, \bar{\eta}$ distributions) weights, f_ξ ,
633 due to migrations of events between three ξ regions.

634 Additionally, the obtained distributions were corrected for BBC-small efficiency, ϵ_{BBC} , using
635 the following weight, which was calculated for each true-level quantity $(n_{\text{ch}}, p_T, \bar{\eta})$ in three ranges
636 of ξ separately:

$$w_{\text{BBC}} = \frac{1}{\epsilon_{\text{BBC}}} \quad (7.3)$$

637 In the following sections, the correction procedure for each of the measured distributions is
638 presented separately.

639 7.1 Correction to dN/dn_{sel}

640 In order to express the multiplicity distribution in terms of the number of charged particles, n_{ch} ,
641 instead of the number of selected tracks, n_{sel} , the following procedure based on the Bayesian un-
642 folding [14, 15] was used. First, the n_{sel} distribution was corrected for vertex reconstruction effects
643 by applying event-by-event weights, $w_{\text{ev}}^{\text{vrt}}(n_{\text{vrt}}^{\text{global}}, |\Delta z_0|)$. The number of events in which n_{ch} are
644 produced, $N_{\text{ev}}(n_{\text{ch}})$, can be associated with the number of events in which n_{sel} are reconstructed,
645 $N_{\text{ev}}(n_{\text{sel}})$. Since there are several possible n_{sel} observed in n_{ch} event, $N_{\text{ev}}(n_{\text{ch}})$ is given by:

$$\begin{aligned} N_{\text{ev}}(n_{\text{ch}}) &= \sum_{n_{\text{sel}}=0}^8 P(n_{\text{ch}}|n_{\text{sel}}) \cdot N_{\text{ev}}(n_{\text{sel}}) \\ &= \frac{1}{\epsilon_m(n_{\text{ch}})\epsilon_r(n_{\text{ch}})} \sum_{n_{\text{sel}}=2}^8 P(n_{\text{ch}}|n_{\text{sel}}) \cdot N_{\text{ev}}(n_{\text{sel}}) \end{aligned} \quad (7.4)$$

646 where:

647 $P(n_{\text{ch}}|n_{\text{sel}})$ is the conditional probability of having n_{ch} charged particles in an event in which
 648 n_{sel} tracks were found,

649 $\epsilon_m(n_{\text{ch}})$ is a factor, which recovers events that are lost due to TPC track reconstruction and TOF
 650 matching inefficiencies, i.e. those with $n_{\text{ch}} \geq 2$ but $n_{\text{sel}} < 2$,

651 $\epsilon_r(n_{\text{ch}})$ is a factor, which recovers events which are lost due to fake tracks, i.e. those with $n_{\text{ch}} \leq 8$
 652 but $n_{\text{sel}} > 8$. It was checked that this effect is negligible (smaller than 1%) and can be
 653 omitted.

654 Figure 7.1 shows $\epsilon_m(n_{\text{ch}})$ in three ranges of ξ . It was derived from PYTHIA 8 embedding MC
 655 and varies from about 25% for $n_{\text{ch}} = 2$ to 95% for $n_{\text{ch}} = 8$. Since there are additional data-driven
 656 corrections to TPC and TOF efficiencies, MC simulations were modified by randomly removing
 657 or adding tracks. This was done in accordance with differences in the efficiencies between data
 658 and MC. Figure 7.2 shows $\epsilon_m(n_{\text{ch}})$ calculated in three ranges of ξ using no-pile-up PYTHIA 8 and
 659 EPOS SD+SD'. The differences between these two models, which are up to 12% for $n_{\text{ch}} = 2$ and
 660 $0.02 < \xi < 0.05$, were symmetrized and taken as a systematic uncertainty.

661 The probability $P(n_{\text{ch}}|n_{\text{sel}})$ can be derived using Bayes' theorem, which can be stated mathematically
 662 in terms of charged particle and charged track multiplicities as:

$$P(n_{\text{sel}}|n_{\text{ch}}) \cdot P(n_{\text{ch}}) = P(n_{\text{ch}}|n_{\text{sel}}) \cdot P(n_{\text{sel}}) \quad (7.5)$$

663 where: $P(n_{\text{sel}})$ and $P(n_{\text{ch}})$ are probabilities of observing n_{sel} and n_{ch} respectively, $P(n_{\text{ch}}|n_{\text{sel}})$ and
 664 $P(n_{\text{sel}}|n_{\text{ch}})$ are conditional probabilities.

665 In order to improve the estimate of $P(n_{\text{ch}}|n_{\text{sel}})$, the unfolding is done iteratively:

- 666 • In the first iteration, it is assumed that:

$$P(n_{\text{ch}}|n_{\text{sel}}) = P = P^{\text{MC}}(n_{\text{sel}}|n_{\text{ch}}) \frac{P^{\text{MC}}(n_{\text{ch}})}{P^{\text{MC}}(n_{\text{sel}})} \quad (7.6)$$

$$N_{\text{ev}}(n_{\text{ch}}) = \frac{1}{\epsilon_m(n_{\text{ch}})} \sum_{n_{\text{sel}}=2}^8 N_{\text{ev}}(n_{\text{sel}}) \cdot P \quad (7.7)$$

669 where $P^{\text{MC}}(n_{\text{sel}}|n_{\text{ch}})$, $P^{\text{MC}}(n_{\text{ch}})$ and $P^{\text{MC}}(n_{\text{sel}})$ are obtained from MC. $P^{\text{MC}}(n_{\text{sel}}|n_{\text{ch}})$ is
 670 the same for each iteration.

- 671 • In the $(i + 1)$ th iteration we have:

$$P^{i+1} = P^{\text{MC}}(n_{\text{sel}}|n_{\text{ch}}) \frac{N_{\text{ev}}^i(n_{\text{ch}})}{N_{\text{ev}}(n_{\text{sel}})} \quad (7.8)$$

$$N_{\text{ev}}^{i+1}(n_{\text{ch}}) = \frac{1}{\epsilon_m(n_{\text{ch}})} \sum_{n_{\text{sel}}=2}^8 N_{\text{ev}}(n_{\text{sel}}) \cdot P^{i+1} \quad (7.9)$$

673 where $N_{\text{ev}}^i(n_{\text{ch}})$ is calculated in the previous iteration, and $N_{\text{ev}}(n_{\text{sel}})$ is taken from data.

674 The unfolding matrices $P(n_{\text{ch}}|n_{\text{sel}})$ for each ξ region, shown in Fig. 7.3, were obtained from
 675 PYTHIA 8 embedding MC and used in all iterations of the above procedure. Similarly to $\epsilon_m(n_{\text{ch}})$,
 676 the matrices were modified by randomly removing or adding tracks in order to take into account
 677 additional data-driven corrections to TPC and TOF efficiencies. In order to increase statistical
 678 precision of the unfolding matrices, all simulated events were used, i.e. also those with additional
 679 fake vertices (with n_{sel} defined as a number of primary tracks associated with the best vertex).
 680 The systematic uncertainty related to limited statistics in PYTHIA 8 was estimated by performing
 681 50 pseudo-experiments, in which the unfolding matrices were smeared according to their statistical

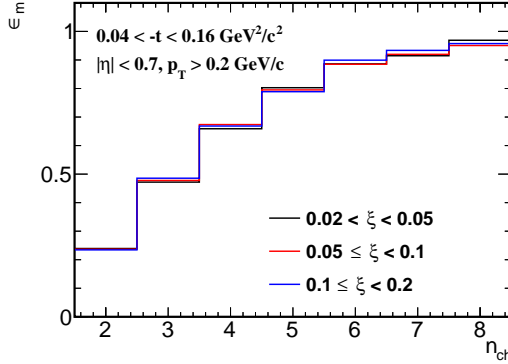


Figure 7.1: $\epsilon_m(n_{ch})$ calculated separately in three ranges of ξ using PYTHIA 8 embedding MC.

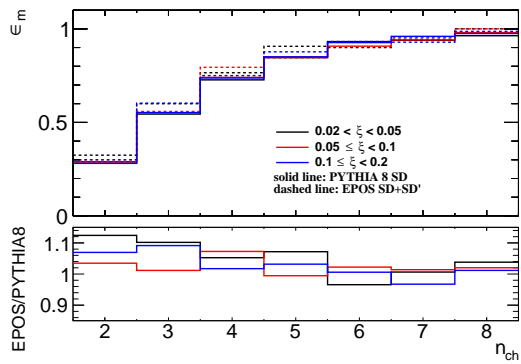


Figure 7.2: Comparison of $\epsilon_m(n_{ch})$ calculated separately in three ranges of ξ using PYTHIA 8 SD and EPOS SD+SD' no-pile-up MCs. The ratios of EPOS to PYTHIA 8 predictions are shown in the bottom panel.

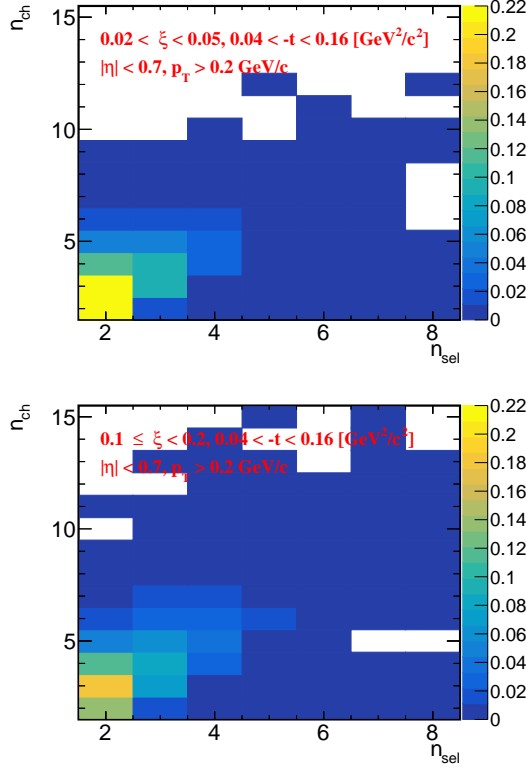


Figure 7.3: The unfolding matrices calculated from PYTHIA 8 embedding MC for three ranges of ξ separately.

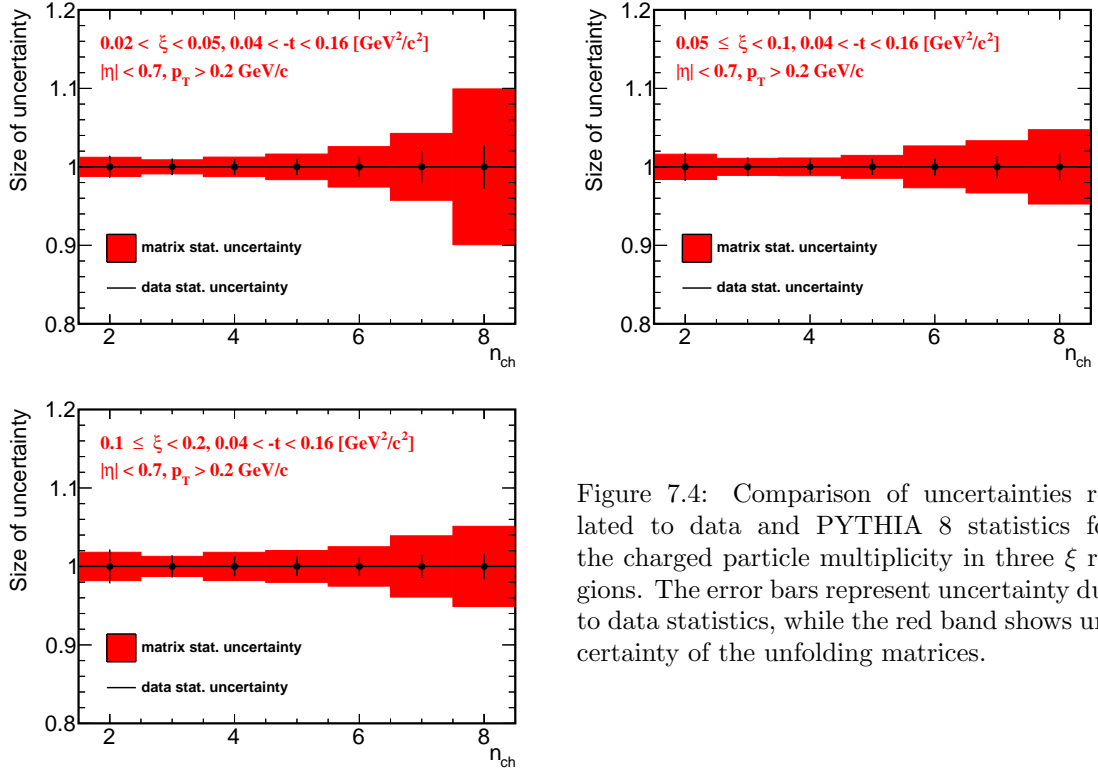


Figure 7.4: Comparison of uncertainties related to data and PYTHIA 8 statistics for the charged particle multiplicity in three ξ regions. The error bars represent uncertainty due to data statistics, while the red band shows uncertainty of the unfolding matrices.

uncertainties. It affects mainly large charged-particle multiplicities, where it is about 8 – 10% (as shown in Fig. 7.4), and is smaller or at the same level as other components contributing to the total systematic uncertainty.

The distribution dN/dn_{ch} obtained after the unfolding procedure was corrected for BBC-small efficiency, through $w_{\text{BBC}}(n_{\text{ch}})$ weights, and migrations of events between ξ ranges, through $f_{\xi}(n_{\text{ch}})$ weights. Since the unfolding matrices contain track reconstruction efficiencies, non-primary track backgrounds, migrations of tracks into and out of the fiducial region, the weight $w_{\text{trk}}(p_{\text{T}}, \eta, V_z)$ was not used.

Finally, the dN/dn_{ch} distribution was normalized to the total number of events, $N_{\text{ev}} = N$, which was calculated as the integral of the unfolded distribution.

7.2 Correction to Transverse Momentum and Pseudorapidity Distributions

First the accidental and non-SD backgrounds were subtracted from the p_{T} and $\bar{\eta}$ distributions. Next, each event was corrected for vertex reconstruction efficiency by applying $w_{\text{ev}}^{\text{vrt}}(n_{\text{vrt}}^{\text{global}}, |\Delta z_0|)$ weights. Then, the tracks were corrected for the track reconstruction efficiency, non-primary track background contribution, track and ξ migrations, BBC-small efficiency (the product of $w_{\text{trk}}(p_{\text{T}}, \eta, V_z)$, f_{ξ} and w_{BBC} weights was applied, f_{ξ} and w_{BBC} were calculated as a function of true-level p_{T} and $\bar{\eta}$ separately).

In order to obtain charged-particle densities, the p_{T} and $\bar{\eta}$ distributions were normalized to unity and scaled by the average charged particle multiplicity in an event $\langle n_{\text{ch}} \rangle$. The latter was calculated from the corrected charged particle multiplicity distribution dN/dn_{ch} (Sec. 7.1). The above procedure was done to correct the data also for events that are lost due to $n_{\text{sel}} < 2$ but $n_{\text{ch}} \geq 2$ since such correction was not included in any event-by-event and track-by-track weights. There was an assumption that p_{T} and η distributions are the same for lost and measured events, but it

706 was validated by the closure tests (Sec. 7.3). The mean p_T and $\bar{\eta}$ in an event, $\langle p_T \rangle$ and $\langle \bar{\eta} \rangle$, were
707 obtained from the measured distributions.

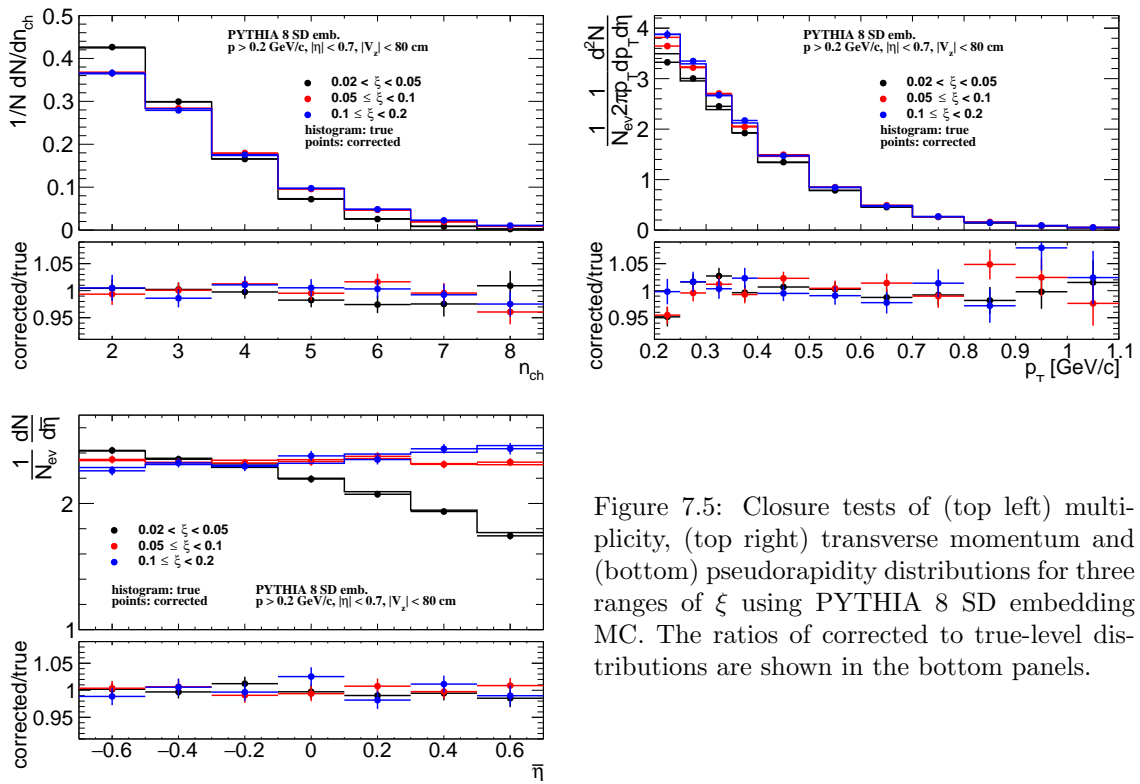
708 7.3 Closure Tests

709 In order to validate the correction procedures, closure tests were performed, i.e. full correction
710 procedure was applied to the MC detector-level distributions and the results were directly com-
711 pared to the true-level distributions. Figure 7.5 shows closure tests of multiplicity, transverse
712 momentum and pseudorapidity distributions for three ranges of ξ , separately. PYTHIA 8 SD
713 embedding MC was used as an input. In order to compare corrected and true-level distributions,
714 the statistical uncertainties of the true-level distributions were assumed to be 0. The difference
715 between true-level and corrected distributions was taken as a systematic uncertainties.

716 7.4 EAST-WEST asymmetry

717 Another kind of consistency check can be performed by comparing the results obtained by tag-
718 ging forward-scattered protons in different detectors. Therefore, each distribution was measured
719 separately for events in which forward-scattered proton is on one and the other side of the IP
720 (east-west). Figure 7.6 shows the tests of multiplicity, transverse momentum and pseudorapidity
721 distributions for three ranges of ξ , separately. Both statistical uncertainty components, due to
722 input data and due to unfolding matrix, are added in quadrature for n_{ch} distributions. The largest
723 difference is observed for charged-particle multiplicity distributions, where it varies up to 20% for
724 $n_{ch} = 8$ and $0.02 < \xi < 0.1$. For the rest multiplicities and ξ ranges, the differences are smaller
725 ($< 10\%$). In case of p_T and $\bar{\eta}$ distributions, a level of these disagreements is below 5%.

726 The deviations between the distributions for events with forward-scattered proton on east and
727 west side of the IP were fitted with a constant (Fig. 7.6). The quality of the fit shows that the
728 disagreements are compatible with statistical fluctuations (χ^2/ndf close to 1) for multiplicity and
729 transverse momentum distributions. For pseudorapidity, the χ^2/ndf is significantly larger than 1.



727
728
729
730
731
732
733
734
735
736
737
738
739
740
741
742
743
744
745
746
747
748
749
750
751
752
753
754
755
756
757
758
759
760
761
762
763
764
765
766
767
768
769
770
771
772
773
774
775
776
777
778
779
780
781
782
783
784
785
786
787
788
789
790
791
792
793
794
795
796
797
798
799
800
801
802
803
804
805
806
807
808
809
810
811
812
813
814
815
816
817
818
819
820
821
822
823
824
825
826
827
828
829
830
831
832
833
834
835
836
837
838
839
840
841
842
843
844
845
846
847
848
849
850
851
852
853
854
855
856
857
858
859
860
861
862
863
864
865
866
867
868
869
870
871
872
873
874
875
876
877
878
879
880
881
882
883
884
885
886
887
888
889
890
891
892
893
894
895
896
897
898
899
900
901
902
903
904
905
906
907
908
909
910
911
912
913
914
915
916
917
918
919
920
921
922
923
924
925
926
927
928
929
930
931
932
933
934
935
936
937
938
939
940
941
942
943
944
945
946
947
948
949
950
951
952
953
954
955
956
957
958
959
960
961
962
963
964
965
966
967
968
969
970
971
972
973
974
975
976
977
978
979
980
981
982
983
984
985
986
987
988
989
990
991
992
993
994
995
996
997
998
999
1000
1001
1002
1003
1004
1005
1006
1007
1008
1009
1010
1011
1012
1013
1014
1015
1016
1017
1018
1019
1020
1021
1022
1023
1024
1025
1026
1027
1028
1029
1030
1031
1032
1033
1034
1035
1036
1037
1038
1039
1040
1041
1042
1043
1044
1045
1046
1047
1048
1049
1050
1051
1052
1053
1054
1055
1056
1057
1058
1059
1060
1061
1062
1063
1064
1065
1066
1067
1068
1069
1070
1071
1072
1073
1074
1075
1076
1077
1078
1079
1080
1081
1082
1083
1084
1085
1086
1087
1088
1089
1090
1091
1092
1093
1094
1095
1096
1097
1098
1099
1100
1101
1102
1103
1104
1105
1106
1107
1108
1109
1110
1111
1112
1113
1114
1115
1116
1117
1118
1119
1120
1121
1122
1123
1124
1125
1126
1127
1128
1129
1130
1131
1132
1133
1134
1135
1136
1137
1138
1139
1140
1141
1142
1143
1144
1145
1146
1147
1148
1149
1150
1151
1152
1153
1154
1155
1156
1157
1158
1159
1160
1161
1162
1163
1164
1165
1166
1167
1168
1169
1170
1171
1172
1173
1174
1175
1176
1177
1178
1179
1180
1181
1182
1183
1184
1185
1186
1187
1188
1189
1190
1191
1192
1193
1194
1195
1196
1197
1198
1199
1200
1201
1202
1203
1204
1205
1206
1207
1208
1209
1210
1211
1212
1213
1214
1215
1216
1217
1218
1219
1220
1221
1222
1223
1224
1225
1226
1227
1228
1229
1230
1231
1232
1233
1234
1235
1236
1237
1238
1239
1240
1241
1242
1243
1244
1245
1246
1247
1248
1249
1250
1251
1252
1253
1254
1255
1256
1257
1258
1259
1260
1261
1262
1263
1264
1265
1266
1267
1268
1269
1270
1271
1272
1273
1274
1275
1276
1277
1278
1279
1280
1281
1282
1283
1284
1285
1286
1287
1288
1289
1290
1291
1292
1293
1294
1295
1296
1297
1298
1299
1300
1301
1302
1303
1304
1305
1306
1307
1308
1309
1310
1311
1312
1313
1314
1315
1316
1317
1318
1319
1320
1321
1322
1323
1324
1325
1326
1327
1328
1329
1330
1331
1332
1333
1334
1335
1336
1337
1338
1339
1340
1341
1342
1343
1344
1345
1346
1347
1348
1349
1350
1351
1352
1353
1354
1355
1356
1357
1358
1359
1360
1361
1362
1363
1364
1365
1366
1367
1368
1369
1370
1371
1372
1373
1374
1375
1376
1377
1378
1379
1380
1381
1382
1383
1384
1385
1386
1387
1388
1389
1390
1391
1392
1393
1394
1395
1396
1397
1398
1399
1400
1401
1402
1403
1404
1405
1406
1407
1408
1409
1410
1411
1412
1413
1414
1415
1416
1417
1418
1419
1420
1421
1422
1423
1424
1425
1426
1427
1428
1429
1430
1431
1432
1433
1434
1435
1436
1437
1438
1439
1440
1441
1442
1443
1444
1445
1446
1447
1448
1449
1450
1451
1452
1453
1454
1455
1456
1457
1458
1459
1460
1461
1462
1463
1464
1465
1466
1467
1468
1469
1470
1471
1472
1473
1474
1475
1476
1477
1478
1479
1480
1481
1482
1483
1484
1485
1486
1487
1488
1489
1490
1491
1492
1493
1494
1495
1496
1497
1498
1499
1500
1501
1502
1503
1504
1505
1506
1507
1508
1509
1510
1511
1512
1513
1514
1515
1516
1517
1518
1519
1520
1521
1522
1523
1524
1525
1526
1527
1528
1529
1530
1531
1532
1533
1534
1535
1536
1537
1538
1539
1540
1541
1542
1543
1544
1545
1546
1547
1548
1549
1550
1551
1552
1553
1554
1555
1556
1557
1558
1559
1560
1561
1562
1563
1564
1565
1566
1567
1568
1569
1570
1571
1572
1573
1574
1575
1576
1577
1578
1579
1580
1581
1582
1583
1584
1585
1586
1587
1588
1589
1590
1591
1592
1593
1594
1595
1596
1597
1598
1599
1600
1601
1602
1603
1604
1605
1606
1607
1608
1609
1610
1611
1612
1613
1614
1615
1616
1617
1618
1619
1620
1621
1622
1623
1624
1625
1626
1627
1628
1629
1630
1631
1632
1633
1634
1635
1636
1637
1638
1639
1640
1641
1642
1643
1644
1645
1646
1647
1648
1649
1650
1651
1652
1653
1654
1655
1656
1657
1658
1659
1660
1661
1662
1663
1664
1665
1666
1667
1668
1669
1670
1671
1672
1673
1674
1675
1676
1677
1678
1679
1680
1681
1682
1683
1684
1685
1686
1687
1688
1689
1690
1691
1692
1693
1694
1695
1696
1697
1698
1699
1700
1701
1702
1703
1704
1705
1706
1707
1708
1709
1710
1711
1712
1713
1714
1715
1716
1717
1718
1719
1720
1721
1722
1723
1724
1725
1726
1727
1728
1729
1730
1731
1732
1733
1734
1735
1736
1737
1738
1739
1740
1741
1742
1743
1744
1745
1746
1747
1748
1749
1750
1751
1752
1753
1754
1755
1756
1757
1758
1759
1750
1751
1752
1753
1754
1755
1756
1757
1758
1759
1760
1761
1762
1763
1764
1765
1766
1767
1768
1769
1770
1771
1772
1773
1774
1775
1776
1777
1778
1779
1770
1771
1772
1773
1774
1775
1776
1777
1778
1779
1780
1781
1782
1783
1784
1785
1786
1787
1788
1789
1780
1781
1782
1783
1784
1785
1786
1787
1788
1789
1790
1791
1792
1793
1794
1795
1796
1797
1798
1799
1790
1791
1792
1793
1794
1795
1796
1797
1798
1799
1800
1801
1802
1803
1804
1805
1806
1807
1808
1809
1800
1801
1802
1803
1804
1805
1806
1807
1808
1809
1810
1811
1812
1813
1814
1815
1816
1817
1818
1819
1810
1811
1812
1813
1814
1815
1816
1817
1818
1819
1820
1821
1822
1823
1824
1825
1826
1827
1828
1829
1820
1821
1822
1823
1824
1825
1826
1827
1828
1829
1830
1831
1832
1833
1834
1835
1836
1837
1838
1839
1830
1831
1832
1833
1834
1835
1836
1837
1838
1839
1840
1841
1842
1843
1844
1845
1846
1847
1848
1849
1840
1841
1842
1843
1844
1845
1846
1847
1848
1849
1850
1851
1852
1853
1854
1855
1856
1857
1858
1859
1850
1851
1852
1853
1854
1855
1856
1857
1858
1859
1860
1861
1862
1863
1864
1865
1866
1867
1868
1869
1860
1861
1862
1863
1864
1865
1866
1867
1868
1869
1870
1871
1872
1873
1874
1875
1876
1877
1878
1879
1880
1881
1882
1883
1884
1885
1886
1887
1888
1889
1880
1881
1882
1883
1884
1885
1886
1887
1888
1889
1890
1891
1892
1893
1894
1895
1896
1897
1898
1899
1890
1891
1892
1893
1894
1895
1896
1897
1898
1899
1900
1901
1902
1903
1904
1905
1906
1907
1908
1909
1900
1901
1902
1903
1904
1905
1906
1907
1908
1909
1910
1911
1912
1913
1914
1915
1916
1917
1918
1919
1910
1911
1912
1913
1914
1915
1916
1917
1918
1919
1920
1921
1922
1923
1924
1925
1926
1927
1928
1929
1920
1921
1922
1923
1924
1925
1926
1927
1928
1929
1930
1931
1932
1933
1934
1935
1936
1937
1938
1939
1930
1931
1932
1933
1934
1935
1936
1937
1938
1939
1940
1941
1942
1943
1944
1945
1946
1947
1948
1949
1940
1941
1942
1943
1944
1945
1946
1947
1948
1949
1950
1951
1952
1953
1954
1955
1956
1957
1958
1959
1960
1961
1962
1963
1964
1965
1966
1967
1968
1969
1970
1971
1972
1973
1974
1975
1976
1977
1978
1979
1980
1981
1982
1983
1984
1985
1986
1987
1988
1989
1980
1981
1982
1983
1984
1985
1986
1987
1988
1989
1990
1991
1992
1993
1994
1995
1996
1997
1998
1999
1990
1991
1992
1993
1994
1995
1996
1997
1998
1999
2000
2001
2002
2003
2004
2005
2006
2007
2008
2009
2000
2001
2002
2003
2004
2005
2006
2007
2008
2009
2010
2011
2012
2013
2014
2015
2016
2017
2018
2019
2020
2021
2022
2023
2024
2025
2026
2027
2028
2029
2030
2031
2032
2033
2034
2035
2036
2037
2038
2039
2040
2041
2042
2043
2044
2045
2046
2047
2048
2049
2050
2051
2052
2053
2054
2055
2056
2057
2058
2059
2060
2061
2062
2063
2064
2065
2066
2067
2068
2069
2070
2071
2072
2073
2074
2075
2076
2077
2078
2079
2080
2081
2082
2083
2084
2085
2086
2087
2088
2089
2080
2081
2082
2083
2084
2085
2086
2087
2088
2089
2090
2091
2092
2093
2094
2095
2096
2097
2098
2099
2090
2091
2092
2093
2094
2095
2096
2097
2098
2099
2100
2101
2102
2103
2104
2105
2106
2107
2108
2109
2100
2101
2102
2103
2104
2105
2106
2107
2108
2109
2110
2111
2112
2113
2114
2115
2116
2117
2118
2119
2110
2111
2112
2113
2114
2115
2116
2117
2118
2119
2120
2121
2122
2123
2124
2125
2126
2127
2128
2129
2120
2121
2122
2123
2124
2125
2126
2127
2128
2129
2130
2131
2132
2133
2134
2135
2136
2137
2138
2139
2130
2131
2132
2133
2134
2135
2136
2137
2138
2139
2140
2141
2142
2143
2144
2145
2146
2147
2148
2149
2140
2141
2142
2143
2144
2145
2146
2147
2148
2149
2150
21

730 Therefore, half of the differences between east and west distributions were used to be systematic
 731 uncertainty for $\bar{\eta}$ distributions.

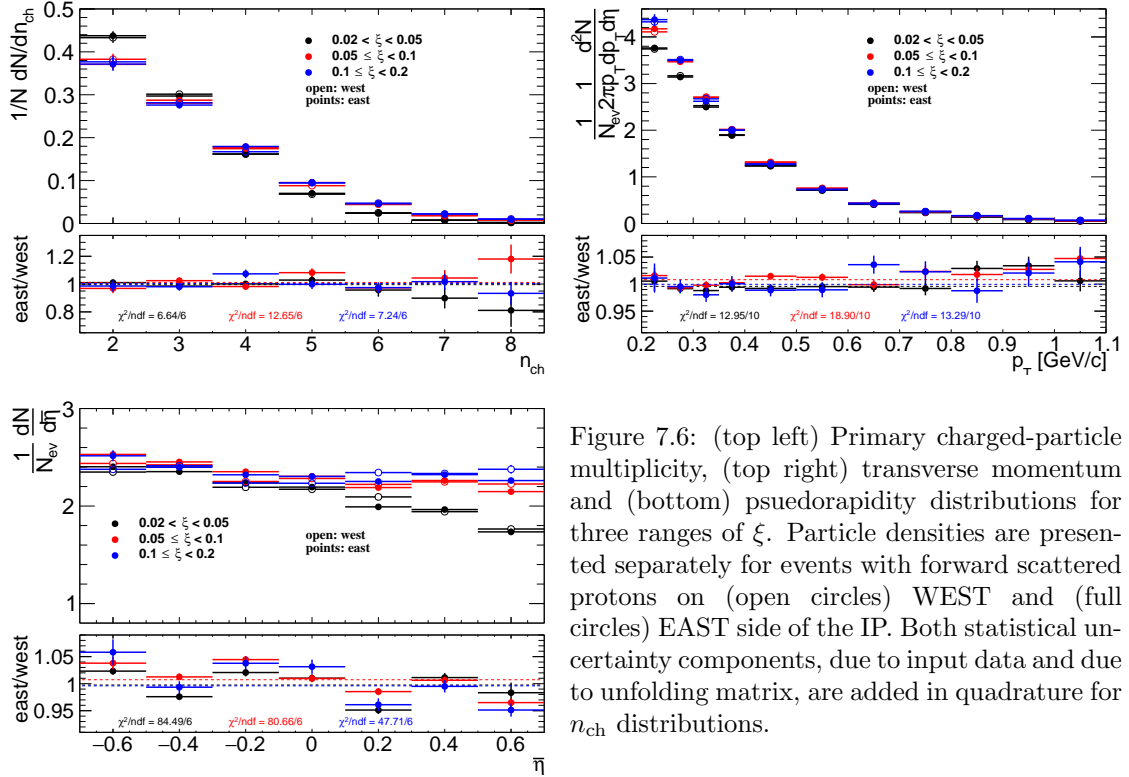


Figure 7.6: (top left) Primary charged-particle multiplicity, (top right) transverse momentum and (bottom) psuedorapidity distributions for three ranges of ξ . Particle densities are presented separately for events with forward scattered protons on (open circles) WEST and (full circles) EAST side of the IP. Both statistical uncertainty components, due to input data and due to unfolding matrix, are added in quadrature for n_{ch} distributions.

7.5 Particle Identification

732 Specific ionization energy loss, the dE/dx , is a function of the magnitude of a particle momentum.
 733 In this section the particle identification with help of dE/dx is described. Due to a low particle
 734 multiplicity and lack of signal in VPDs on the outgoing proton side (presence of the rapidity
 735 gap) in SD events, the time of collision is not defined precisely enough, therefore, the particle
 736 identification by the TOF is not possible and the analysis was limited to identification only by
 737 dE/dx .
 738

739 The ionization energy loss of charged particles in material is given by the Bethe-Bloch formula
 740 and for the STAR TPC by the more precise Bichsel formula [16]. The particle type can be
 741 determined by comparison of particle's dE/dx with the Bethe-Bloch (Bichsel) expectations. Figure
 742 7.7 shows the dE/dx versus rigidity $q \times p$ for particles in $|\eta| < 0.7$. Particles are well separated at
 743 low $|q \times p|$, whereas at higher $|q \times p|$ the dE/dx of different particle species starts to overlap: e^\pm
 744 and K^\pm merge at ~ 0.4 GeV/c, K^\pm and π^\pm merge at ~ 0.65 GeV/c, and $p(\bar{p})$ and π^\pm merge at
 745 ~ 1 GeV/c. Since the dE/dx distribution for a given particle type is not Gaussian, the following
 746 variable for each particle type was defined:

$$n\sigma_{dE/dx}^i = \ln \left(\frac{dE/dx}{(dE/dx)_i^{BB}} \right) / \sigma \quad (7.10)$$

747 where $(dE/dx)_i^{BB}$ is the Bethe-Bloch (Bichsel) expectation of dE/dx for the given particle type
 748 i ($i = \pi, K, p$), σ - the relative dE/dx resolution. The expected value of $n\sigma_{dE/dx}^i$ for the particle
 749 under consideration is 0 and the width equals to 1. The sample $n\sigma_{dE/dx}^i$ distribution for π^\pm, K^\pm
 750 and $p(\bar{p})$ in one ξ range, $0.02 < \xi < 0.05$, is shown in Fig. 7.8.

751 Figure 7.9 shows the $n\sigma_{dE/dx}^{\pi^\pm}$, $n\sigma_{dE/dx}^{K^\pm}$ and $n\sigma_{dE/dx}^{p(\bar{p})}$ distributions for $0.6 < p_T < 0.65$ GeV/c in
 752 the ξ range, $0.02 < \xi < 0.05$, each corrected for the energy loss (mass of i -particle was assumed) [1]
 753 and vertexing (other p_T bins are shown in Appendix B). To extract the particle yield for a given
 754 particle type, a multi-Gaussian fit is applied to the $n\sigma_{dE/dx}^i$ distribution in each p_T bin and ξ range.
 755 The parameters of the multi-Gaussian fit are the centroids μ_{i^-/i^+} , widths σ_{i^-/i^+} , sums and ratios of
 756 yields C_{i^-/i^+} , r_{i^-/i^+} for negative i^- and positive i^+ particles (π^\pm , e^\pm , K^\pm , p and \bar{p}). The positive
 757 and negative particle $n\sigma_{dE/dx}^i$ -distributions are fitted simultaneously, where the centroids and
 758 widths are kept the same for particle and antiparticle. In some p_T regions, the fit does not
 759 converge, because different particle species are not well separated there. Therefore, multiple steps
 760 of the fitting procedure are performed to reduce the number of free parameters in the final fit
 761 and ensure its stability. Almost all centroids and widths are constrained by a function with free
 762 parameters p_k , where $k \in \mathbb{N}$. The function is chosen to describe the data as best as possible.
 763 Since dE/dx is a function of the particle's momentum and its shape should be independent of
 764 the process under study, the values of p_k are obtained only for events with $0.02 < \xi < 0.05$ and
 765 kept the same for other ξ ranges. The electron contributions are fitted only in the first analysed p_T
 766 range, separately for each particle species and ξ range. For higher p_T ranges, they are estimated
 767 from PYTHIA 8 embedding MC, and scaled according to the ratio of PYTHIA 8 predictions and
 768 contributions fitted in the first p_T bin. The procedure slightly differs for different particle types.
 769 In each step, the multi-Gaussian fit is performed first, then the widths and centroids are fitted
 770 in p_T ranges in which the fit applied to $n\sigma_{dE/dx}^i$ converges. Later, the widths and centroids are
 771 extrapolated to other p_T ranges, in which particle species are not well separated:

772 1. π^\pm :

773 • Step 1 (Fig. 7.10):

- 774 – Analyze data with $0.2 < p_T < 0.65$ GeV/c
- 775 – Fit μ_{π^-/π^+} and σ_{π^-/π^+} as a function of p_T with a polynomial $p_0 p_T^3 + p_1 p_T^2 + p_2 p_T + p_3$
- 776 – Fit r_{e^-/e^+} as a function of p_T with a polynomial $p_0 p_T^2 + p_1 p_T + p_2$
- 777 – Fit C_{e^-/e^+} , μ_{K^-/K^+} as a functions of p_T with $p_0 \exp(p_1 p_T) + p_2$
- 778 – Fit μ_{e^-/e^+} as a function of p_T with $p_0 \exp[-(p_1 p_T)^{p_2}]$
- 779 – Fit σ_{K^-/K^+} as a function of p_T , for $0.3 < p_T < 0.5$ GeV/c, with constant p_0
- 780 – Fit $\mu_{\bar{p}/p}$ and $\sigma_{\bar{p}/p}$ as a function of p_T with $p_0 \exp(p_1 p_T)$

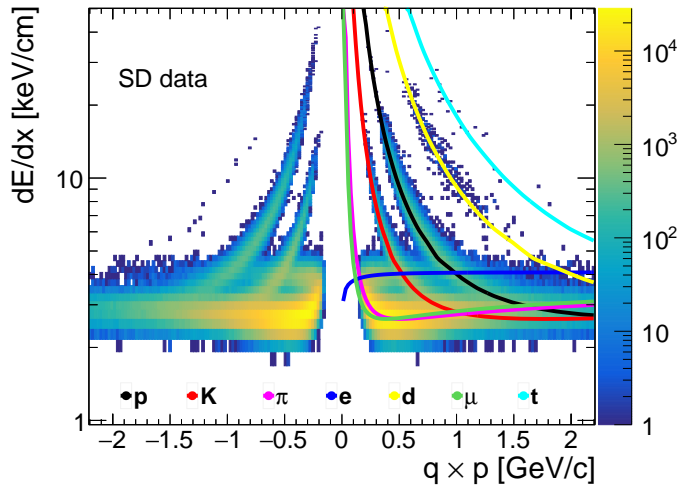


Figure 7.7: Specific ionization energy loss dE/dx as a function of rigidity $q \times p$ for particles in $|\eta| < 0.7$. The Bichsel predictions for each particle species are also shown.

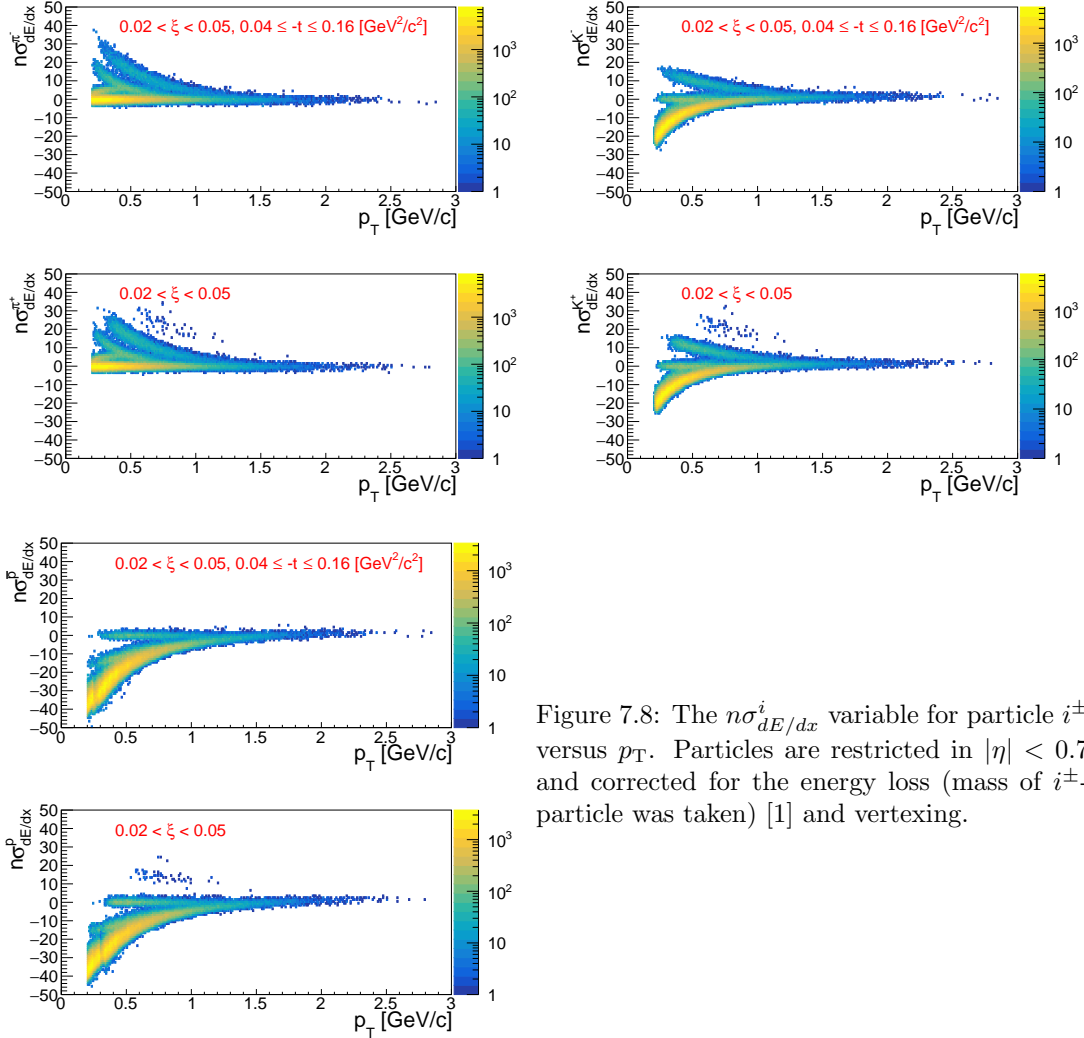


Figure 7.8: The $n\sigma_{dE/dx}^i$ variable for particle i^\pm versus p_T . Particles are restricted in $|\eta| < 0.7$ and corrected for the energy loss (mass of i^\pm -particle was taken) [1] and vertexing.

781

- Step 2:

782

- σ_{e^-/e^+} fixed to 1.2 and 0.8 for $0.2 < p_T < 0.4$ and $0.4 < p_T < 0.7$, respectively
- Fit σ_{K^-/K^+} as a function of p_T , for $0.3 < p_T < 0.7$ GeV/c, with constant p_0 and fix it to the value of p_0
- The rest parameters from Step 1 are fixed to the values calculated from functions obtained in Step 1: μ_{π^-/π^+} , σ_{π^-/π^+} , r_{e^-/e^+} , C_{e^-/e^+} , μ_{e^-/e^+} , μ_{K^-/K^+} , $\mu_{\bar{p}/p}$, $\sigma_{\bar{p}/p}$

783

784

785

786

787

788

2. K^\pm :

789

- Step 1 (Fig. 7.11):

790

791

792

793

794

795

- Analyze data with $0.2 < p_T < 0.6$ GeV/c
- Fit μ_{π^-/π^+} as a function of p_T with $-\exp(p_0 + p_1 p_T)$
- Fit σ_{π^-/π^+} , C_{e^-/e^+} , σ_{e^-/e^+} , σ_{K^-/K^+} as a function of p_T with $\exp(p_0 + p_1 p_T)$
- Fit r_{e^-/e^+} as a function of p_T with constant p_0
- Fit μ_{e^-/e^+} as a function of p_T with a polynomial $p_0 p_T^3 + p_1 p_T^2 + p_2 p_T + p_3$
- Fit μ_{K^-/K^+} as a function of p_T with a polynomial $p_0 + p_1 p_T^2$

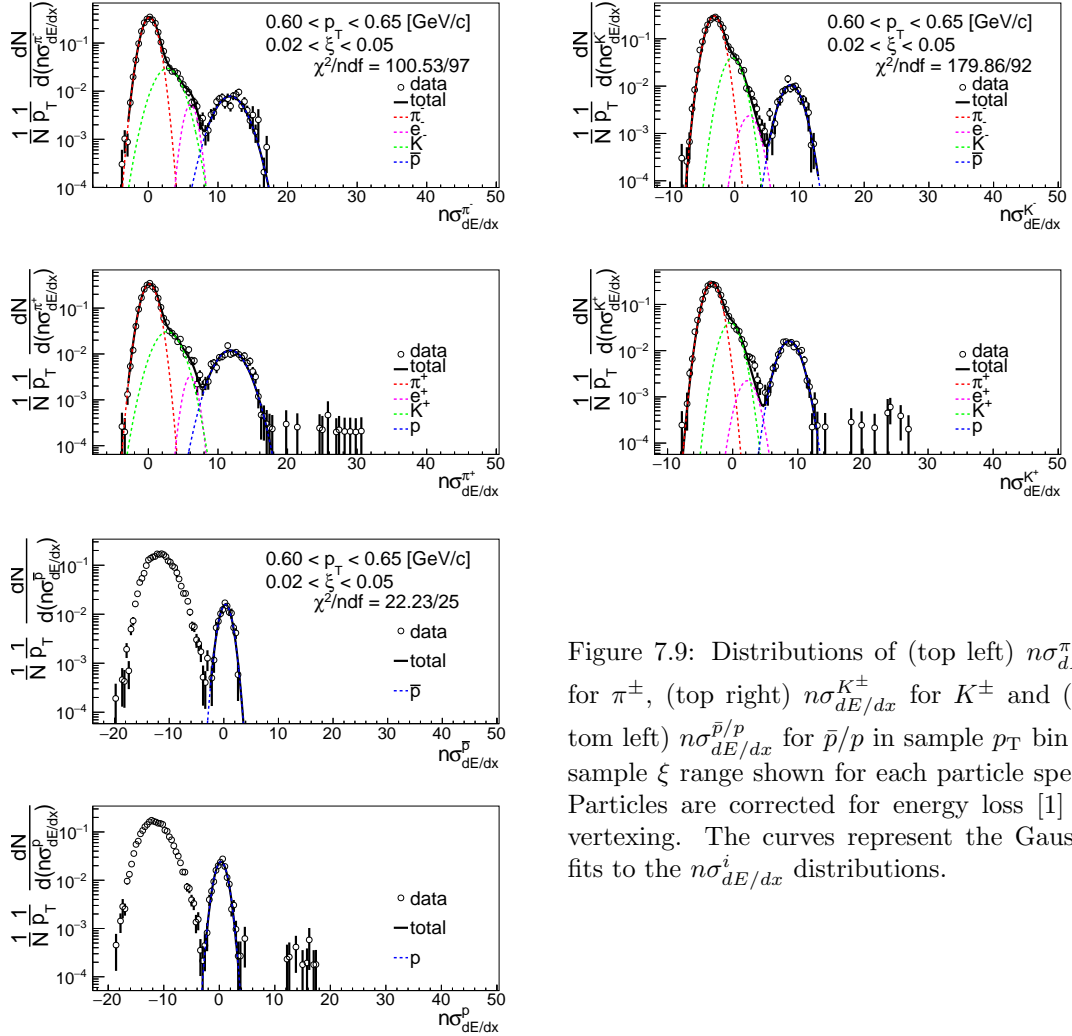


Figure 7.9: Distributions of (top left) $n\sigma_{dE/dx}^{\pi^\pm}$, (top right) $n\sigma_{dE/dx}^{K^\pm}$ and (bottom left) $n\sigma_{dE/dx}^{\bar{p}/p}$ for \bar{p}/p in sample p_T bin and sample ξ range shown for each particle species. Particles are corrected for energy loss [1] and vertexing. The curves represent the Gaussian fits to the $n\sigma_{dE/dx}^i$ distributions.

- Step 2:
 - All parameters from Step 1 except σ_{e^-/e^+} are fixed to the values calculated from functions obtained in Step 1
 - Fit σ_{e^-/e^+} as a function of p_T , for $0.45 < p_T < 0.65$ GeV/c, with constant p_0
- Step 3:
 - σ_{e^-/e^+} fixed to the values calculated from functions obtained in Steps 1 and 2 for $0.3 < p_T < 0.45$ and $0.45 < p_T < 0.65$, respectively.
 - The rest parameters from Step 1 are fixed to the values calculated from functions obtained in Step 1: μ_{π^-/π^+} , σ_{π^-/π^+} , r_{e^-/e^+} , C_{e^-/e^+} , μ_{e^-/e^+} , μ_{K^-/K^+} , σ_{K^-/K^+}

3. \bar{p}, p :

- Step 1 (Fig. 7.12):
 - Analyze data with $0.4 < p_T < 0.9$ GeV/c
 - Fit μ_{π^-/π^+} , μ_{K^-/K^+} as a function of p_T with a polynomial $p_0 p_T + p_1$
 - Fit σ_{π^-/π^+} as a function of p_T with a polynomial $p_0 p_T^2 + p_1 p_T + p_2$

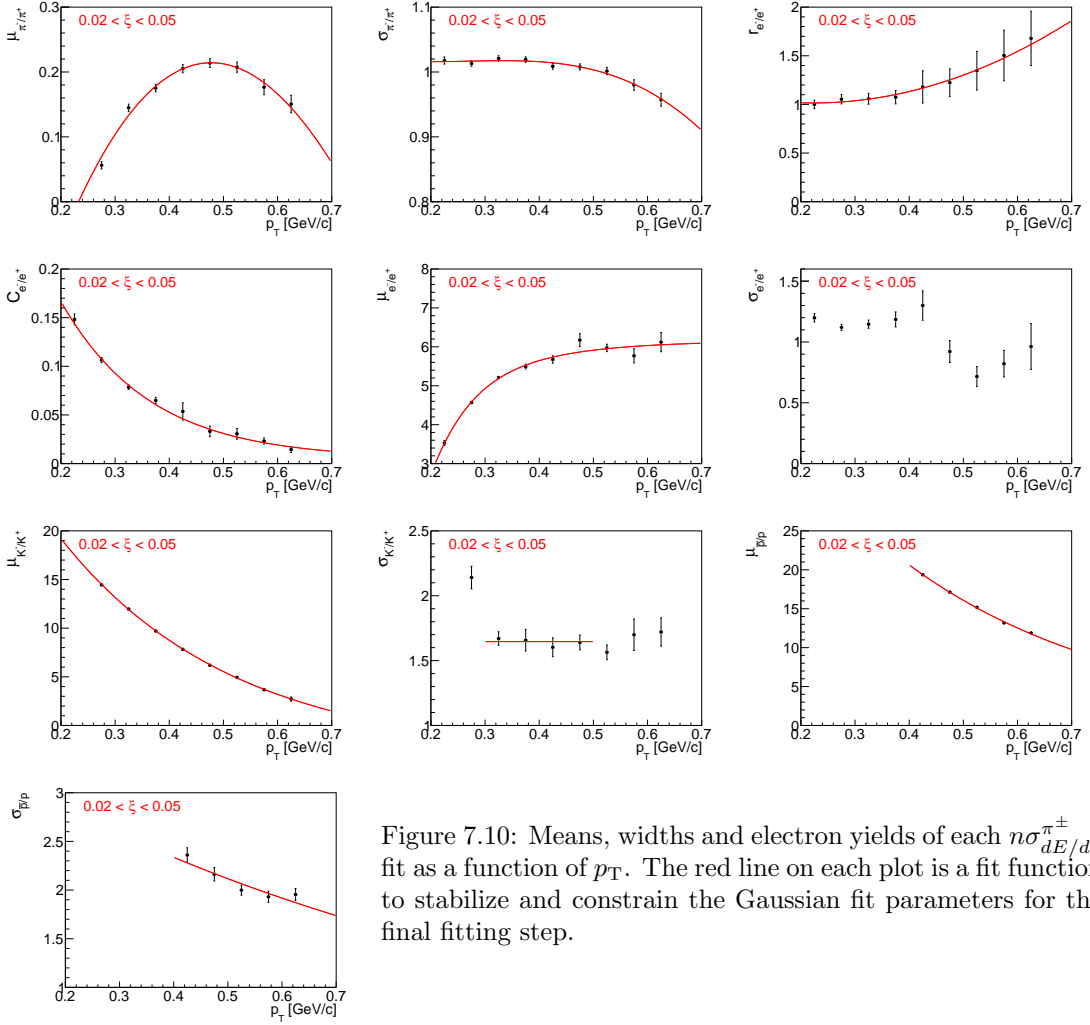


Figure 7.10: Means, widths and electron yields of each $n\sigma_{dE/dx}^{\pi^\pm}$ fit as a function of p_T . The red line on each plot is a fit function to stabilize and constrain the Gaussian fit parameters for the final fitting step.

- 810 – Fit σ_{K^-/K^+} as a function of p_T with $\exp(p_0 + p_1 p_T)$
- 811 • Step 2:
 - 812 – μ_{K^-/K^+} fixed to the values calculated from a function obtained in Step 1
 - 813 – All the rest parameters from Step 1 are limited to the values calculated from functions obtained in Step 1
 - 814 – Fit μ_{π^-/π^+} , σ_{π^-/π^+} , σ_{K^-/K^+} as a function of p_T with a polynomial $p_0 p_T^2 + p_1 p_T + p_2$
 - 815 – Fit $\mu_{\bar{p}/p}$ as a function of p_T , for $0.7 < p_T < 1.0$ GeV/c, with constant p_0
- 816 • Step 3:
 - 817 – μ_{K^-/K^+} fixed to the values calculated from a function obtained in Step 1
 - 818 – $\mu_{\bar{p}/p}$ fixed to the values calculated from a function obtained in Step 2 for $0.7 < p_T < 1.0$
 - 819 – The rest parameters from Step 2 are fixed to the values calculated from functions obtained in Step 2: μ_{π^-/π^+} , σ_{π^-/π^+} , σ_{K^-/K^+}

823 The particle yield is extracted from the fit to the corresponding $n\sigma_{dE/dx}^i$ distribution (corrected
 824 only for the energy loss and vertexing). As shown in Fig. 7.8, the dE/dx of each particle type merge
 825 at large p_T . Hence, the particle identification is limited. Pions can be identified in the momentum
 826 range of 0.2 – 0.7 GeV/c, kaons in 0.3 – 0.65 GeV/c and (anti)protons in 0.4 – 1.0 GeV/c.

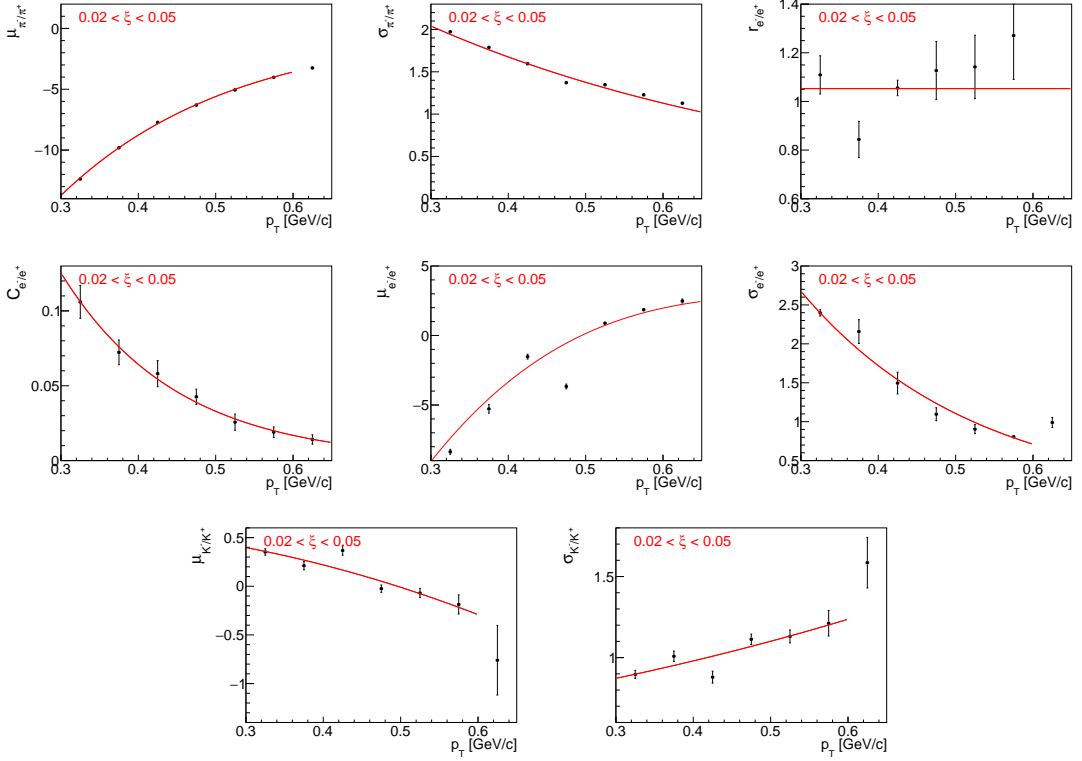


Figure 7.11: Means, widths and electron yields of each $n\sigma_{dE/dx}^{K^\pm}$ fit as a function of p_T . The red line on each plot is a fit function to stabilize and constrain the Gaussian fit parameters for the final fitting step.

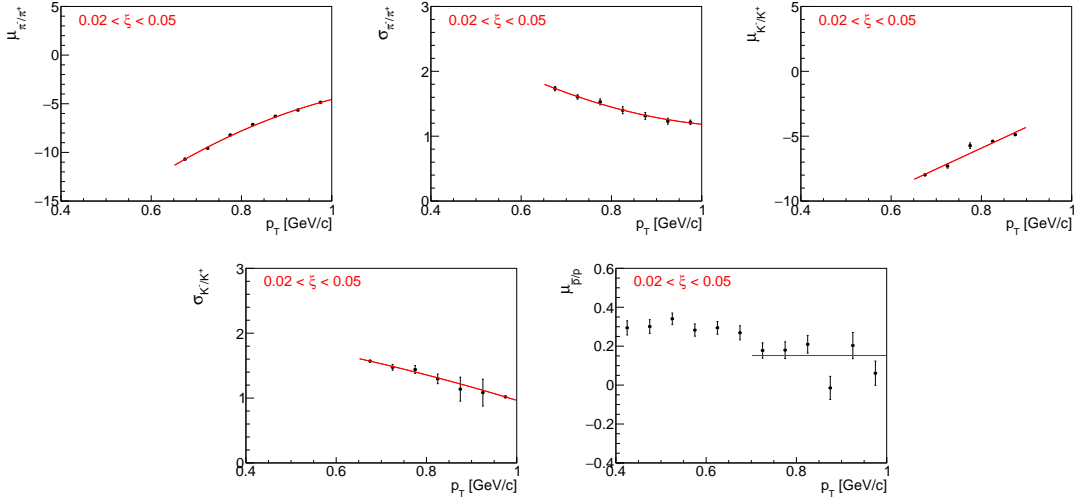


Figure 7.12: Means and widths of each $n\sigma_{dE/dx}^{\bar{p}/p}$ fit as a function of p_T . The red line on each plot is a fit function to stabilize and constrain the Gaussian fit parameters for the final fitting step.

827 7.6 Antiparticle-to-Particle Ratios

828 The following steps were taken to correct the identified antiparticle to particle (pion, kaon, proton
 829 and their antiparticle) multiplicity ratios as a function of p_T in three ranges of ξ :

- 830 • The raw identified particle yields were obtained through multi-Gaussian fits to the $n\sigma_{dE/dx}^i$
 831 distributions (Sec. 7.5), where the vertex reconstruction and energy loss corrections [1] were
 832 applied. The latter depends on the particle type.
- 833 • The non-SD background (Sec. 4.2) is the same for particles and antiparticles, thus, it was
 834 not subtracted. The accidental background contribution (Sec. 4) is very small, hence, any
 835 particle-antiparticle differences have a negligible effect on the result. Therefore, it was as-
 836 sumed that the accidental background does not depend on the particle type and for this
 837 reason it was not subtracted.
- 838 • The particle yields were corrected for track reconstruction efficiencies [1], which depend on
 839 the particle type and charge. These corrections are averaged over η and V_z . The ratio of
 840 particle to antiparticle TPC-TOF efficiencies is shown in Fig. 7.13. It weakly depends on ξ
 841 range, therefore, only sample results for single range of $0.02 < \xi < 0.05$ are presented.
- 842 • The background from non-primary tracks was subtracted (Sec. 4.1):
 - 843 – π^\pm : weak decays pions, muon contribution and background from detector dead-material
 interactions,
 - 844 – p : background from detector dead-material interactions,
 - 845 – p, \bar{p} : reconstructed tracks which have the appropriate number of common hit points
 with true-level particle, but the distance between them is too large (this background is
 negligibly small for other particle types),
 - 846 – fake track contribution was assumed to be the same for each particle type, hence, it
 was not subtracted.
- 847 • Since track and ξ migrations, and BBC-small efficiency, do not depend on the particle type
 848 and charge, these corrections are not applied.
- 849 • Finally, each antiparticle p_T distribution was divided by the corresponding particle p_T dis-
 850 tribution to obtain fully corrected identified antiparticle to particle multiplicity ratios.
- 851 • Additionally, the average antiparticle to particle ratios over fiducial region of p_T in each ξ
 852 region were calculated.

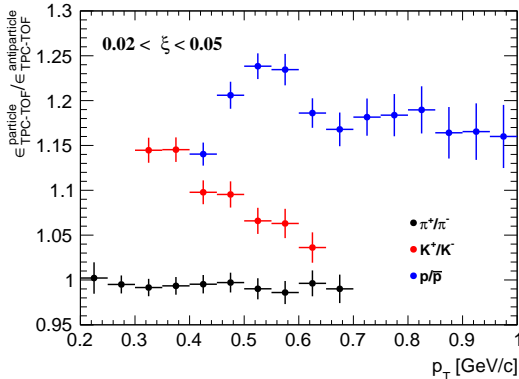


Figure 7.13: Ratio of particle to antiparticle TPC-TOF efficiencies for $0.02 < \xi < 0.05$.

8. Systematic Uncertainties

Apart from the statistical uncertainties there are also systematic uncertainties originating from inefficiencies and limitations of the measurement devices and techniques. The following sources of systematic uncertainties were considered:

- the effect of off-time pile-up on TPC track reconstruction efficiency [1],
- the uncertainty of TPC track reconstruction efficiency related to the description of dead-material in simulation [1],
- representation of data sample in embedding MC [1],
- variation in the track quality cuts [1],
- non-primary track background contribution (Sec. 4.1),
- fake track background contribution (Sec. 4.1),
- TOF system simulation accuracy [1],
- accidental background contribution (Sec. 4),
- the effect of alternative model of hadronization on BBC-small efficiency (Sec. 5.2),
- non-SD background contribution (Sec. 4.2),
- the effect of alternative model on ϵ_m correction (Sec. 7.1),
- non-closure (Sec 7.3),
- non-closure of N_{ev} , applied only to p_T and $\bar{\eta}$ distributions,
- difference in the distributions calculated separately for events in which forward proton is on one and the other side of the IP (east-west, Sec 7.4).

Some of the systematic uncertainties on $1/N dN/dn_{\text{ch}}$ (related to TPC and TOF reconstruction efficiencies, fake track background contribution) are propagated by randomly removing and adding tracks in the n_{sel} distribution before unfolding procedure. For each track, a random number is generated. If this number is smaller than the absolute value of systematic uncertainty, then n_{sel} is increased or decreased, depending on the sign of systematic uncertainty.

Figures 8.1 to 8.3 show the components contributing to the total systematic uncertainty for charged particle distributions without the identification. The dominant systematic uncertainty for p_T and n_{ch} distributions is related to TOF system simulation accuracy. It affects mainly low- p_T particles, where it is about 2 – 3%, and large charged particle multiplicities, where it varies up to 20% for $n_{\text{ch}} = 8$ and $0.02 < \xi < 0.05$. In case of $\bar{\eta}$ distribution, the systematic uncertainty on TOF mainly refers to charged particles produced at the edge of the fiducial region, for which it is about 2%. The largest (up to 30%) systematic uncertainty for $\langle \bar{\eta} \rangle$, is related to the observed difference in the distributions calculated separately with respect to the forward-scattered proton direction. The rest of the components have smaller contributions to the total systematic uncertainty. The systematic uncertainty on non-closure is on average at the level of 2% which proves the accuracy of the correction procedure.

Figures 8.4 to 8.7 show breakdown of all different systematics for the antiparticle-to-particle multiplicity ratio distributions. An additional systematic contribution for \bar{p}/p multiplicity ratio due to proton background estimation was introduced. Since most of the corrections are the same for particle and its antiparticle, nearly all systematic uncertainties cancel out in the antiparticle-to-particle ratios. The largest sources of systematics, which do not, are related to proton background estimation and dead-material effect on TPC track reconstruction efficiency. The former was found to be up to 6%, whereas the latter varies up to 2% for low- p_T \bar{p}/p multiplicity ratio.

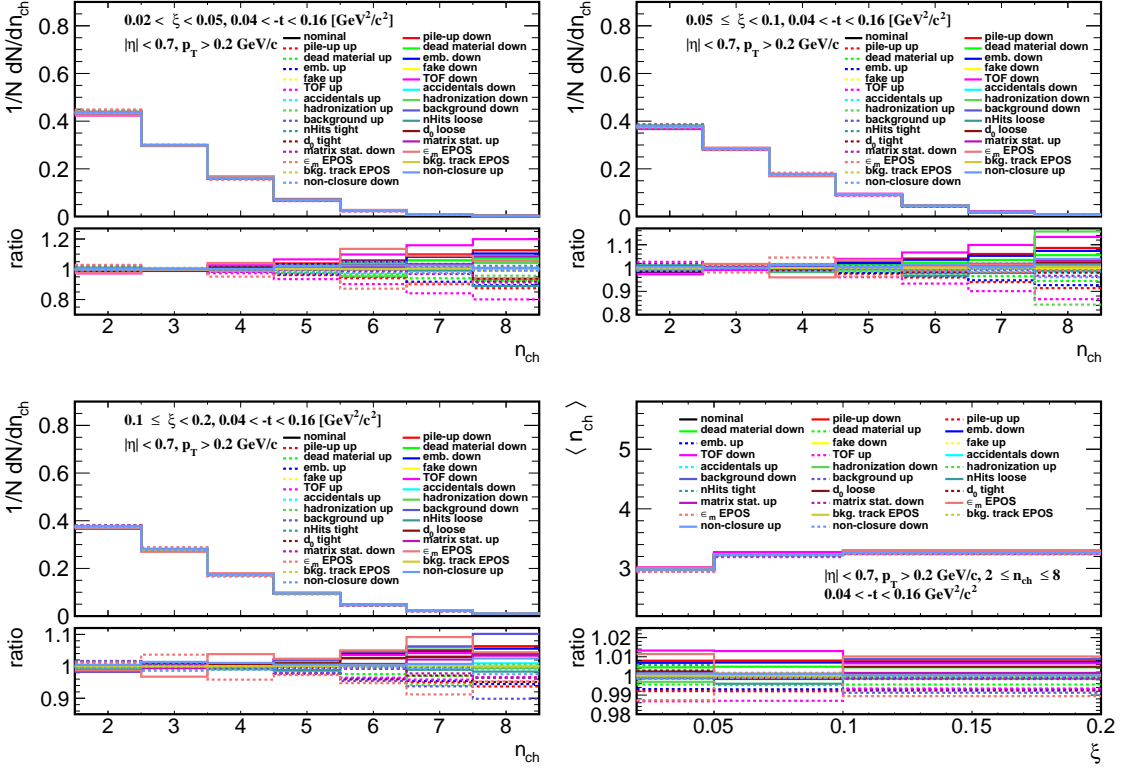


Figure 8.1: Components of the systematic uncertainties for the charged particle multiplicity in three ξ regions and for the average charged particle multiplicity.

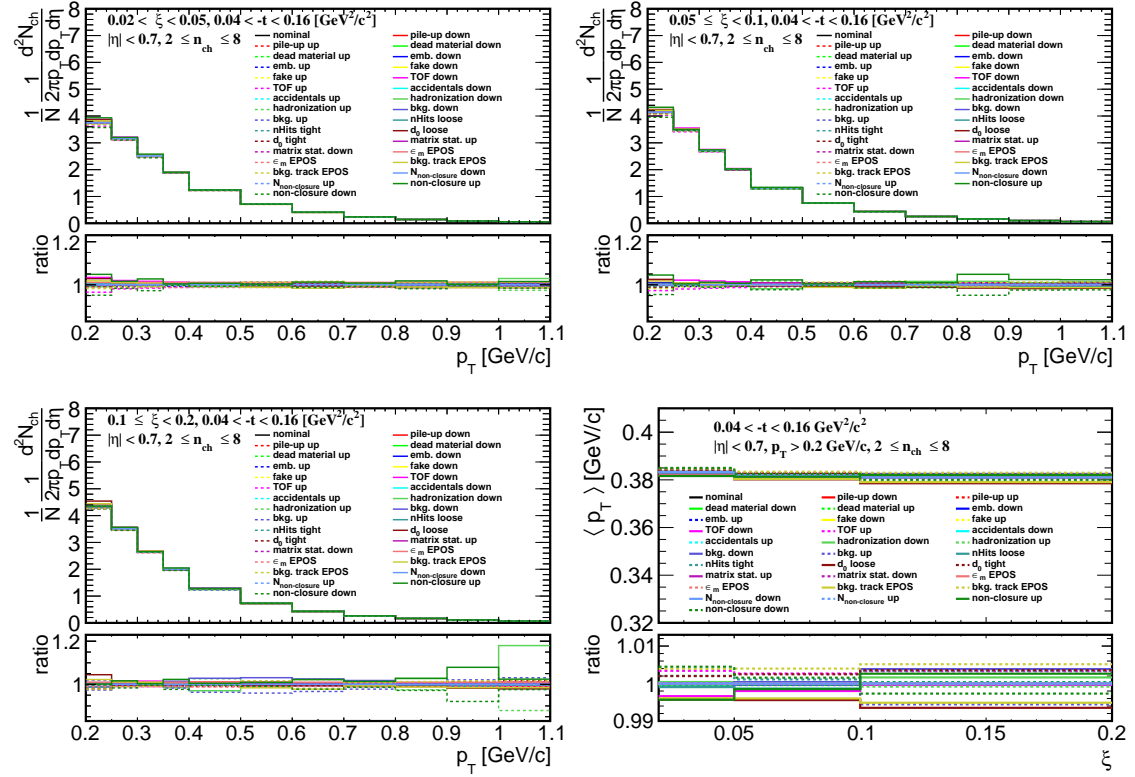


Figure 8.2: Components of the systematic uncertainties for p_T distributions in three ξ regions and for an average p_T distribution.

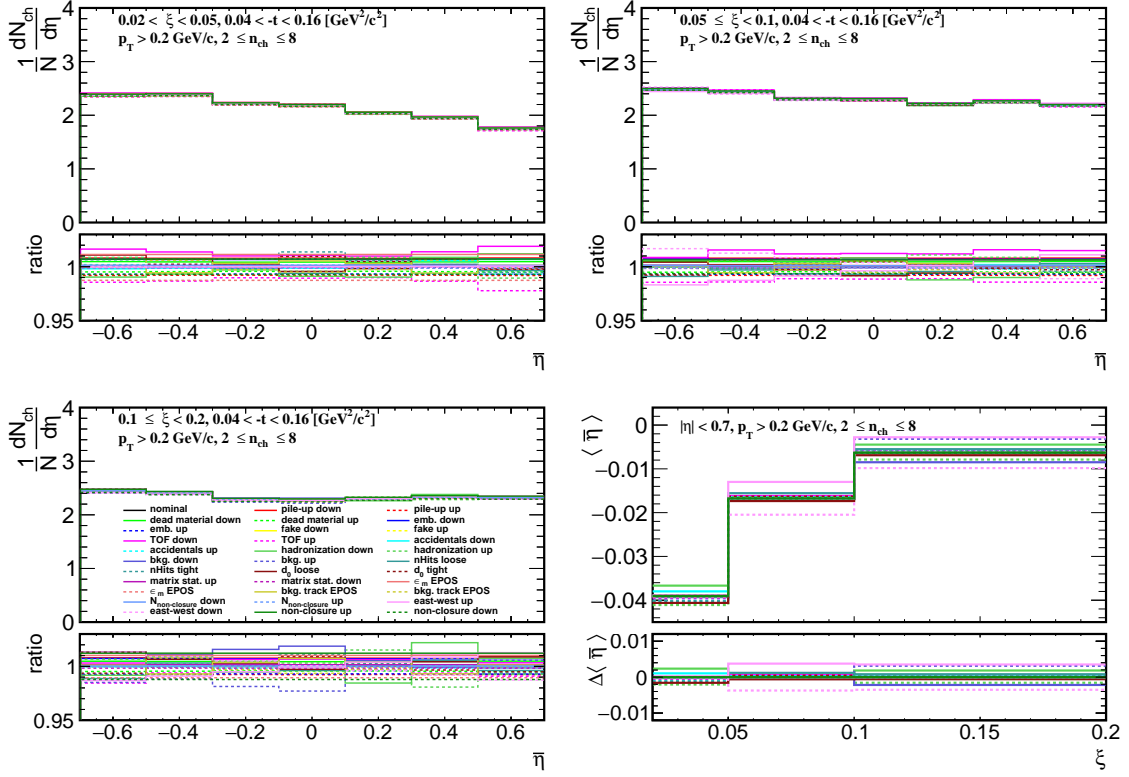


Figure 8.3: Components of the systematic uncertainties for $\bar{\eta}$ distributions in three ξ regions and for an average $\bar{\eta}$ distribution.

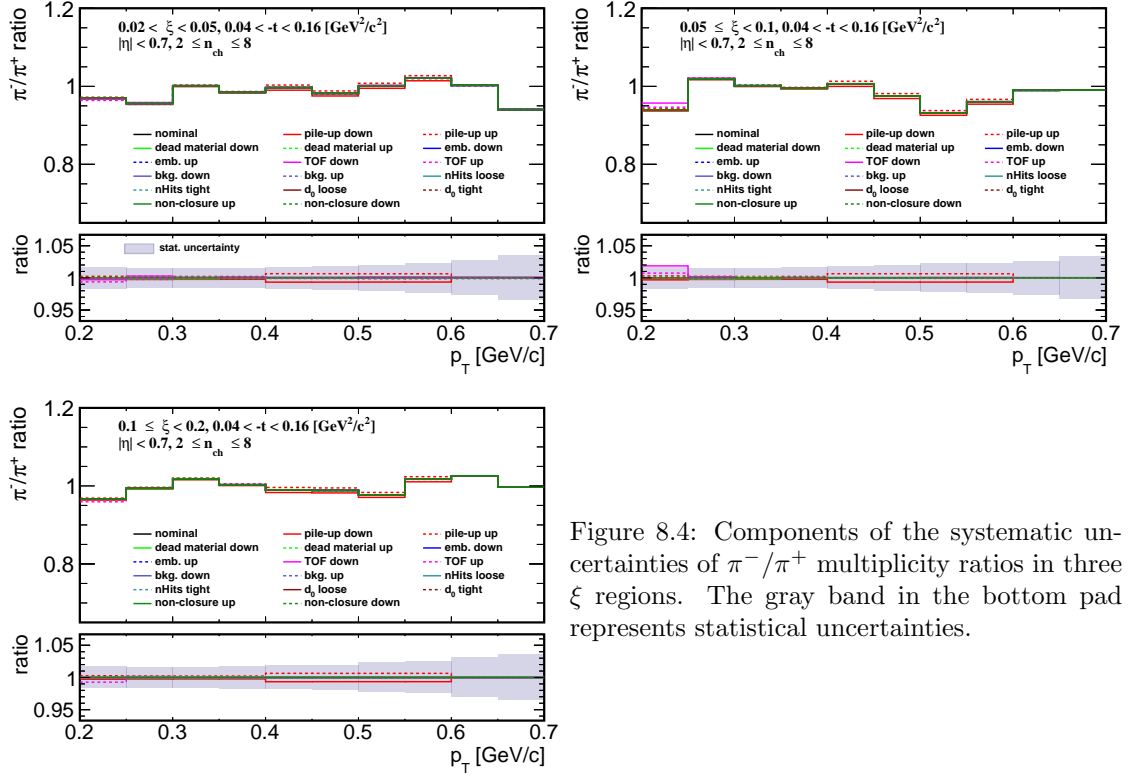


Figure 8.4: Components of the systematic uncertainties of π^-/π^+ multiplicity ratios in three ξ regions. The gray band in the bottom pad represents statistical uncertainties.

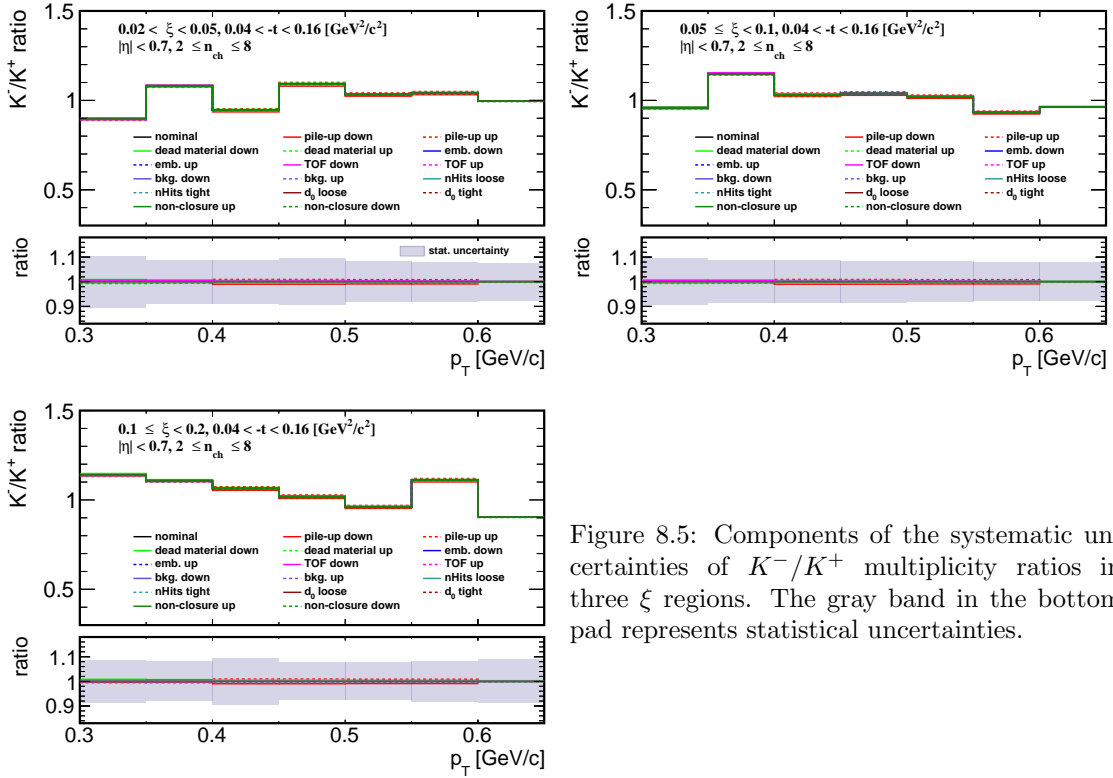


Figure 8.5: Components of the systematic uncertainties of K^-/K^+ multiplicity ratios in three ξ regions. The gray band in the bottom pad represents statistical uncertainties.

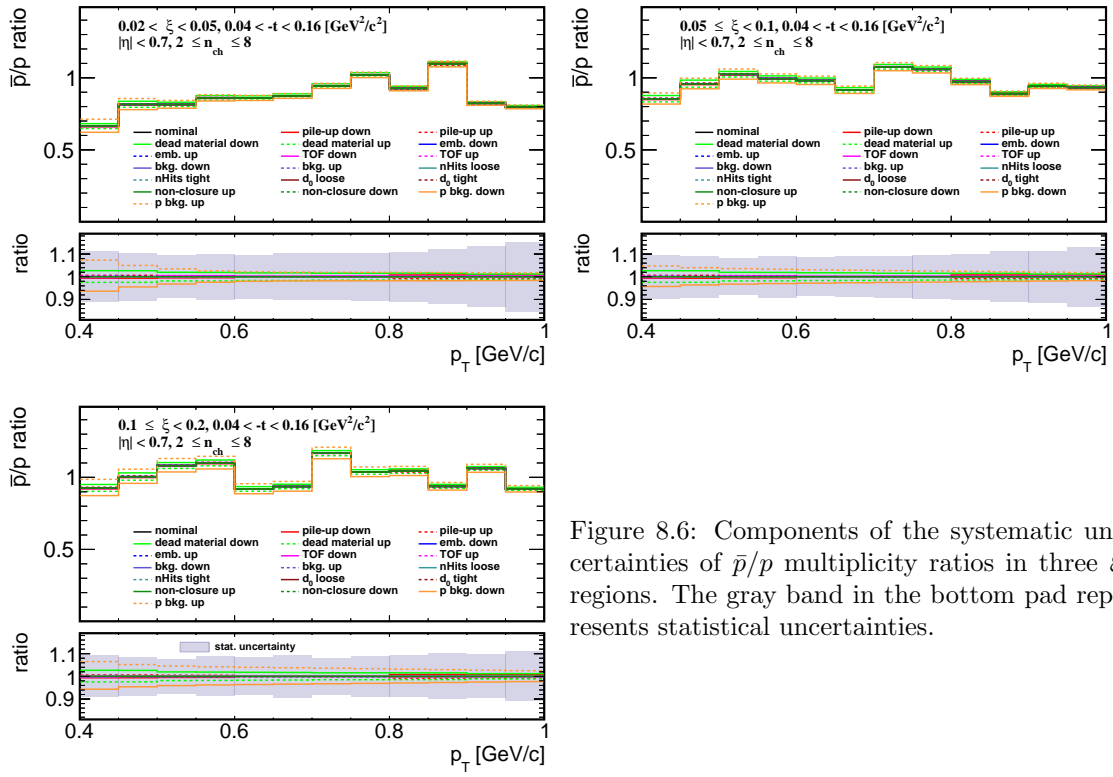


Figure 8.6: Components of the systematic uncertainties of \bar{p}/p multiplicity ratios in three ξ regions. The gray band in the bottom pad represents statistical uncertainties.

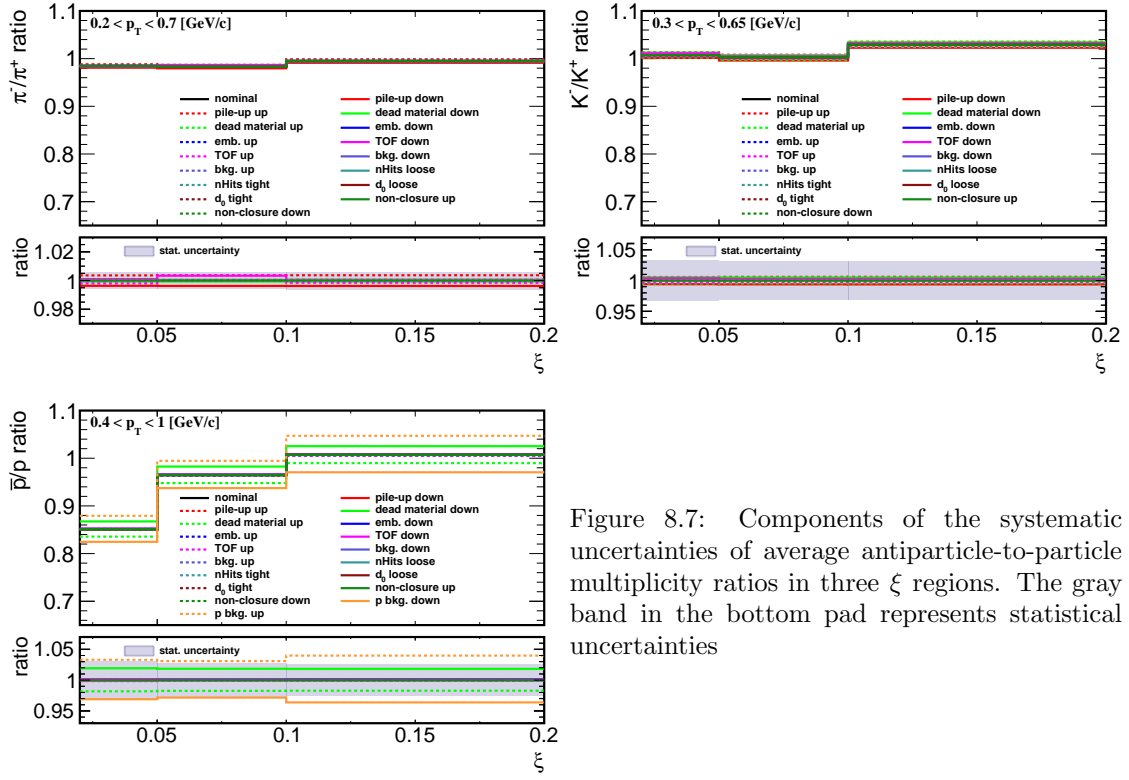


Figure 8.7: Components of the systematic uncertainties of average antiparticle-to-particle multiplicity ratios in three ξ regions. The gray band in the bottom pad represents statistical uncertainties

9. Results

In the following section, the final-state charged particle distributions are compared with various SD MC predictions, i.e.

- PYTHIA 8 4C (SaS),
- PYTHIA 8 A2 (MBR),
- PYTHIA 8 A2 (MBR-tuned),
- HERWIG 7,
- EPOS LHC with combined two classes of processes: diffractive (EPOS SD) and non-diffractive (EPOS SD'),
- EPOS LHC SD'.

In all figures, data are shown as solid points with error bars representing the statistical uncertainties. Gray boxes represent statistical and systematic uncertainties added in quadrature. Predictions from MC models are shown as colour histograms and markers. The lower panel in each figure shows the ratio of data to the models' predictions. All results are presented separately for three ranges of ξ : $0.02 < \xi < 0.05$, $0.05 < \xi < 0.1$, $0.1 < \xi < 0.2$.

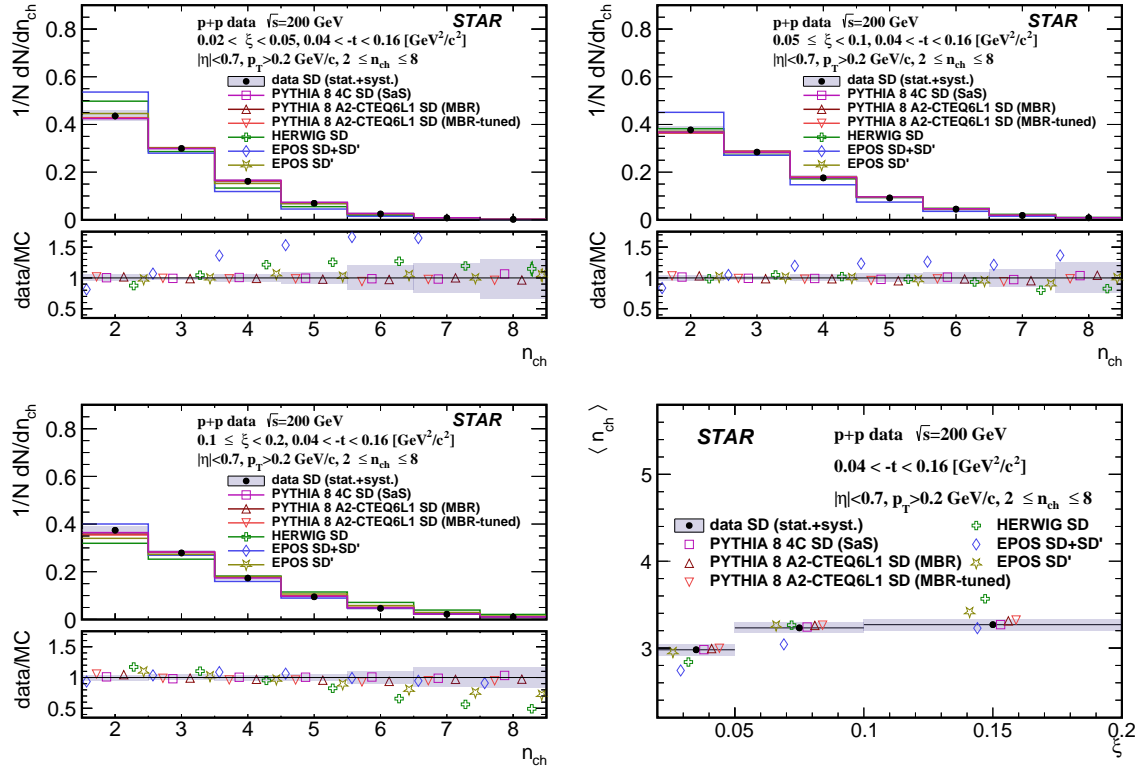


Figure 9.1: Primary charged-particle multiplicity shown separately for the three ranges of ξ : (top left) $0.02 < \xi < 0.05$, (top right) $0.05 < \xi < 0.1$, (bottom left) $0.1 < \xi < 0.2$ and (bottom right) the mean multiplicity $\langle n_{ch} \rangle$ as a function of ξ .

915 Figure 9.1 shows primary charged-particle multiplicity separately for the three ranges of ξ and
 916 the mean multiplicity $\langle n_{\text{ch}} \rangle$ as a function of ξ . Data follow the expected increase of $\langle n_{\text{ch}} \rangle$ with
 917 ξ due to the larger diffractive masses probed by increasing ξ in SD process. The shapes of the
 918 measured distributions are reproduced reasonably well by all models except EPOS SD+SD' and
 919 HERWIG SD which predicts smaller $\langle n_{\text{ch}} \rangle$ for $0.02 < \xi < 0.1$ and $0.02 < \xi < 0.05$, respectively.
 920 HERWIG SD predicts too large $\langle n_{\text{ch}} \rangle$ for $0.1 < \xi < 0.2$.

921 Figure 9.2 shows primary charged-particle multiplicities as a function of p_T separately for
 922 the three ranges of ξ and the mean transverse momentum $\langle p_T \rangle$ as a function of ξ . Data show
 923 that $\langle p_T \rangle$ depends very weakly on ξ . Models describe data fairly well except HERWIG SD which
 924 predicts much steeper dependence of particle density with p_T in all three ξ ranges.

925 Figure 9.3 shows primary charged-particle multiplicity as a function of $\bar{\eta}$ separately for the three
 926 ranges of ξ and the mean pseudorapidity $\langle \bar{\eta} \rangle$ as a function of ξ . Data show expected flattening of
 927 the $\bar{\eta}$ distribution with increasing ξ which reflects SD event-asymmetry and fact that the gap-edge
 928 at large ξ is outside $|\bar{\eta}| < 0.7$ region leading to more flat distribution of particle density as a
 929 function of $\bar{\eta}$. PYTHIA 8 models describe data fairly well only at $0.02 < \xi < 0.05$ and predicts
 930 flatter distributions for $0.05 < \xi < 0.2$. EPOS SD+SD' and HERWIG SD predict less and more
 931 steep dependence of particle density with $\bar{\eta}$ for all three ξ ranges, respectively.

932 Figure 9.4 shows the ratio of production yields of π^-/π^+ as a function of p_T separately for
 933 the three ranges of ξ . Data in all three ξ ranges are consistent with equal amounts of π^+ and
 934 π^- with no significant p_T dependence. Models agree with data (except HERWIG) predicting on
 935 average small deviation from unity by $\sim 2\%$ what is smaller than data uncertainties. HERWIG
 936 in first two ξ ranges predicts too large asymmetry between π^+ and π^- .

937 Figure 9.5 shows the ratio of production yields of K^-/K^+ as a function of p_T separately for

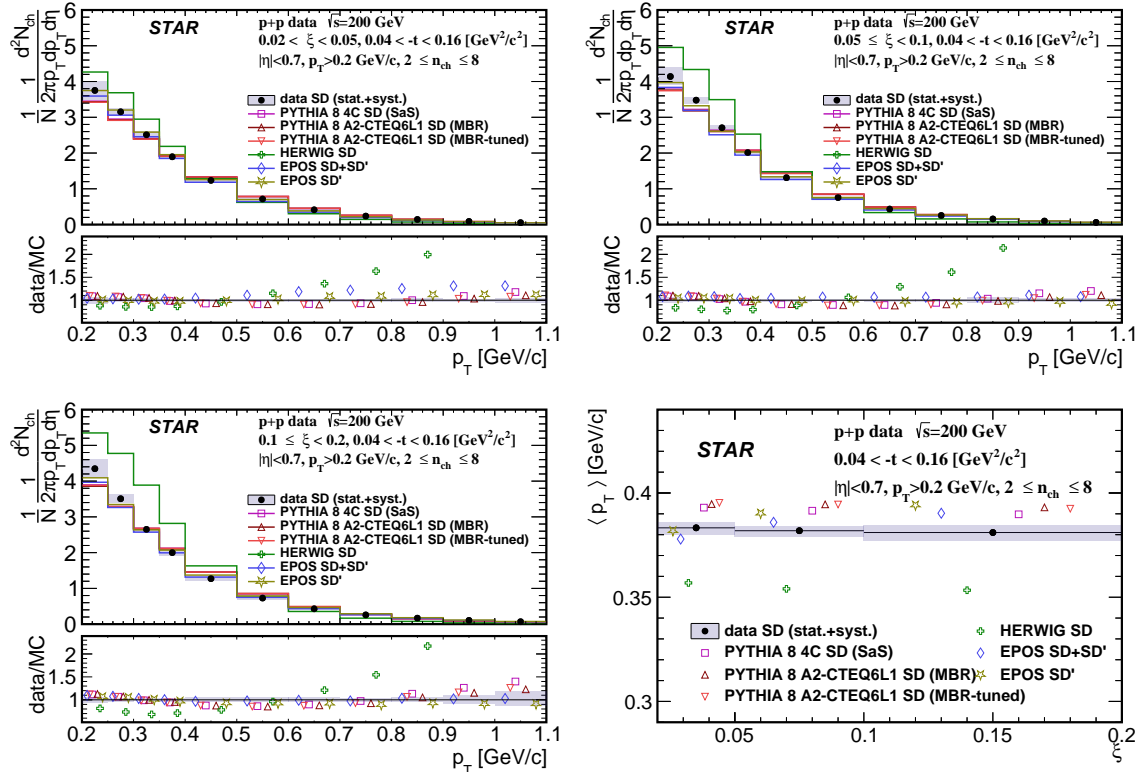


Figure 9.2: Primary charged-particle multiplicities as a function of p_T shown separately for the three ranges of ξ : (top left) $0.02 < \xi < 0.05$, (top right) $0.05 < \xi < 0.1$, (bottom left) $0.1 < \xi < 0.2$ and (bottom right) the mean transverse momentum $\langle p_T \rangle$ as a function of ξ .

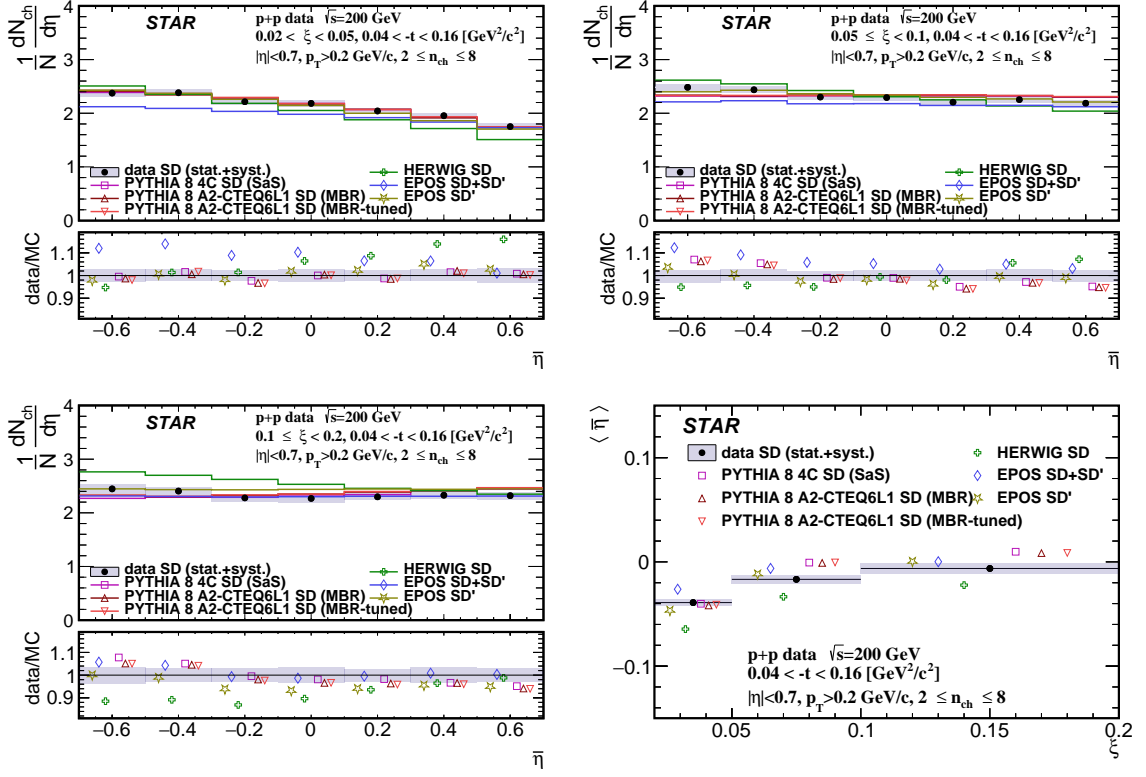


Figure 9.3: Primary charged-particle multiplicity as a function of $\bar{\eta}$ shown separately for the three ranges of ξ : (top left) $0.02 < \xi < 0.05$, (top right) $0.05 < \xi < 0.1$, (bottom left) $0.1 < \xi < 0.2$ and (bottom right) the mean pseudorapidity $\langle \bar{\eta} \rangle$ as a function of ξ .

938 the three ranges of ξ . Data in all three ξ ranges are consistent with equal amounts of K^+ and K^-
939 with no p_T dependence. Models agree with data except HERWIG in the first ξ range predicting
940 too large ratio of K^- to K^+ .

941 Figure 9.6 shows the ratio of production yields of \bar{p}/p as a function of p_T separately for the three
942 ranges of ξ . Data in the last two ξ ranges are consistent with equal amounts of p and \bar{p} with no p_T
943 dependence. However, in the first ξ range at $p_T < 0.7$ GeV/c data shows significant deviation from
944 PYTHIA8, EPOS SD' and EPOS SD+SD' agree with data in the last two ξ ranges. In first ξ
945 range PYTHIA8 and EPOS SD' predict small deviation from unity by $\approx 7\%$ which is smaller than
946 observed in data ($\bar{p}/p = 0.85 \pm 0.04$), whereas EPOS SD+SD' predicts an asymmetry between \bar{p}
947 and p of $\sim 30\%$ which is larger than observed in data except $p_T < 0.5$ GeV/c. HERWIG predicts
948 much larger baryon number transfer compared to data in first two ξ ranges and shows consistency
949 with data in last ξ range.

950 Figure 9.7 shows mean ratio of production yields of π^-/π^+ , K^-/K^+ and \bar{p}/p as a function of
951 ξ .

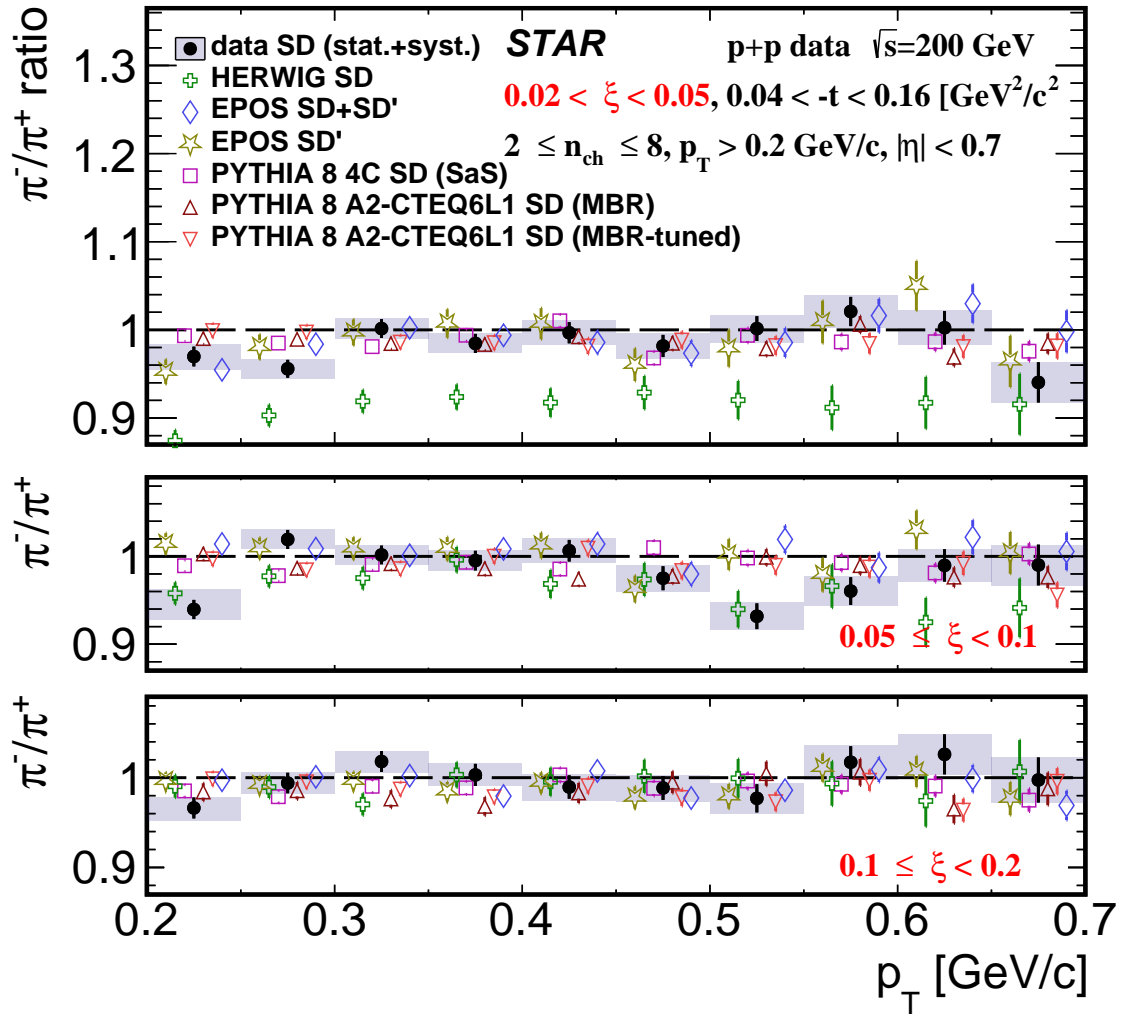


Figure 9.4: Ratio of production yields of π^-/π^+ as a function of p_{T} shown separately for the three ranges of ξ : (top) $0.02 < \xi < 0.05$, (middle) $0.05 < \xi < 0.1$, (bottom) $0.1 < \xi < 0.2$.

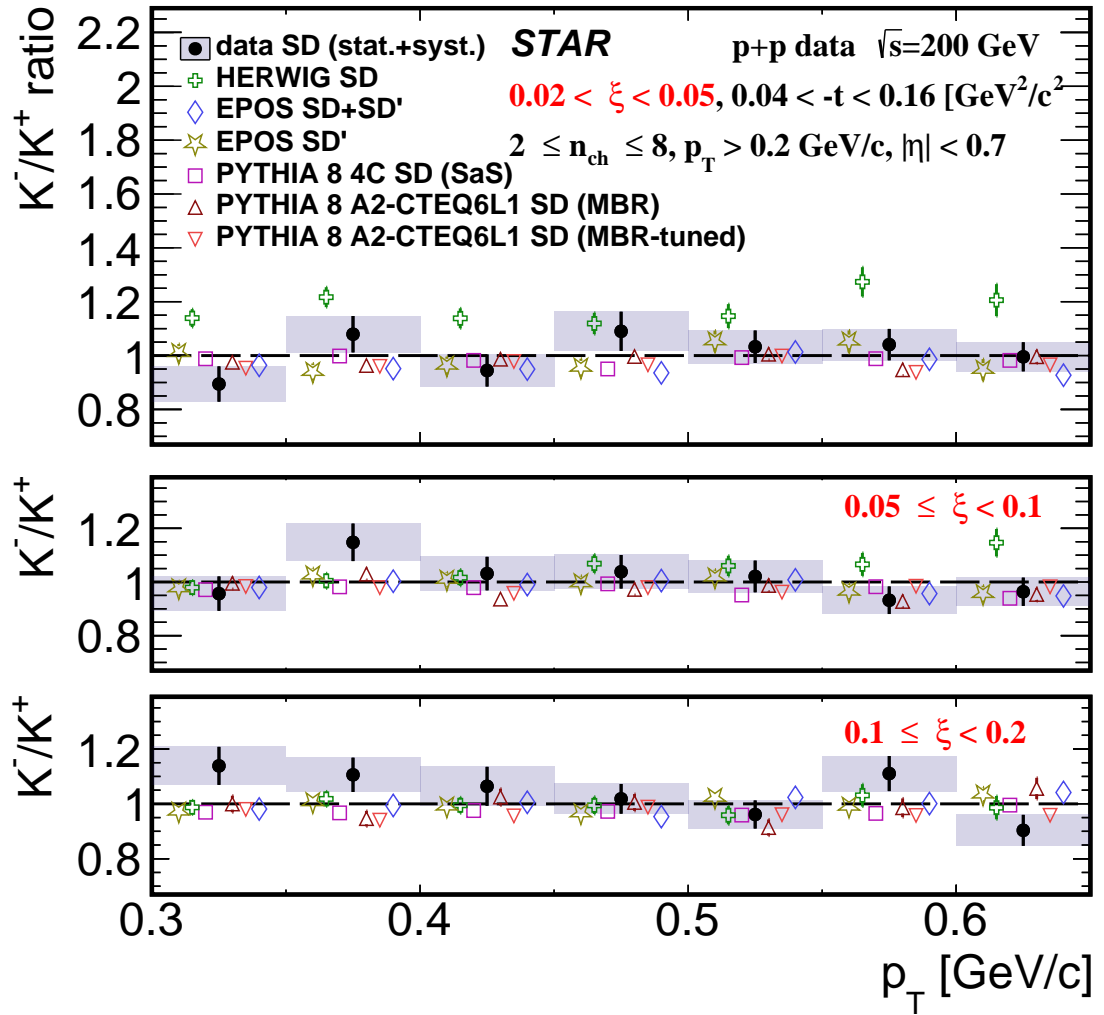


Figure 9.5: Ratio of production yields of K^-/K^+ as a function of p_{T} shown separately for the three ranges of ξ : (top) $0.02 < \xi < 0.05$, (middle) $0.05 < \xi < 0.1$, (bottom) $0.1 < \xi < 0.2$.

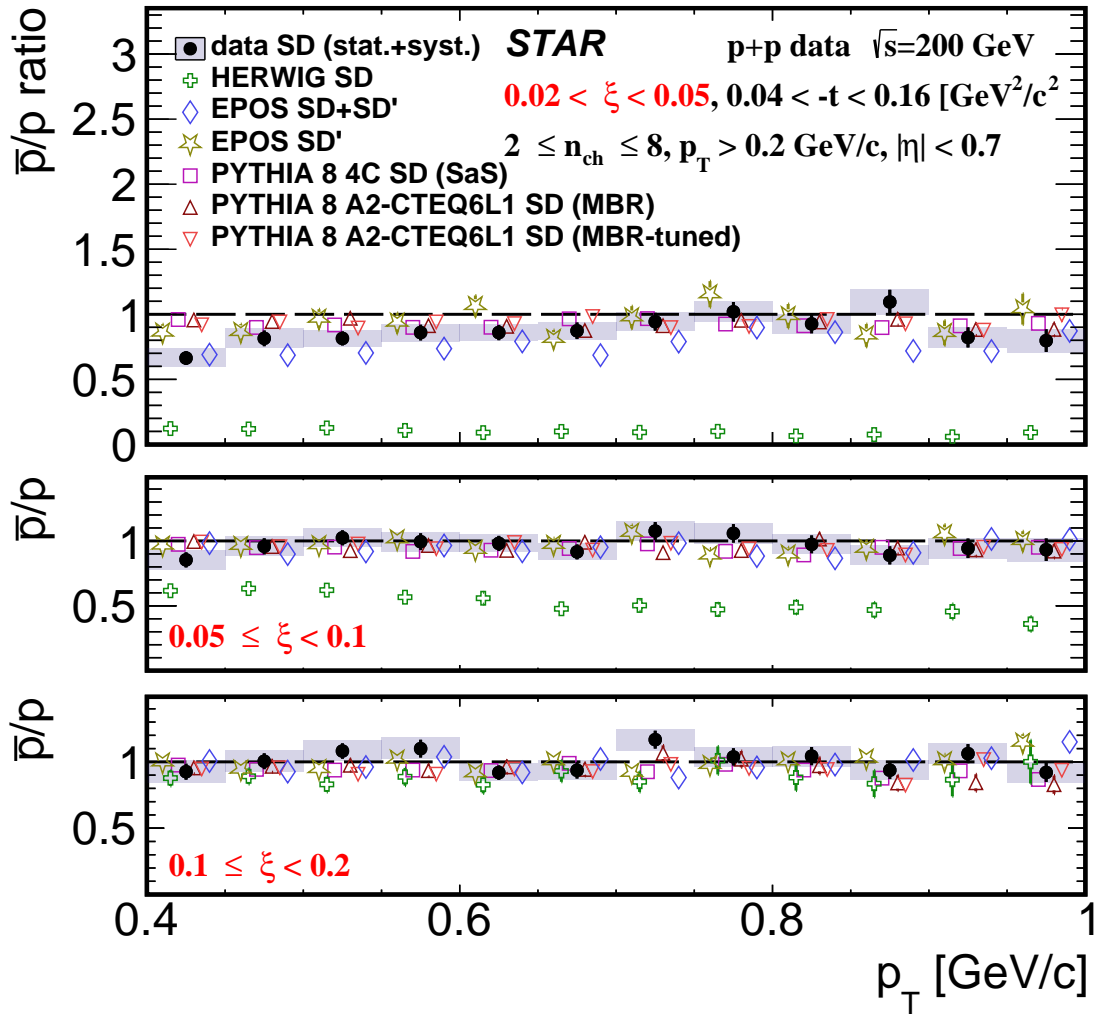


Figure 9.6: Ratio of production yields of \bar{p}/p as a function of p_T shown separately for the three ranges of ξ : (top) $0.02 < \xi < 0.05$, (middle) $0.05 < \xi < 0.1$, (bottom) $0.1 < \xi < 0.2$.

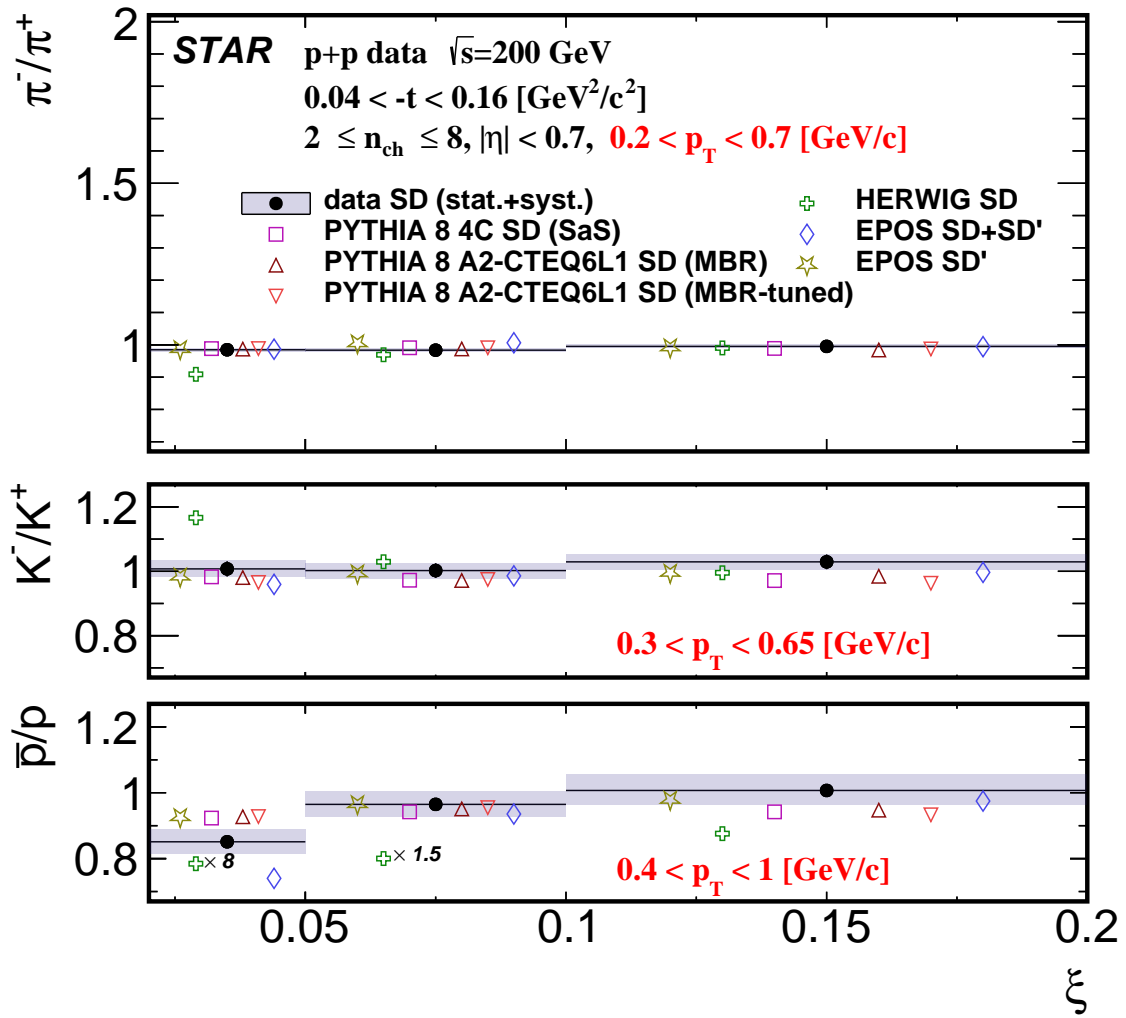


Figure 9.7: Ratio of production yields of π^-/π^+ , K^-/K^+ and \bar{p}/p as a function of ξ .

953 10. Summary and Conclusions

954 Inclusive and identified (pion, kaon, proton and their antiparticles) charged particle production in
955 Single Diffractive Dissociation process has been measured in proton-proton collisions at $\sqrt{s} = 200$
956 GeV with the STAR detector at RHIC using data corresponding to an integrated luminosity of
957 15 nb^{-1} .

958 Significant differences are observed between the measured distributions of ξ and MC model
959 predictions. Amongst the models considered, EPOS and PYTHIA 8 (MBR) without artificial
960 suppression of diffractive cross sections at large ξ provide the best description of the data.

961 Charged-particle multiplicity and its dependence on the pseudorapidity and the transverse
962 momentum are well described by PYTHIA8 and EPOS SD' models. EPOS SD+SD' and HERWIG
963 do not describe the data.

964 π^-/π^+ and K^-/K^+ production ratios are close to unity and consistent with most of model
965 predictions except for HERWIG.

966 \bar{p}/p production ratio shows a significant deviation from unity in the $0.02 < \xi < 0.05$ range
967 indicating a non-negligible transfer of the baryon number from the forward to the central region.
968 Equal amount of protons and antiprotons are observed in the $\xi > 0.05$ range. PYTHIA8, EPOS
969 SD+SD' and EPOS SD' agree with data for $\xi > 0.05$. For $0.02 < \xi < 0.05$ PYTHIA 8 and
970 EPOS SD' predict small deviations from unity (0.93) which is however higher than observed
971 in data (0.85 ± 0.04). EPOS SD+SD' predicts an asymmetry between \bar{p} and p of $\sim 30\%$ at
972 $0.02 < \xi < 0.05$. HERWIG predicts much larger baryon number transfers compared to data for
973 $\xi < 0.1$ and shows consistency with data for $\xi > 0.1$.

Bibliography

- [1] L. Adamczyk, L. Fulek, and R. Sikora, *Supplementary note on diffractive analyses of 2015 proton-proton data*, <https://drupal.star.bnl.gov/STAR/starnotes/private/psn0732>, July, 2019.
- [2] B. Z. Kopeliovich and B. G. Zakharov, *Novel Mechanisms of Baryon Number Flow Over Large Rapidity Gap*, Z. Phys. **C43** (1989) 241.
- [3] F. W. Bopp, *Baryon transport in dual models and the possibility of a backward peak in diffraction*, in *New trends in high-energy physics: Experiment, phenomenology, theory. Proceedings, International School-Conference, Crimea 2000, Yalta, Ukraine, May 27-June 4, 2000*. arXiv:hep-ph/0007229 [hep-ph].
- [4] M. Anderson et al., *The STAR Time Projection Chamber: A Unique tool for studying high multiplicity events at RHIC*, Nucl. Instrum. Meth. **A499** (2003) 659–678, arXiv:nucl-ex/0301015 [nucl-ex].
- [5] T. Sjöstrand, S. Mrenna, and P. Z. Skands, *PYTHIA 6.4 Physics and Manual*, JHEP **05** (2006) 026.
- [6] R. Ciesielski and K. Goulianos, *MBR Monte Carlo Simulation in PYTHIA8*, PoS **ICHEP2012** (2013) 301, arXiv:1205.1446 [hep-ph].
- [7] *Roman Pot Phase II* - online DAQ monitoring*, <https://online.star.bnl.gov/rp/pp200/>.
- [8] *STAR RunLog Browser*, <https://online.star.bnl.gov/RunLogRun15/>.
- [9] W. Fischer, *Run Overview of the Relativistic Heavy Ion Collider*, <http://www.agsrhichome.bnl.gov/RHIC/Runs/>.
- [10] *STAR Luminosity Tracker*, <https://www.star.bnl.gov/protected/common/common2015/trigger2015/runningStatepp200GeV/plots.html>.
- [11] STAR Collaboration, J. Adam et al., *Results on Total and Elastic Cross Sections in Proton-Proton Collisions at $\sqrt{s} = 200$ GeV*, arXiv:2003.12136 [hep-ex].
- [12] STAR Collaboration, B. I. Abelev et al., *Systematic Measurements of Identified Particle Spectra in $p\bar{p}$, $d^+ \text{Au}$ and $\text{Au}+\text{Au}$ Collisions from STAR*, Phys. Rev. **C79** (2009) 034909, arXiv:0808.2041 [nucl-ex].
- [13] CDF Collaboration, D. Acosta et al., *Inclusive double pomeron exchange at the Fermilab Tevatron $\bar{p}p$ collider*, Phys. Rev. Lett. **93** (2004) 141601, arXiv:hep-ex/0311023 [hep-ex].
- [14] ATLAS Collaboration, G. Aad et al., *Charged-particle distributions in $\sqrt{s} = 13$ TeV $p\bar{p}$ interactions measured with the ATLAS detector at the LHC*, Phys. Lett. **B758** (2016) 67–88, arXiv:1602.01633 [hep-ex].

- 1008 [15] G. D'Agostini, *A Multidimensional unfolding method based on Bayes' theorem*, Nucl.
1009 Instrum. Meth. **A362** (1995) 487–498.
- 1010 [16] H. Bichsel, *A method to improve tracking and particle identification in TPCs and silicon
1011 detectors*, Nucl. Instrum. Meth. **A562** (2006) 154–197.

Appendices

₁₀₁₃ **A. Proton and Antiproton DCA
Distributions**

₁₀₁₄

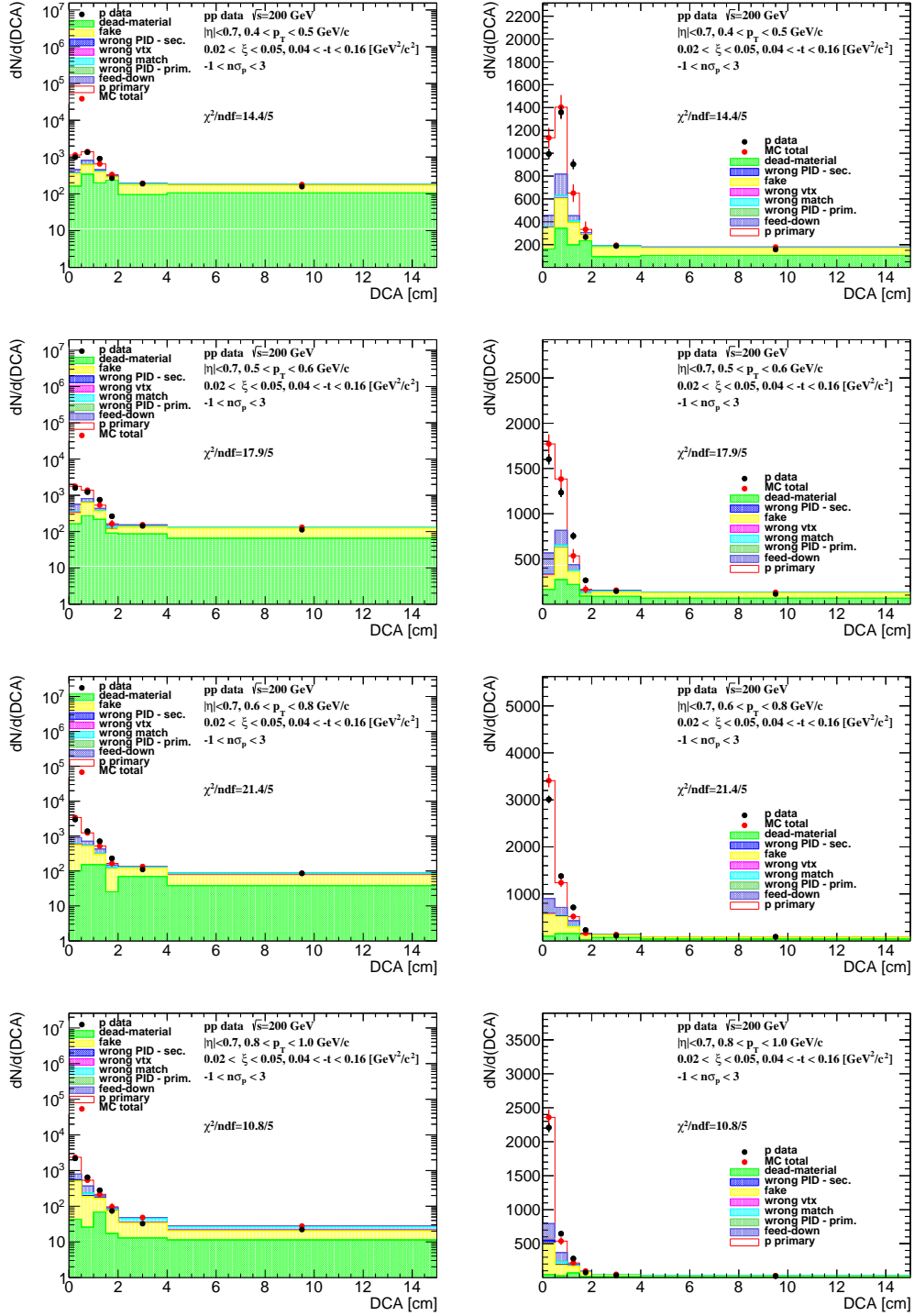


Figure A.1: Distributions of DCA for protons in SD interactions with $0.02 < \xi < 0.05$ and loose selection.

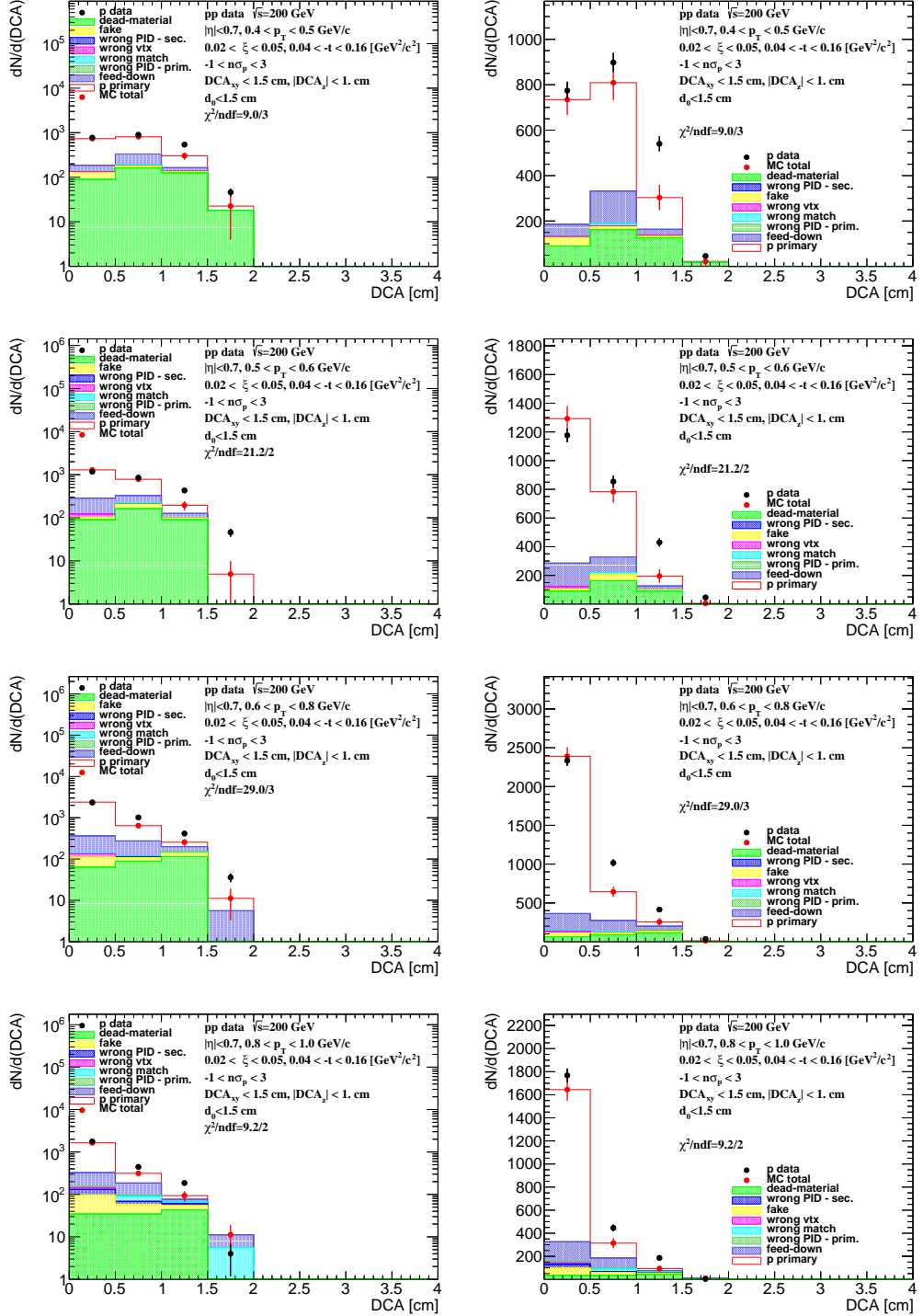


Figure A.2: Distributions of DCA for protons in SD interactions with $0.02 < \xi < 0.05$ and normal selection.

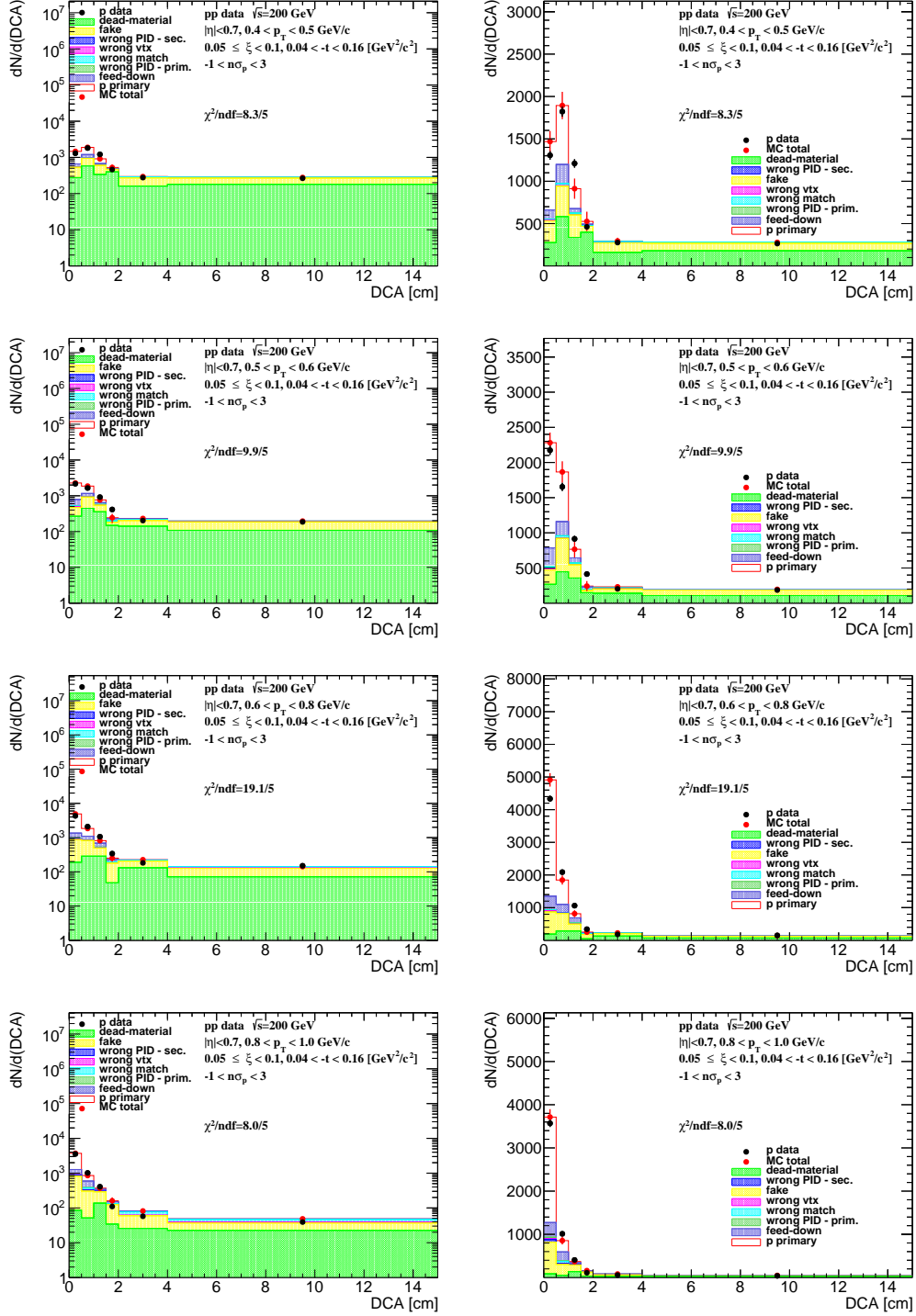


Figure A.3: Distributions of DCA for protons in SD interactions with $0.05 < \xi < 0.1$ and loose selection.

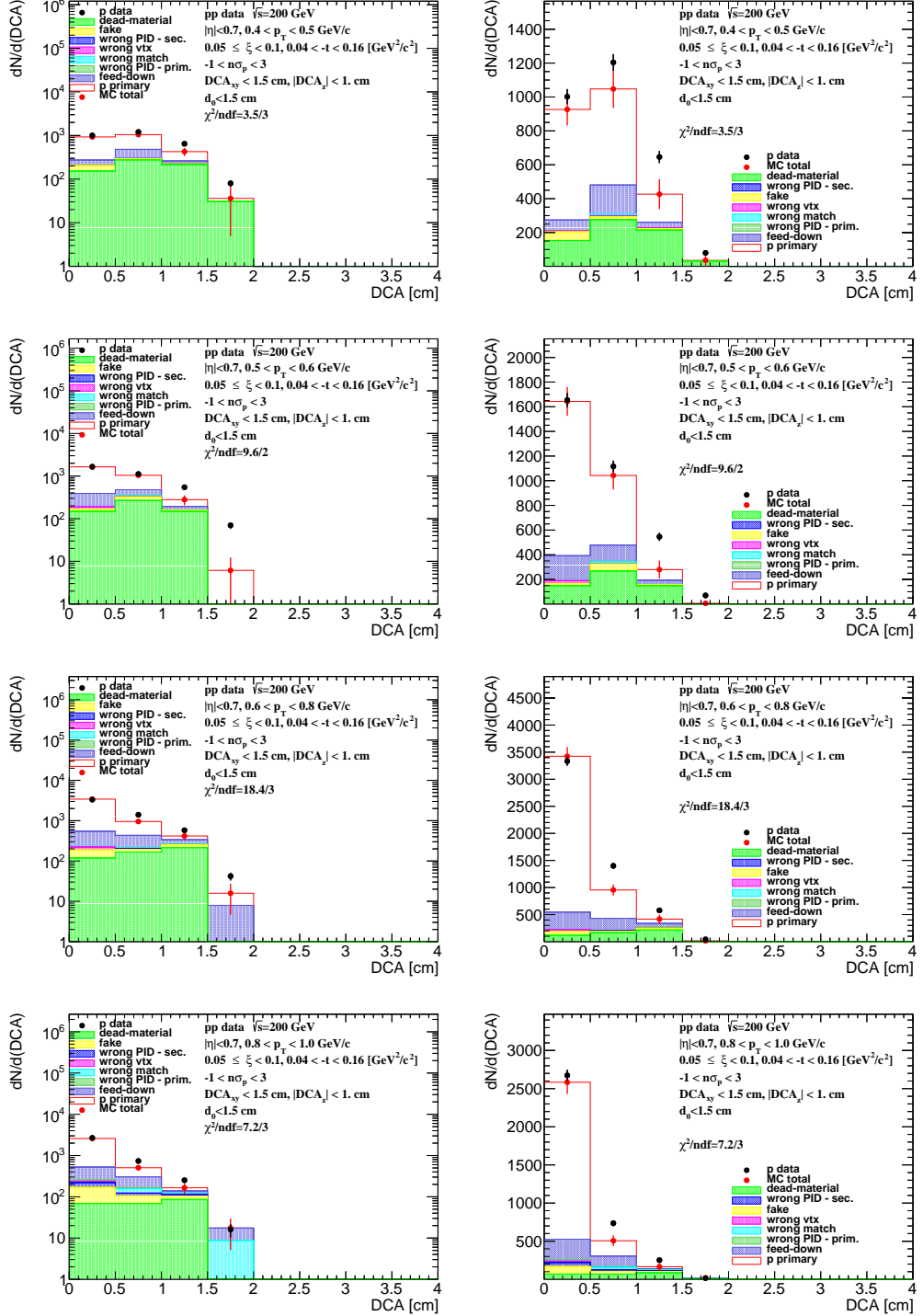


Figure A.4: Distributions of DCA for protons in SD interactions with $0.05 < \xi < 0.1$ and normal selection.

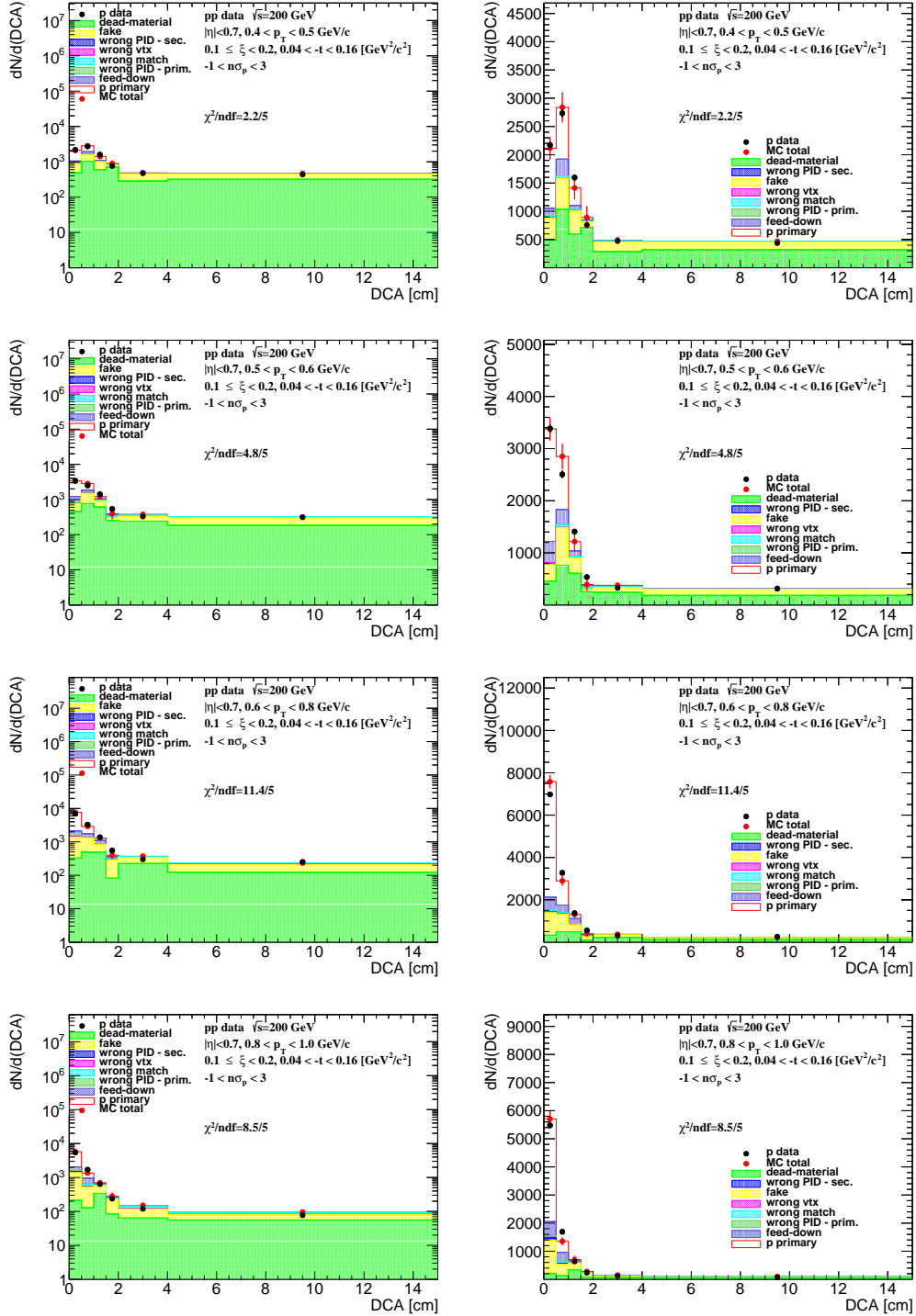


Figure A.5: Distributions of DCA for protons in SD interactions with $0.1 < \xi < 0.2$ and loose selection.

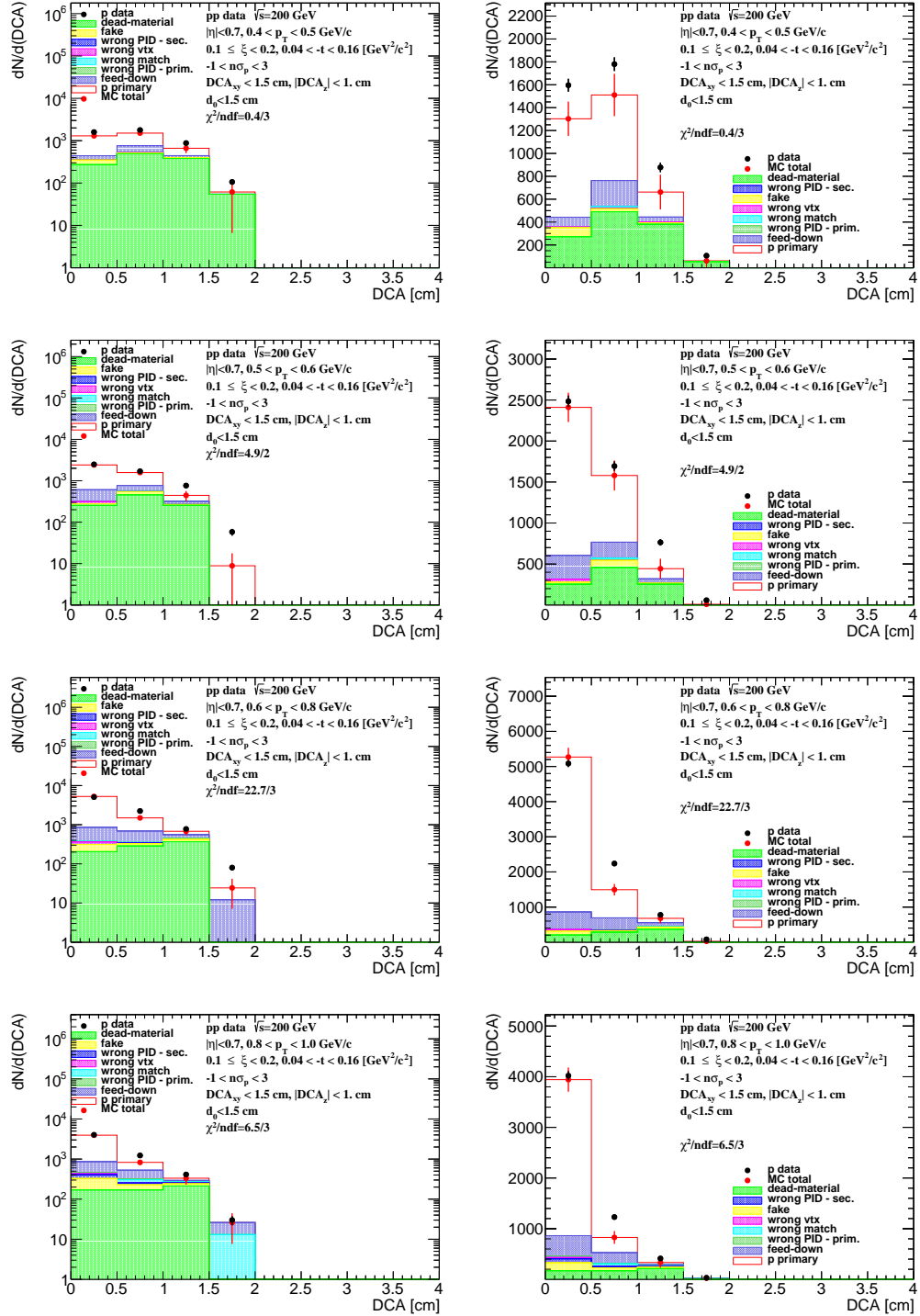


Figure A.6: Distributions of DCA for protons in SD interactions with $0.1 < \xi < 0.2$ and normal selection.

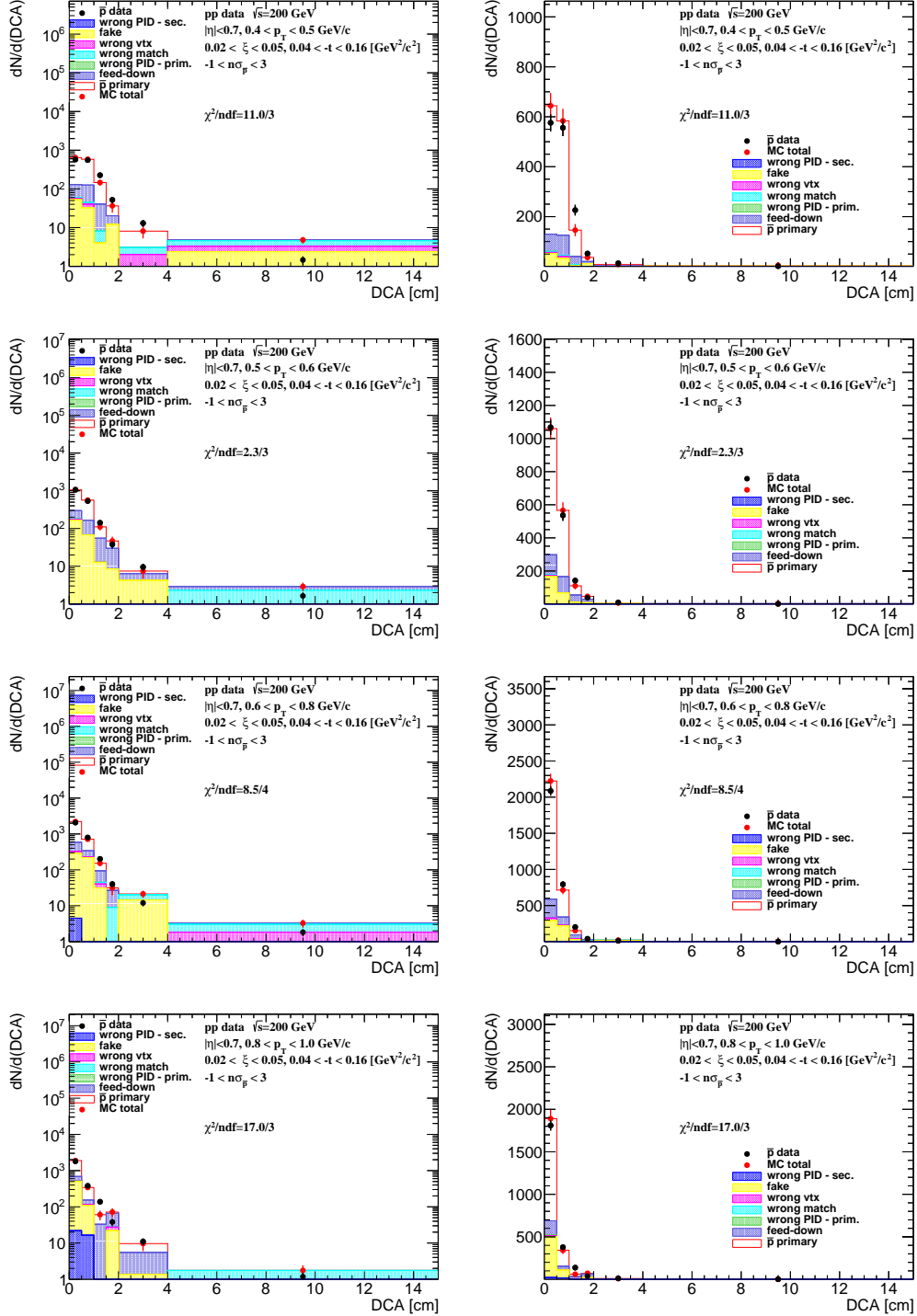


Figure A.7: Distributions of DCA for antiprotons in SD interactions with $0.02 < \xi < 0.05$ and loose selection.

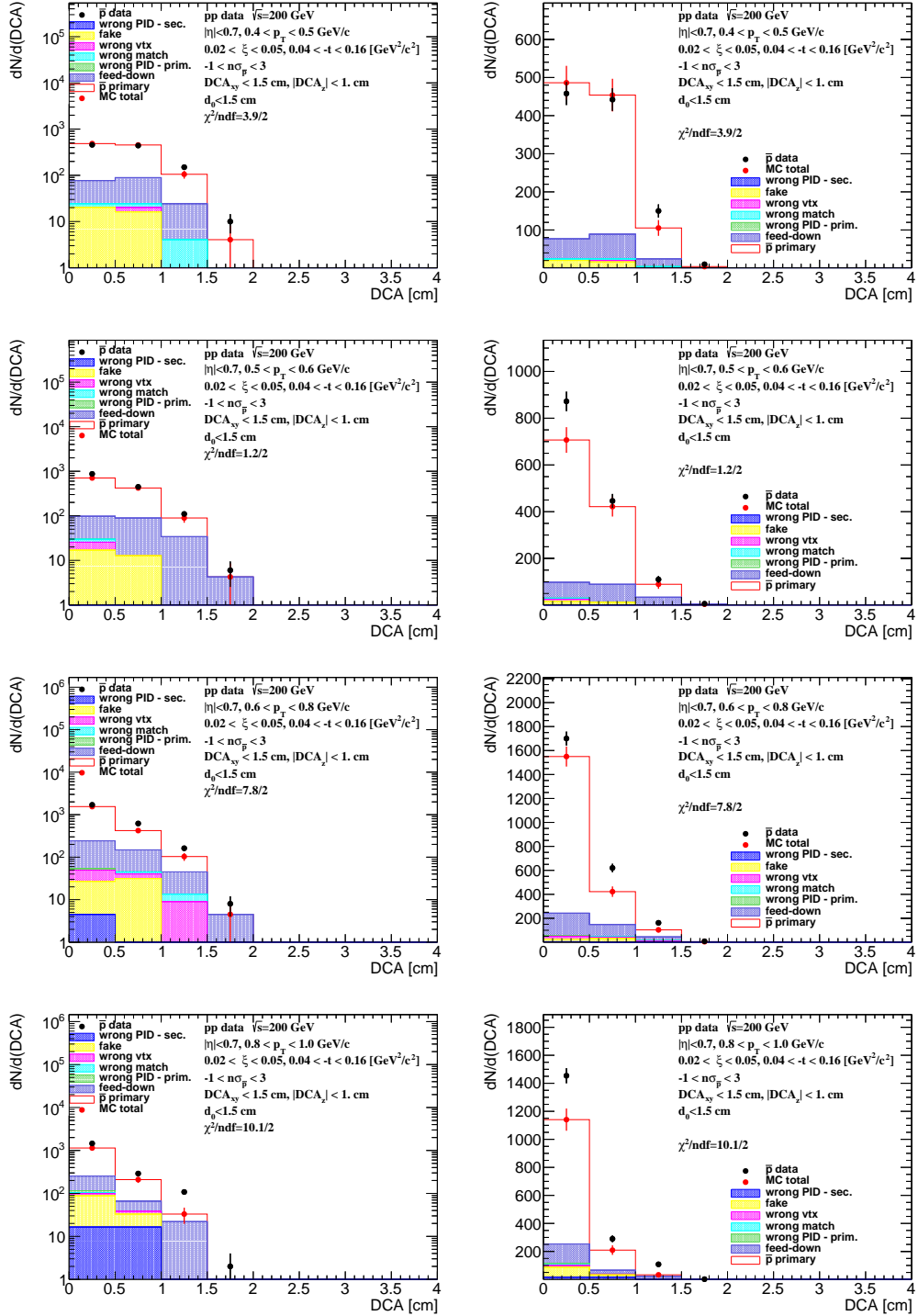


Figure A.8: Distributions of DCA for antiprotons in SD interactions with $0.02 < \xi < 0.05$ and normal selection.

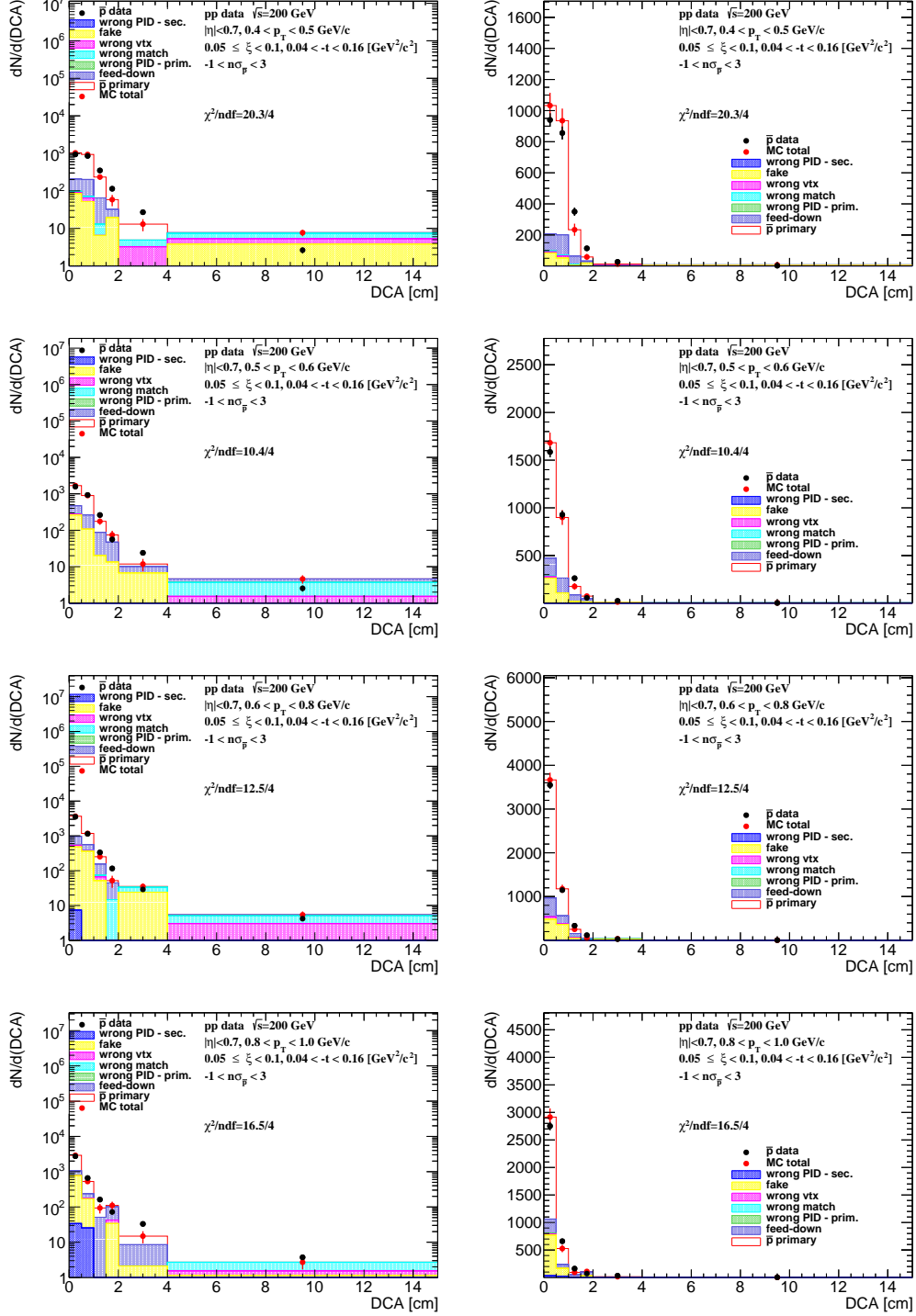


Figure A.9: Distributions of DCA for antiprotons in SD interactions with $0.05 < \xi < 0.1$ and loose selection.

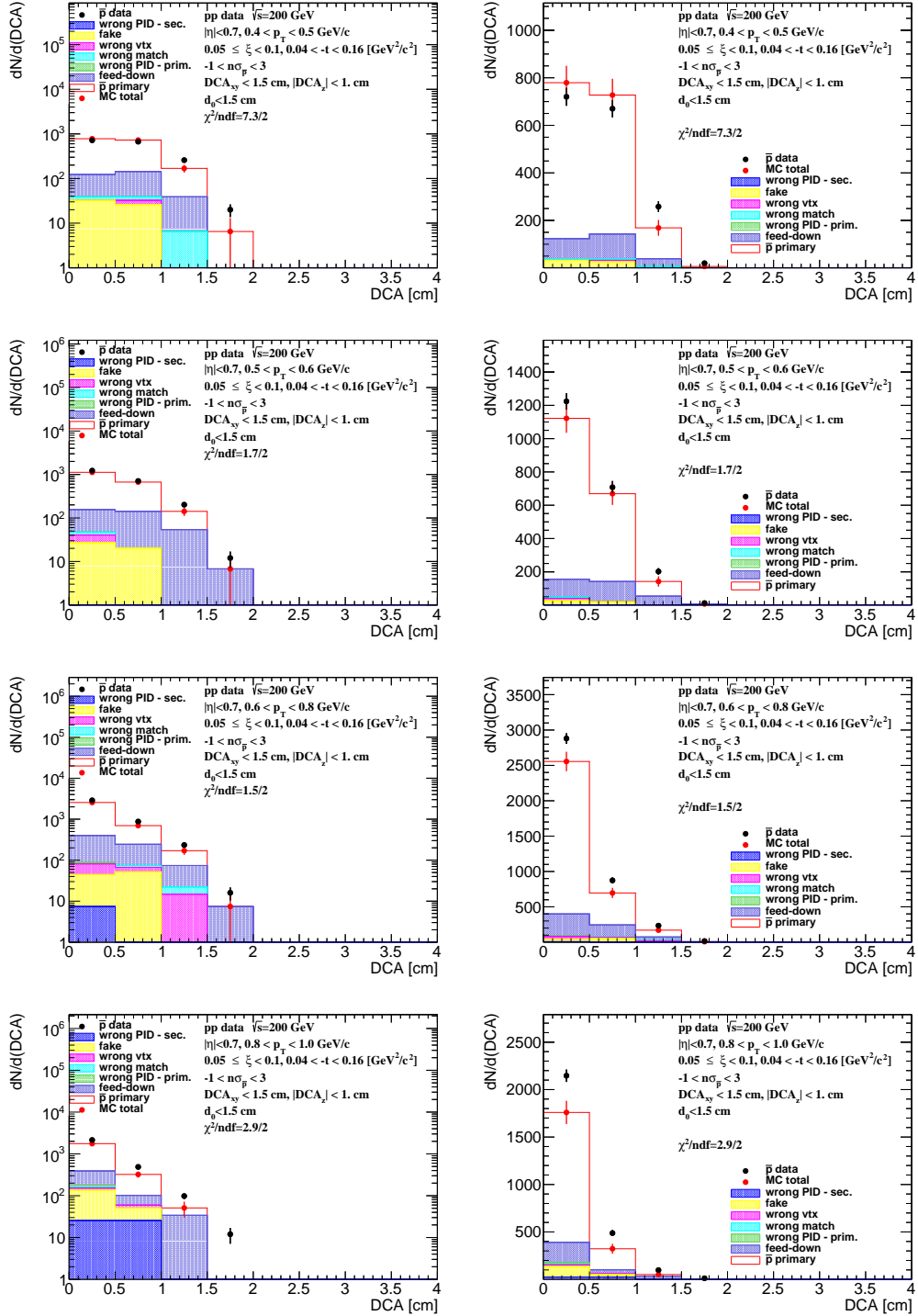


Figure A.10: Distributions of DCA for antiprotons in SD interactions with $0.05 < \xi < 0.1$ and normal selection.

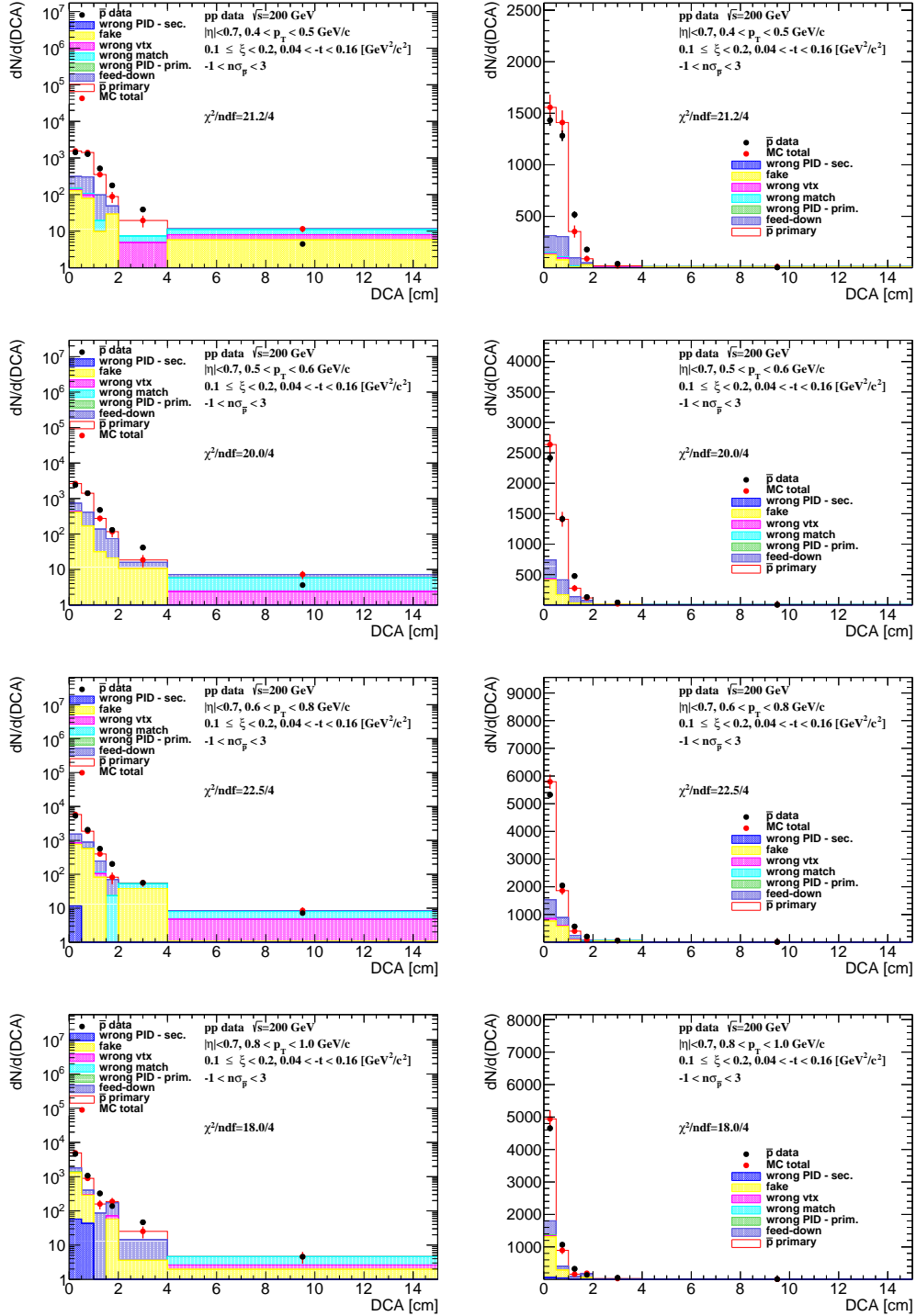


Figure A.11: Distributions of DCA for antiprotons in SD interactions with $0.1 < \xi < 0.2$ and loose selection.

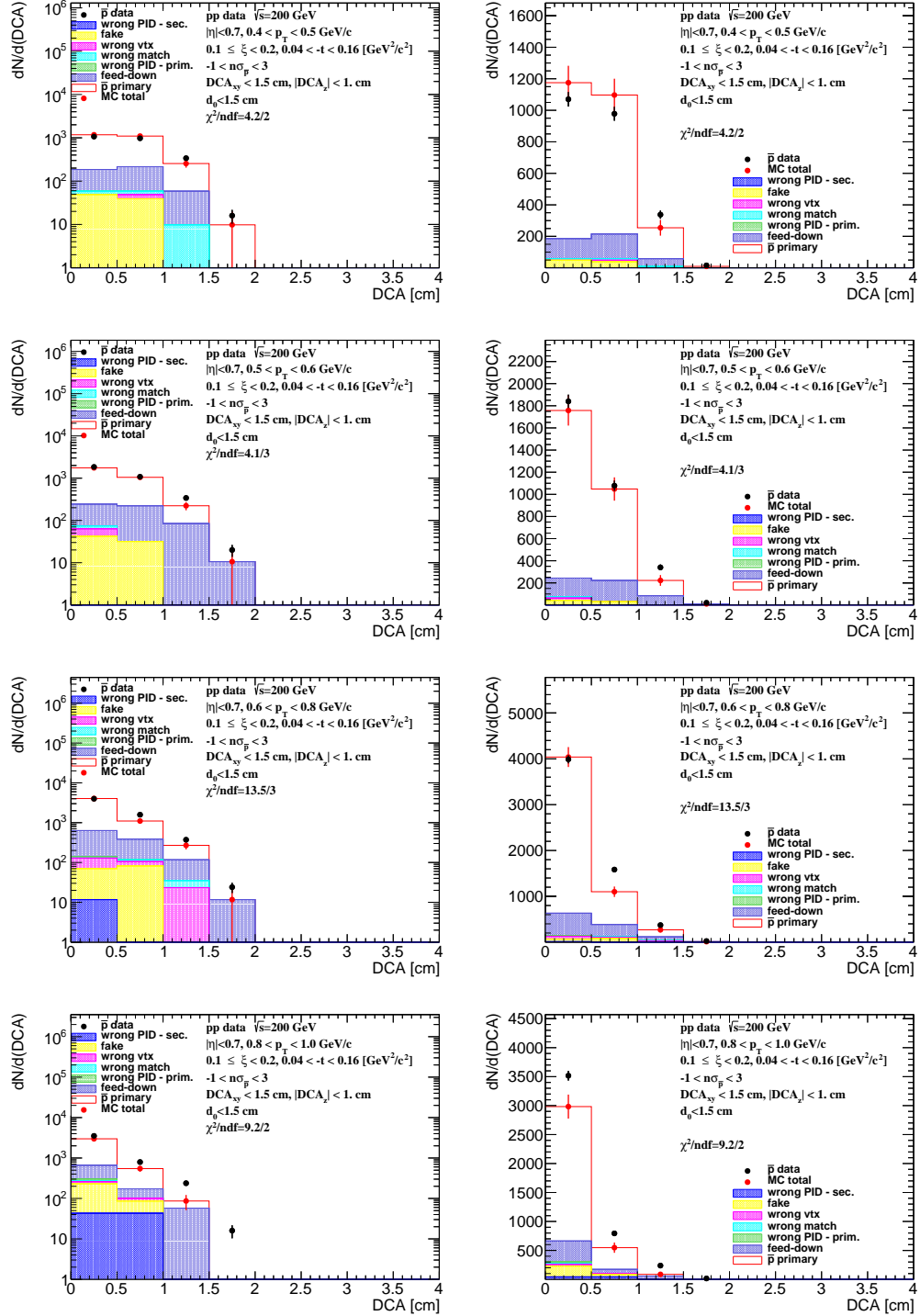


Figure A.12: Distributions of DCA for antiprotons in SD interactions with $0.1 < \xi < 0.2$ and normal selection.

B. Distributions of $n\sigma_{dE/dx}^i$ in SD

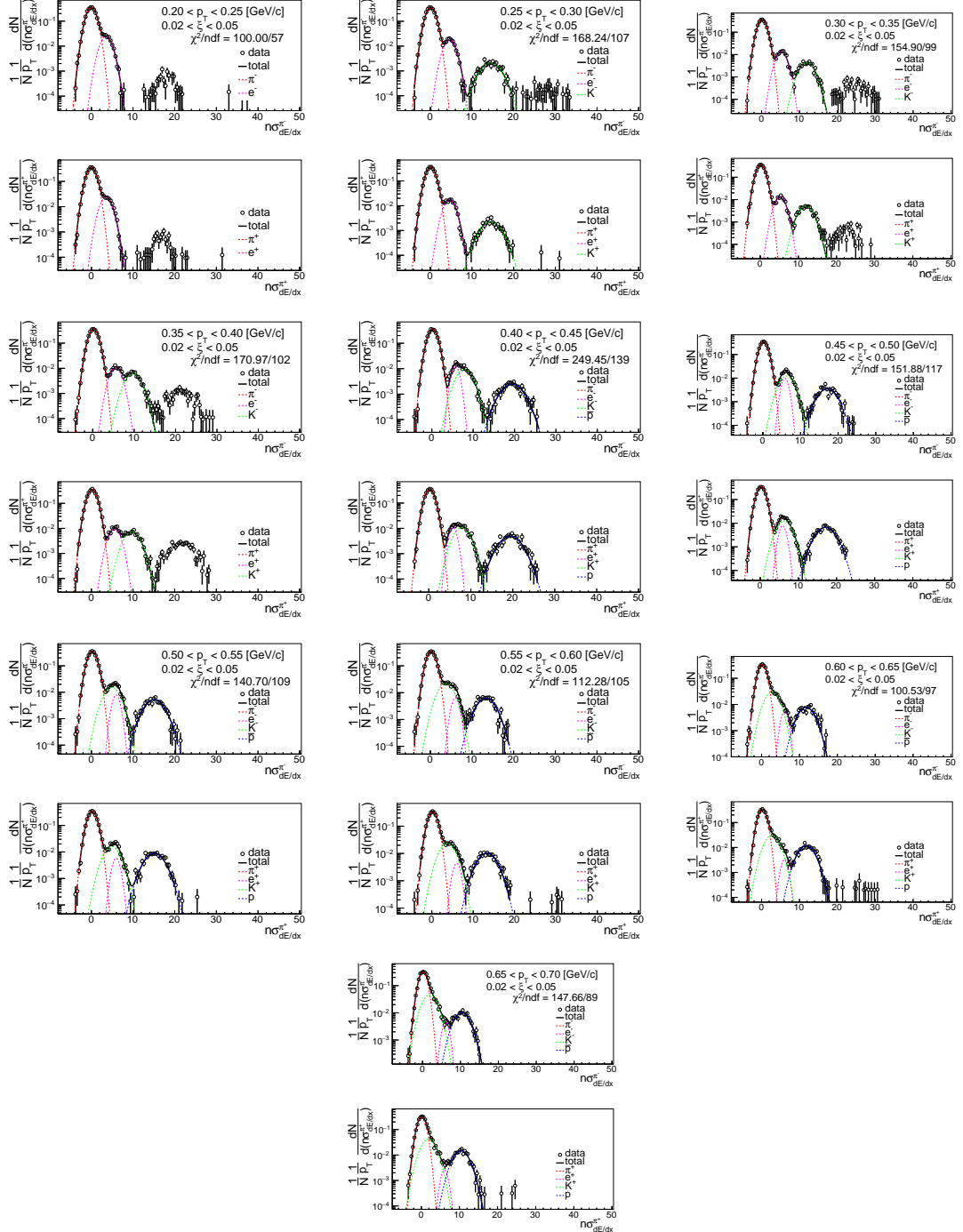


Figure B.1: Distributions of $n\sigma_{dE/dx}^{\pi^\pm}$ for π^\pm in SD interactions with $0.02 < \xi < 0.05$.

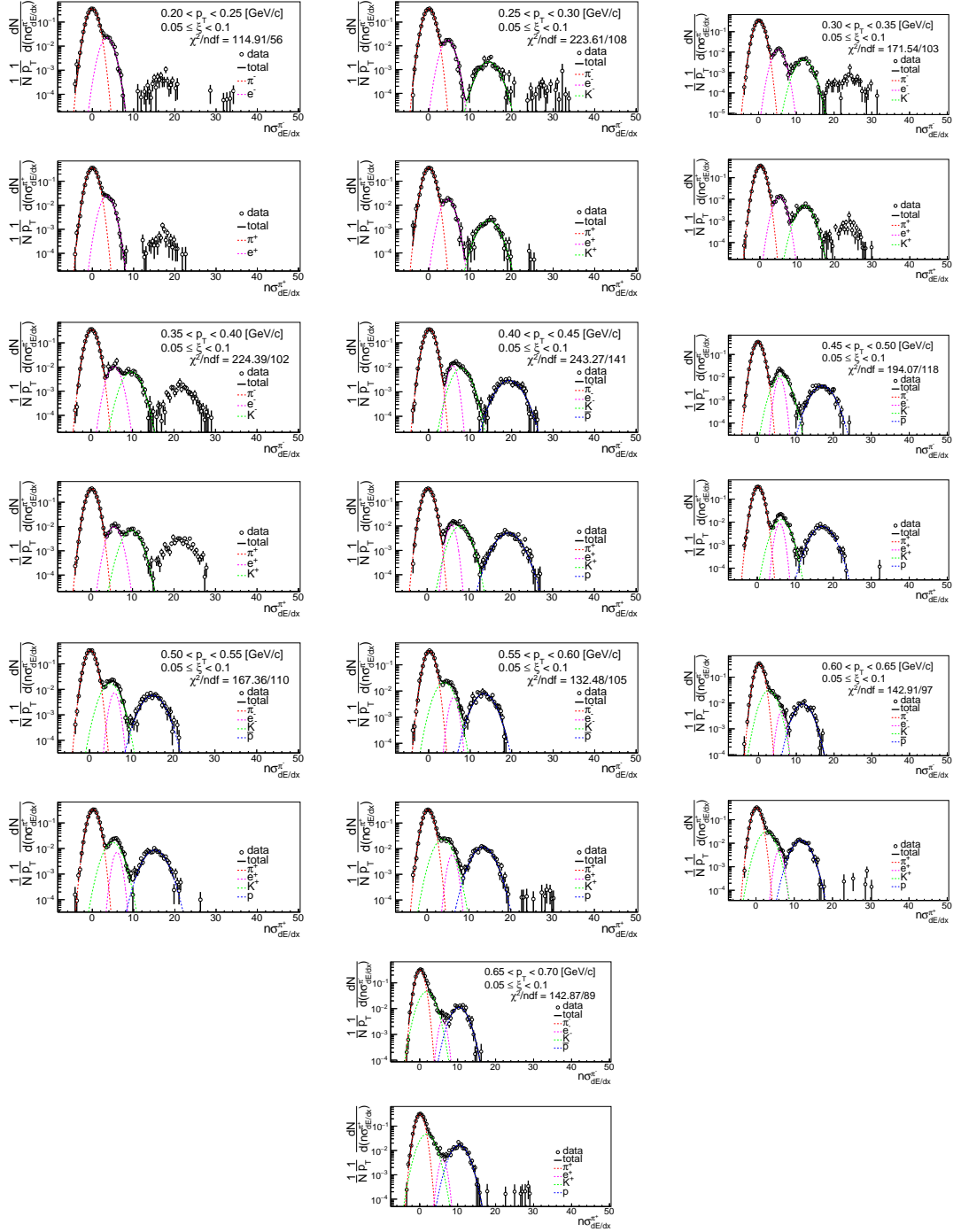


Figure B.2: Distributions of $n\sigma_{dE/dx}^{\pi^\pm}$ for π^\pm in SD interactions with $0.05 < \xi < 0.1$.

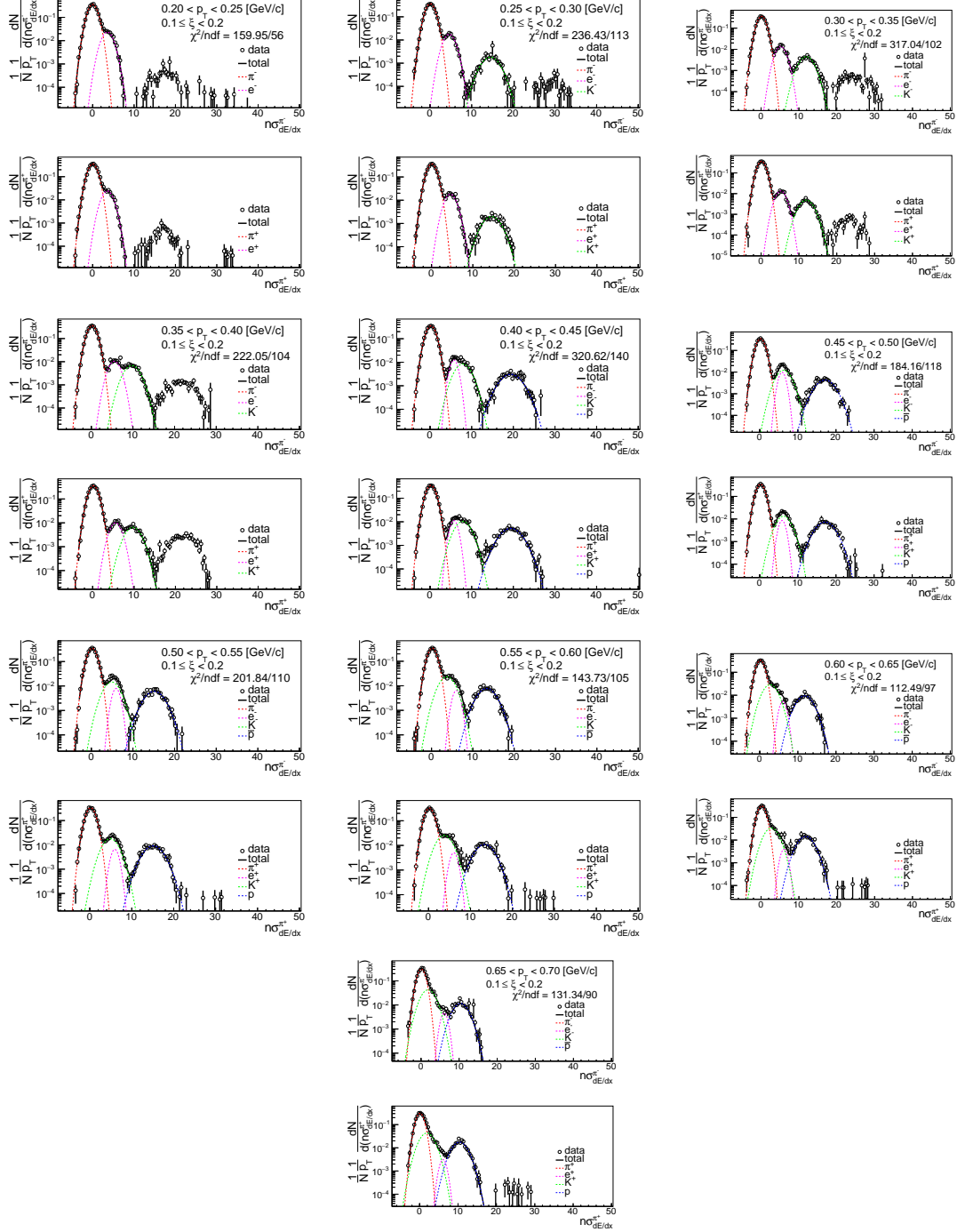


Figure B.3: Distributions of $n\sigma_{dE/dx}^{\pi^\pm}$ for π^\pm in SD interactions with $0.1 < \xi < 0.2$.

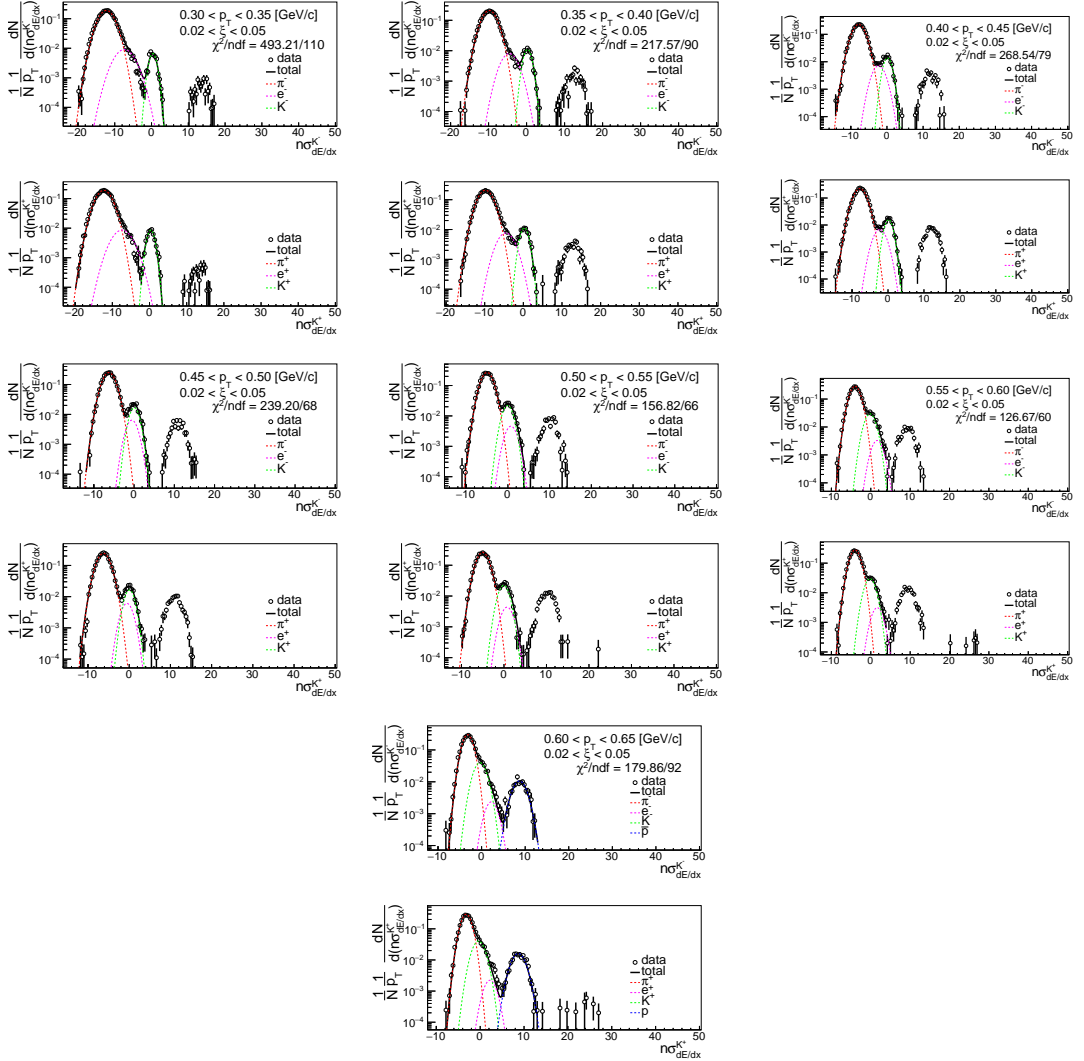


Figure B.4: Distributions of $n\sigma_{dE/dx}^{K^\pm}$ for K^\pm in SD interactions with $0.02 < \xi < 0.05$.

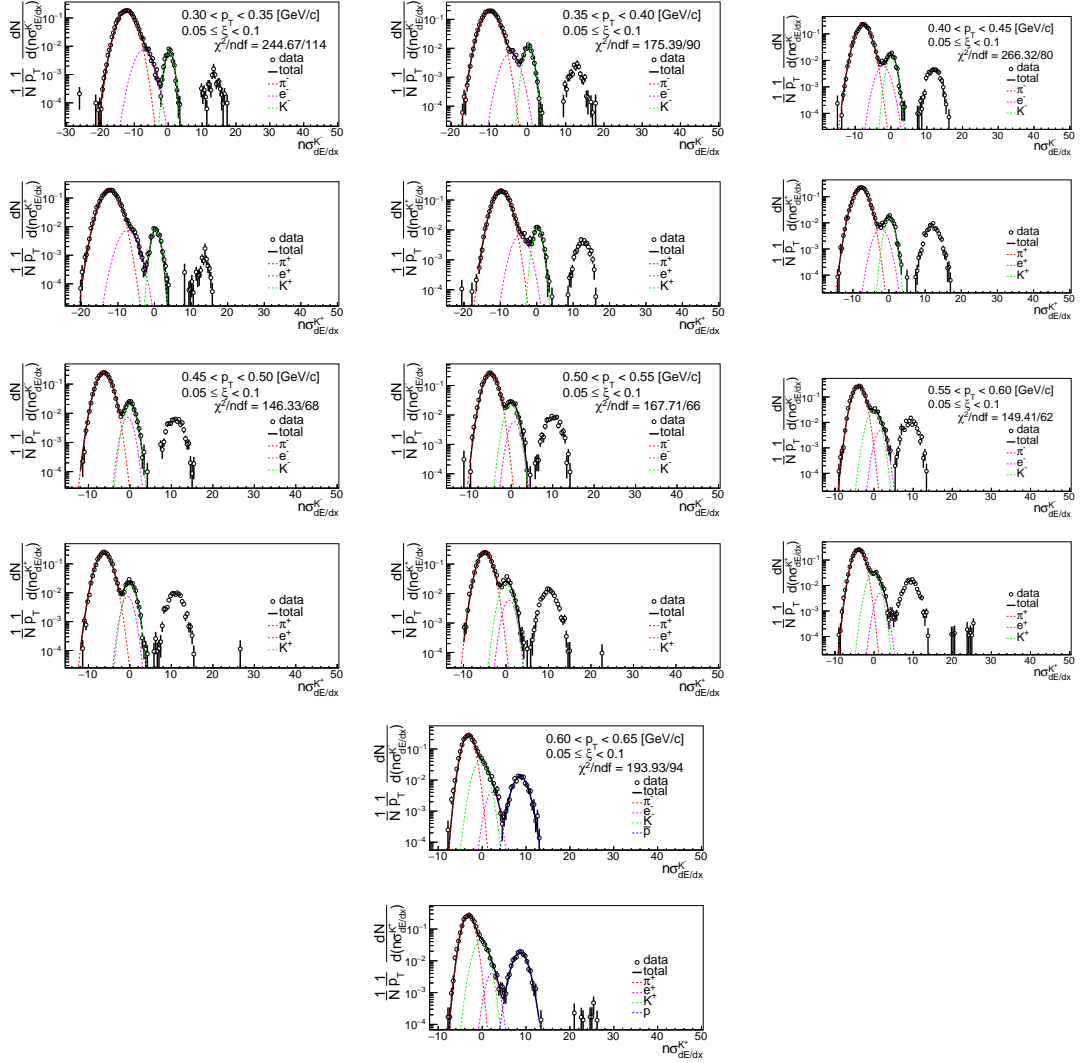


Figure B.5: Distributions of $n\sigma_{dE/dx}^{K^\pm}$ for K^\pm in SD interactions with $0.05 < \xi < 0.1$.

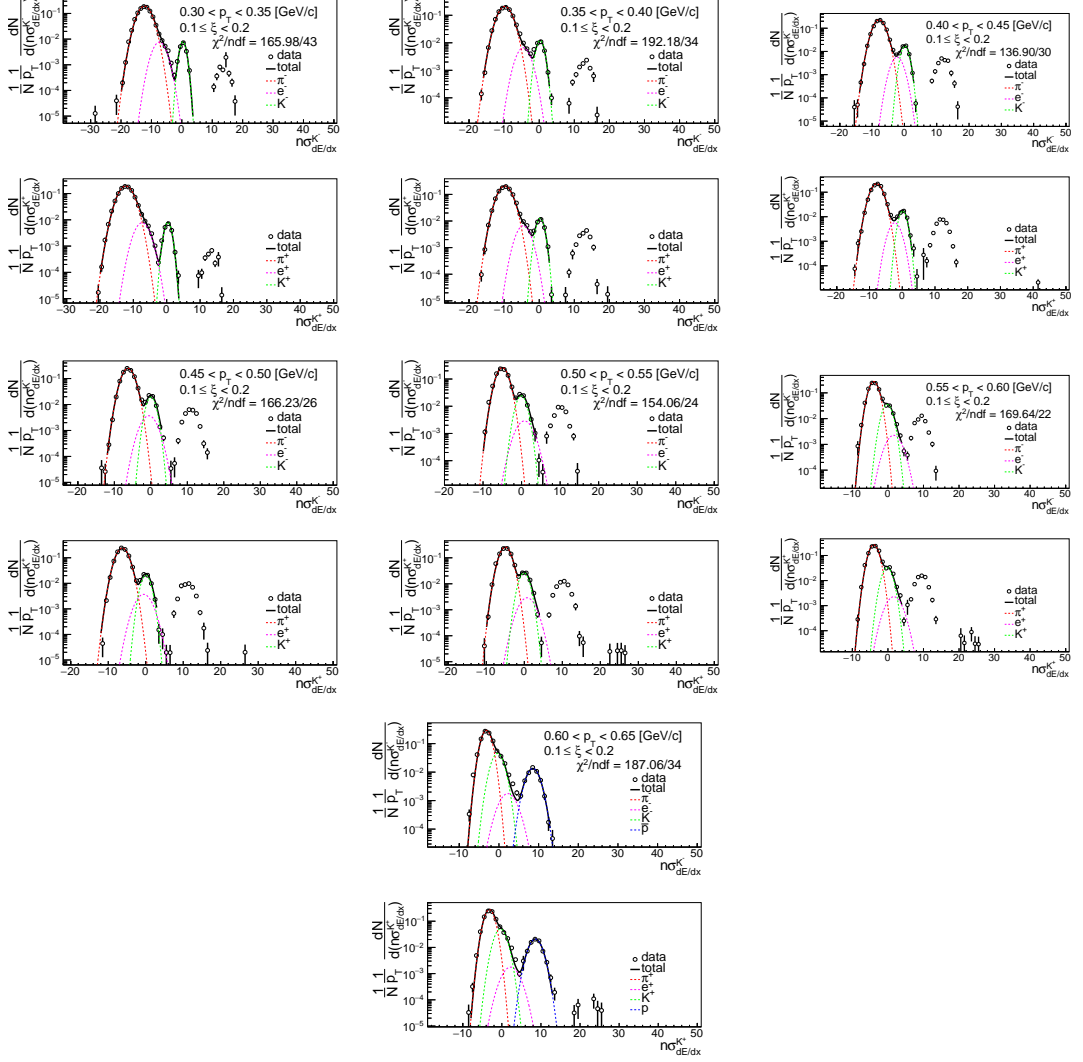


Figure B.6: Distributions of $n\sigma_{dE/dx}^{K^\pm}$ for K^\pm in SD interactions with $0.1 < \xi < 0.2$.

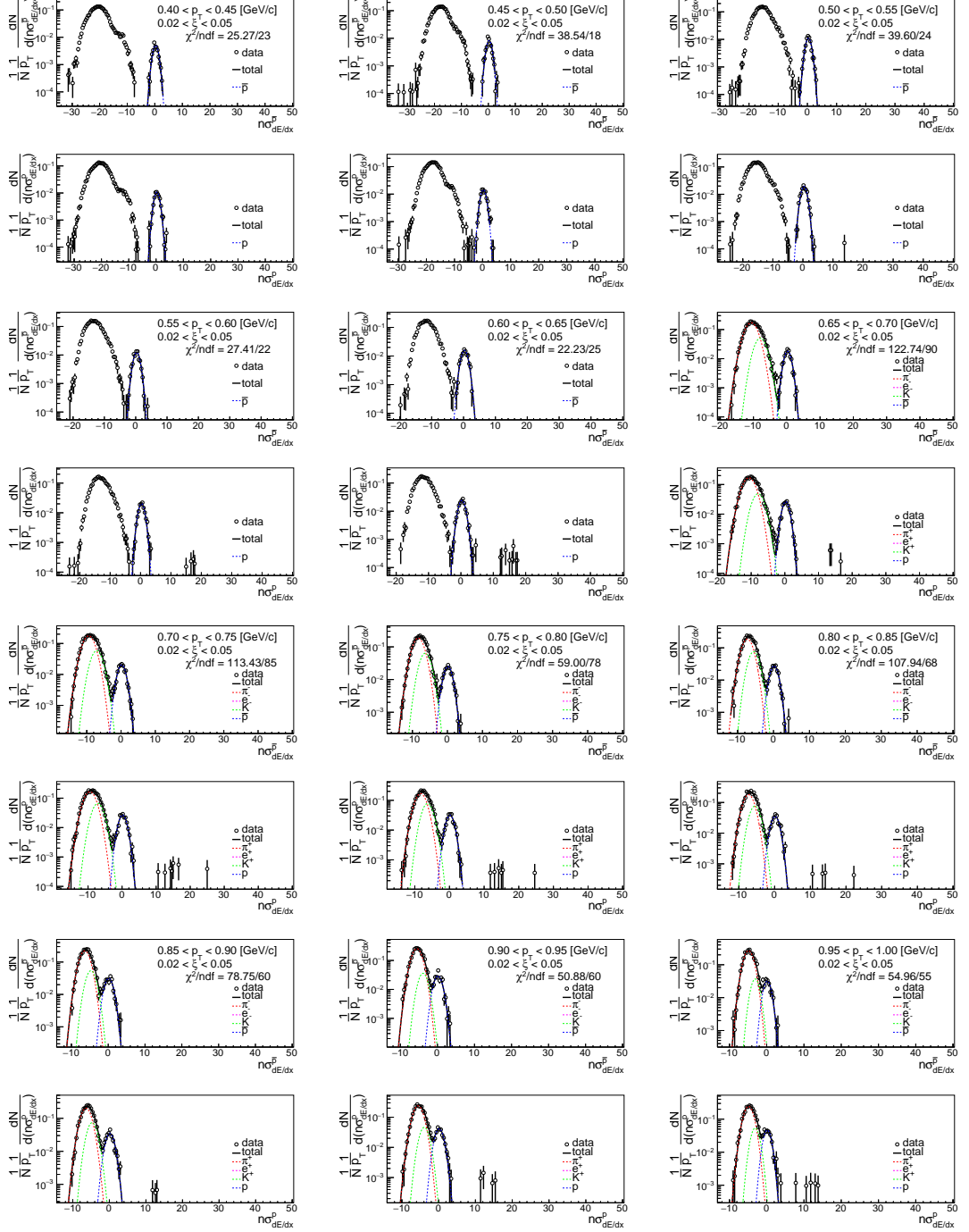


Figure B.7: Distributions of $n\sigma_{dE/dx}^{\bar{p}, p}$ for \bar{p}, p in SD interactions with $0.02 < \xi < 0.05$.

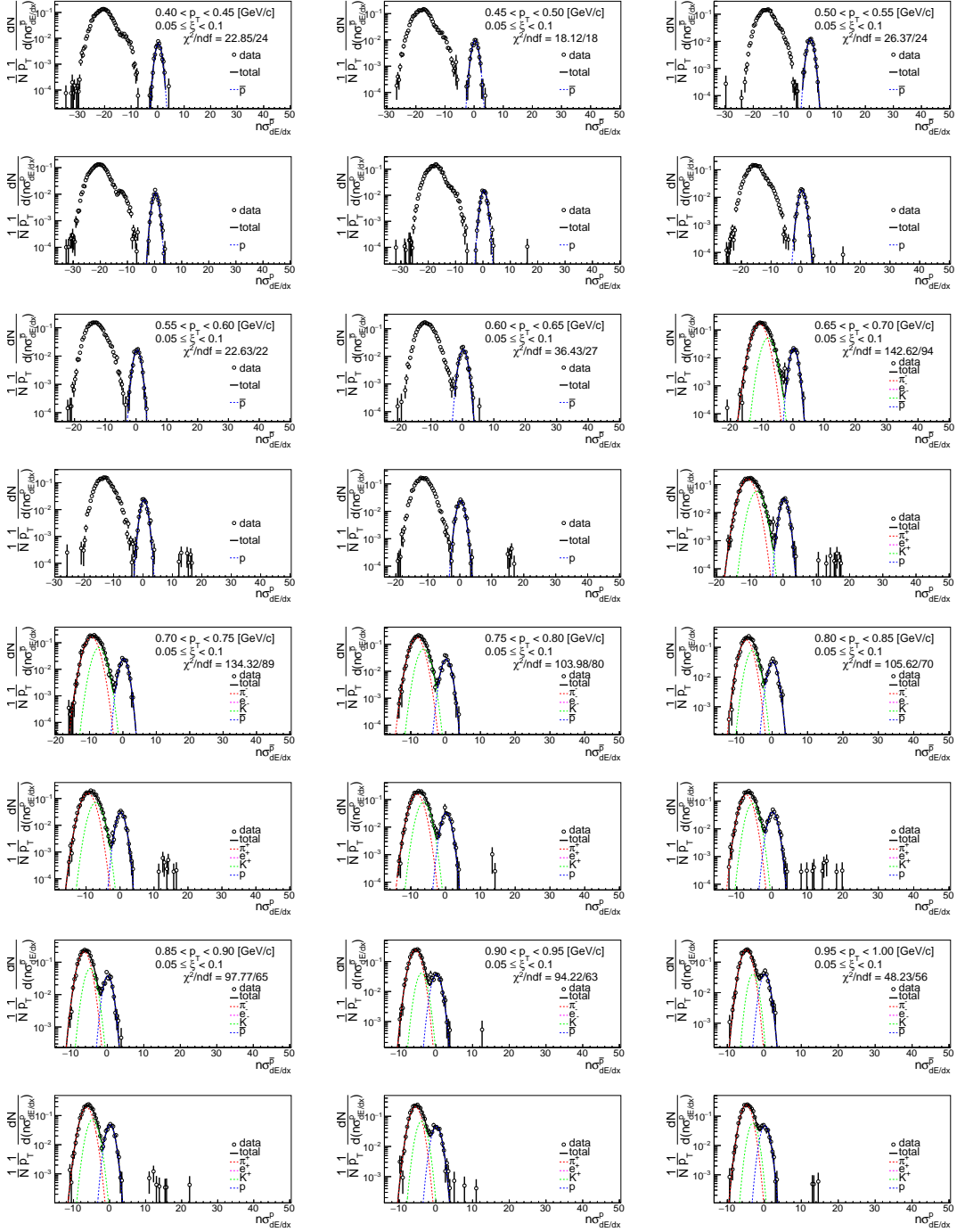


Figure B.8: Distributions of $n\sigma_{dE/dx}^{\bar{p},p}$ for \bar{p}, p in SD interactions with $0.05 < \xi < 0.1$.

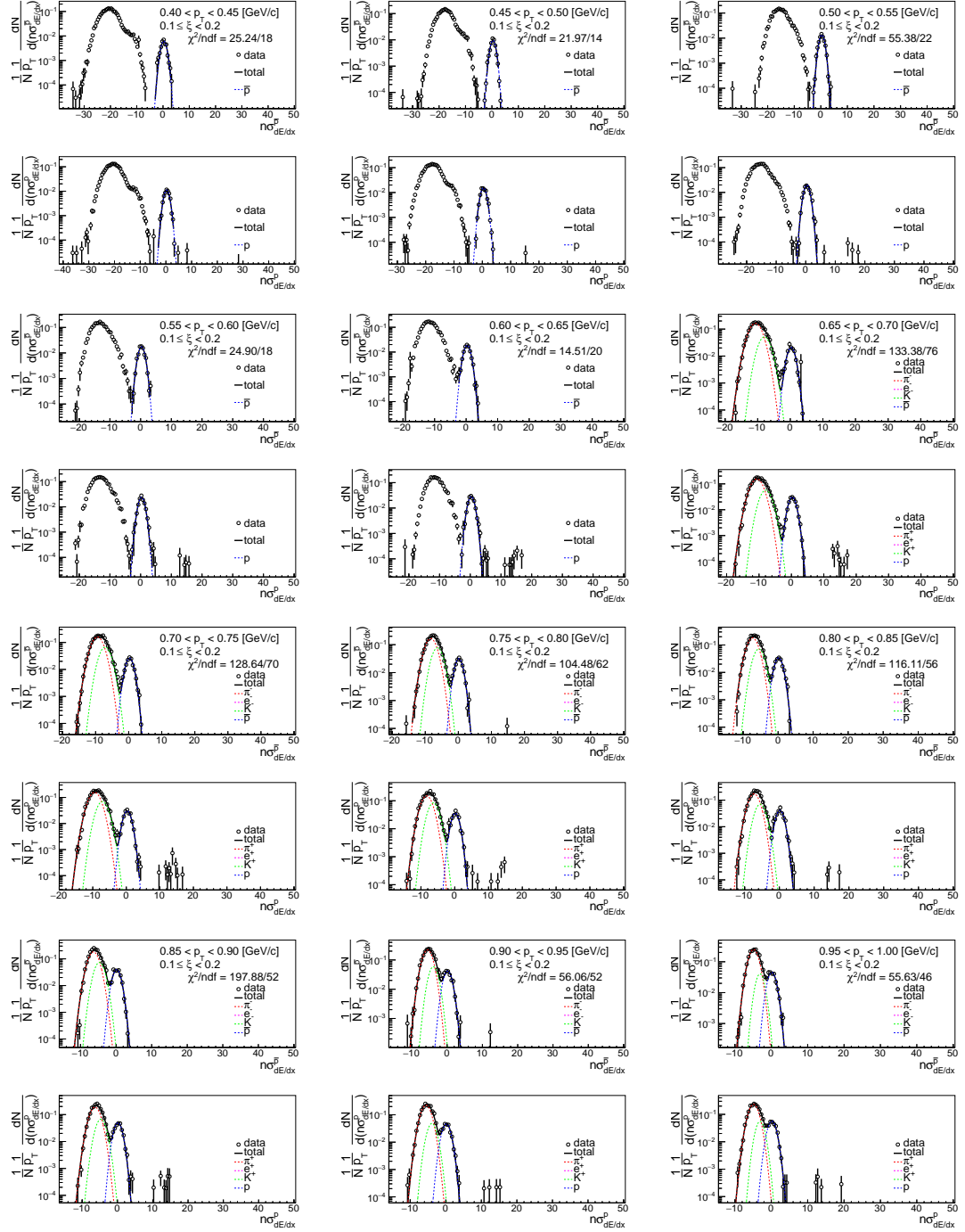


Figure B.9: Distributions of $n\sigma_{dE/dx}^{\bar{p},p}$ for \bar{p}, p in SD interactions with $0.1 < \xi < 0.2$.